SAPIENZA
UNIVERSITÀ DI ROMA

DEPARTMENT OF MECHANICAL AND AEROSPACE ENGINEERING

DOCTORAL THESIS

The gravity fields of Jupiter and Saturn as determined by Juno and Cassini

Author:
Daniele DURANTE

Supervisor:
Prof. Luciano IESS

Doctor of Philosophy in Aeronautical And Space Engineering
30th Cycle

Academic year 2016-2017

"We are not at the end but at the beginning of a new physics. But whatever we find, there will always be new horizons continually awaiting us."

Michio Kaku, Astrophysicist

Sapienza Università di Roma

Abstract

Faculty of Civil and Industrial Engineering
Department of Mechanical and Aerospace Engineering

Doctor of Philosophy in Aeronautical And Space Engineering

The gravity fields of Jupiter and Saturn as determined by Juno and Cassini

by Daniele DURANTE

This Doctoral Thesis reports on the analysis procedure for the data acquired by Juno and Cassini in the last year with the aim of determining, respectively, Jupiter and Saturn's gravity fields. The radio science investigation exploits the Doppler shift of a microwave signal to precisely determine the Earth-Spacecraft radial velocity and to estimate the gravity field harmonic coefficients, along with other dynamical parameters. The basic concepts of Doppler data and orbit determination are reported. A discussion on the estimated gravity fields is presented, as well as the implications for the interior structure of the Solar System's gas giants.

Acknowledgements

I would like to acknowledge my family, for the constant support, my friends, for the good time spent together, my advisor, for always providing useful discussions and opportunities, and my colleagues, for the precious advice and friendliness.

Contents

List of Figures

List of Tables

List of Abbreviations

AMC	**A**dvanced **M**edia **C**alibration
AWVR	**A**dvanced **W**ater **V**apor **R**adiometer
ASI	**A**genzia **S**paziale **I**taliana
C/A	**C**losest **A**pproach
CMS	**C**oncentric **M**aclaurin **S**pheroid
DOY	**D**ate **O**f **Y**ear
DSN	**D**eep **S**pace **N**etwork
DST	**D**eep **S**pace **T**ransponder
EOS	**E**quation **O**f **S**tate
ERT	**E**arth-**R**eceived **T**ime
ESA	**E**uropean **S**pace **A**gency
GPS	**G**lobal **P**ositioning **S**ystem
GRS	**G**reat **R**ed **S**pot
GWE	**G**ravitational **W**ave **E**xperiment
IAU	**I**nternational **A**stronomical **U**nion
JOI	**J**upiter **O**rbit **I**nsertion
KaTS	**Ka**-band **T**ranslator **S**ystem
MOI	**M**oment **O**f **I**nertia
NASA	**N**ational **A**eronautics and **S**pace **A**dministration
NON	**N**egative **O**rbit **N**ormal
OD	**O**rbit **D**etermination
OTM	**O**rbit **T**rim **M**aneuver
PLL	**P**hase **L**ock **L**oop
PRM	**P**eriod **R**eduction **M**anoeuver
PSD	**P**ower **S**pectral **D**ensity
RMS	**R**oot **M**ean **S**quare
RTG	**R**adioisotope **T**hermoelectric **G**enerator
SEP	**S**un-**E**arth-**P**robe
SYMPA	**S**eismographic Imaging Interferometer for **M**onitoring of **P**lanetary **A**tmospheres
TEC	**T**otal **E**lectron **C**ontent
TSAC	**T**racking **S**ystem **A**nalysis **C**alibration
TW	**T**hermal **W**ind

UTC **C**oordinated **U**niversal **T**ime
ZTD **Z**enith **T**otal **D**elay

Introduction

The exploration of Solar System is one of the most fundamental goals of humankind in recent years. The desire of reaching and overtaking the limits imposed on humans by nature has led to great discoveries in the past, and it still is one of the deep ambitions of any human. At the start of the space era, the conquest of the Moon in 1969 was driven by political supremacy of one state over another, nowadays the exploration of the space around the Earth has many objectives, but the exploration of the deep Solar System is intimately bound to scientific goals.

In the past number of years, the exploration of the planets in the outer Solar System has been pursed with many spacecraft. The only missions that have completed an orbit insertion around one of these planets are the Galileo and Juno missions for Jupiter, and the Cassini mission for Saturn, with no spacecraft for Nepture or Uranus. Galileo ended in 2003, Juno is still operative, and Cassini just reached its end in September 2017.

In this thesis I focused on Juno and Cassini, in particular, their gravity experiment for the determination of Jupiter and Saturn gravity fields, which hide answers to fundamental questions about the formation of the Solar System. The analysis of data acquired during Juno's gravity-dedicated orbits and Cassini's Grand Finale orbits is reported and the implications of the determined gravity fields are discussed.

In Chapter 1 a general overview on the exploration of gas giants and the Juno and Cassini missions is presented. Their role for answering the fundamental questions about our Solar System is discussed.

In Chapter 2 the interior structures of Jupiter and Saturn are reported. Then, the resulting gravity field is presented, and the main contributions highlighted: The effect of the rapid rotation, the contribution due to atmospheric dynamics, and the time-varying fields caused by normal modes.

In Chapter 3 the basics of orbit determination and a complete discussion on the radiometric data used for determining the gravity fields of the giant planets is reported. A discussion on the noise sources and the calibrations applied is also presented. In the case of Juno, the result for the Io Plasma Torus are shown. Then, the data analysis process is described for both Juno and Cassini.

To conclude, in Chapter 4 the gravity fields results are commented to infer proprieties of the interior structures of the two giant planets.

Chapter 1

The exploration of Gas Giants

The Solar System, formed about 4.6 billion years ago, consists of eight planets: the rocky planets, Mercury, Venus, Earth, and Mars; the gas giants, Jupiter and Saturn; and the icy giants, Uranus and Neptune. In addition, a large number of minor bodies (asteroids, dwarf planets, or moons) are also gravitationally bound to the Solar System.

The two gas giants, Jupiter and Saturn, contain about 92 % of the mass of all Solar System's planets, with Jupiter being more massive than the sum of the others, Saturn included.

Jupiter, which contains a large amount of the total Solar System's mass, the Sun excluded, is the key to understanding the formation process behind the Solar System. During the formation of the Solar System, the protoplanetary disk followed a series of events which led to the formation of the actual planets. Most of the initial mass was collected to form Jupiter, which therefore contains precious information about the Solar system formation and composition. The study of Jupiter, in particular the understanding of its internal composition, is a way to study processes that took place billions of years ago.

On the other hand, Saturn is the second largest planet in the Solar System. Like Jupiter, it contains a large amount of the protoplanetary disk mass. Although Jupiter also has a faint ring system, Saturn has the biggest and brightest planetary rings within the Solar System, which are indeed Saturn's most famous feature.

At Jupiter, NASA's Juno mission is currently investigating the deep secrets of the planet, with its suite of scientific instruments which includes a radio science experiment for gravity field determination.

At Saturn, NASA's Cassini mission has been collecting data about the Saturn system for almost 13 years. In the final part of its mission, the Cassini Grand Finale, prior to the deliberate plunge into Saturn's atmosphere on 15 September 2017, the spacecraft collected a large amount of data, including gravity field measurements for the study of Saturn's interior structure.

Jupiter and Saturn have much in common, and the possibility to study the gravity field, and thus the interior structure, of the two planets at the same time in history with Juno and Cassini missions is an incredible opportunity.

1.1 Juno at Jupiter

Juno was launched on 5 August 2011, and after 5 years of interplanetary cruise, completed the Jupiter Orbit Insertion (JOI) on 4 July 2016. The spacecraft was initially supposed to complete 33 orbits around Jupiter, each of them with a period of 11 days. Subsequently, the Juno team decided to switch to a 14-day orbit plan, to make operations easier. This option first included two 53.5-day period orbits after the JOI, prior to the Period Reduction Maneuver (PRM) which should have placed Juno in the nominal 14-day orbit. However, a problem with a valve of the propulsion system, which should have performed the PRM led to the postponement of the maneuver to an undefined date. Thus, Juno is currently in a 53.5-day orbit about Jupiter. The larger orbital period does not prevent the mission from accomplishing its scientific goals, and this is also the reason why the team did not risk performing the PRM.

Juno's primary objective (see Bolton, 2010) is to understand the formation and evolution of Jupiter through observations of Jupiter's gravity and magnetic fields, atmospheric dynamics and its composition.

In particular, Juno will focus on:

- Origins: The goal is to discover global properties of Jupiter (e.g. water abundance, core mass) that constrain the process of giant planet formation.
- Interior: The central goal is to use the gravity field, magnetic field and water abundance to determine the internal structure of the planet, core mass, the nature of deep convection and the process of magnetic field generation.
- Atmosphere: Juno will provide a three dimensional map of the atmosphere (to depth grater than 100 bars) providing water and ammonia abundances and characterizing dynamics of clouds and winds beneath the visible surface.
- Magnetosphere: Juno will investigate and characterize the three-dimensional structure of Jupiter's polar magnetosphere.

The last mission that studied Jupiter was NASA's Galileo mission, which focused mainly on Jupiter's Galilean satellites rather than on Jupiter itself. To achieve these goals, and enhance human knowledge about the largest planet in our Solar System, Juno has been equipped with nine scientific instruments:

- JADE, Jovian Auroral Distributions Experiment: It resolves the plasma structure of the Jovian aurora by measuring the angular, energy and compositional distributions of particles in the polar magnetosphere.

- JEDI, Jupiter Energetic-particle Detector Instrument: It measures the energy and angular distribution of Hydrogen, Helium, Oxygen, Sulfur and other ions in the polar magnetosphere.
- WAVES, Plasma Waves Instrument: It can identify the regions of auroral currents that define Jovian radio emissions and acceleration of the auroral particles by measuring the radio and plasma spectra in the auroral region.
- UVS, Ultraviolet Spectrograph: It records the wavelength, position and arrival time of detected ultraviolet photons every time Jupiter is visible by the spectrograph slit, at each turn of the spacecraft.
- JIRAM, Jovian Infrared Auroral Mapper: Its primary goal is to probe the upper layers of Jupiter's atmosphere down to pressures of 5-7 bars at infrared wavelengths in the 2-5 μm range using an imager and a spectrometer.
- MWR, Microwave Radiometer: Its goal is to probe the deep atmosphere at radio wavelengths ranging from 1.3 cm to 50 cm using six separate radiometers to measure the planet's thermal emissions.
- Magnetometer: The magnetic field investigation has three goals: mapping of the magnetic field, determining the dynamics of Jupiter's interior, and determination of the three-dimensional structure of the polar magnetosphere.
- KaTS, Ka-band Translator System: The primary objective of the Gravity Science Experiment is to determine the internal structure of Jupiter by making detailed measurements of its complete gravity field from polar orbit. The experiment is primarily a radio science experiment that uses the telecommunications system for transmitting data back to Earth to measure the precise position of the Juno spacecraft relative to Jupiter.
- JunoCam: This camera provides the first 3-color images of Jupiter as the Juno spacecraft approaches the poles for context and public engagement.

The scientific data acquired by Juno in the last months told us that most of the theories about Jupiter, from its internal composition to the structure of its magnetic field, were wrong. Essentially, Juno is rewriting our knowledge about Jupiter, the king of the gods according to Roman mythology, by providing the most accurate measurements of Jupiter's magnetosphere, auroras, and magnetic and gravity fields ever made.

As of September 2017, Juno completed seven perijove passes, two of them devoted to gravity field investigation. Table 1.1 summarizes the perijove passes completed so far.

The gravity science on Juno has been made possible with the onboard KaTS, Ka-band Translator System, which is able to provide coherent two-way Doppler measurements

Perijoves	Date	Scope
PJ01	27 August 2016	Generic science
PJ02	19 October 2016	Safe Mode
PJ03	11 December 2016	Gravity science
PJ04	2 February 2017	MWR measurements
PJ05	27 March 2017	MWR measurements
PJ06	19 May 2017	Gravity science
PJ07	11 July 2017	MWR measurements

TABLE 1.1: Summary of Juno perijoves.

in Ka-band (Ka/Ka link) with an exquisite accuracy. The KaTS supports the DST, Deep Space Transponder, used for navigation purposes. The DST provides coherent two-way Doppler measurements in X-band for the uplink and X or Ka-bands for the downlink (X/X or X/Ka links). However, the radio system was not designed to have a triple link simultaneously (X/X, X/Ka, and Ka/Ka) and the X/X link can be supported either by the X/Ka link (with the DST) or by the Ka/Ka link (with the KaTS). The Ka/Ka link along with an X/X link is used to partially calibrate dispersive effects on the Doppler measurements (Mariotti and Tortora, 2013; Bertotti, Comoretto, and Iess, 1993). The calibration can remove up to 75% of the plasma noise when compared with a Ka/Ka link (which benefits a reduction of plasma noise of a factor 16 when compared to an X-band link). As we will discuss in Chapter 3, the use of the Ka radio link is crucial for a good determination of Jupiter's gravity field.

The geometry of Juno's orbits also plays a crucial role in the determination of Jupiter's gravitational field. The orbits are highly elliptical, with a period of 53.5 days and an inclination of almost 90 degrees. The use of a polar orbit offers the opportunity to sample Jupiter's gravity while the planet rotates beneath Juno's trajectory. The very high eccentricity implies large velocity at the pericenter (almost 60 km/s), with Juno passing from the north pole to the south pole of Jupiter in only about 2 hours. Thus, the scientific investigation on the gravitational and magnetic fields must be performed in that short time frame. Juno's ground tracks are depicted in Figure 1.1.

The longitudinal coverage of Juno's passes will be uniform, in order to have a complete map of the planet's gravity and magnetic fields. Since the orbits are polar, the ground tracks are almost along the meridians, slightly shifted due to Jupiter's rotation. The first 4 orbits (minus PJ02 due to the safe mode) are shifted by 90 degrees, and the next 4 orbits cover the regions between the previous passes, thus producing a uniform map with a spacing of 45 degrees. Then, the following 8 orbits will further tighten the longitudinal map, as well as the last 16 planned orbits. The final map will thus have a spacing of 11.25 degrees (or 14 thousand kilometers at the equator).

For gravity science, just a limited number of orbits have been selected, therefore a

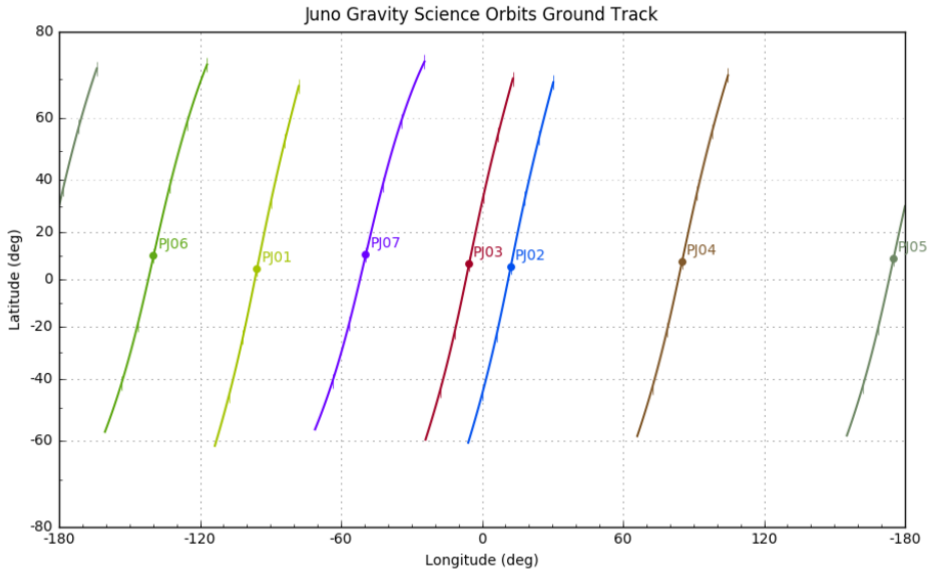

FIGURE 1.1: Juno ground tracks projected onto Jupiter's reference body fixed frame.

complete grid cannot be achieved. Currently, only 3 passes have been dedicated to gravity science, and a satisfactory coverage has not been obtained yet. However, as will be presented in Chapter 3, the gravity field of Jupiter is mostly symmetric, therefore a detailed map of Jupiter is not required to study global phenomena. Of course, an increased coverage helps to disentangle small effects, such as minor anomalies in Jupiter's gravity. An example will be the Great Red Spot, whose signature may be detectable by Juno (Parisi et al., 2016), depending on its penetration depth.

Figure 1.2 reports relevant quantities about Juno's orbital geometry. The large eccentricity and orbital period are responsible for the spikes in both the Juno-Jupiter distance (the spacecraft is very close to the planet in a very limited portion of time) and their relative velocity (which is large only close to the pericenter). The Sun-Earth-Probe (SEP) angle was more favorable in PJ06. The angle between the Negative-Orbit-Normal (NON) to the Earth was approximately 15 and 20 degrees for PJ03 and PJ06, respectively.

1.2 Cassini at Saturn

The Cassini-Huygens mission is a collaborative project of NASA, ESA, and the Italian Space Agency (ASI). Since its arrival at Saturn in 2004, Cassini has collected almost 13 years of scientific data on the atmosphere and magnetosphere of the gas giant, its icy moons, and its rings. Cassini has studied mostly the icy moons, making a lot of important scientific discoveries, the most remarkable being, perhaps, the discovery of an

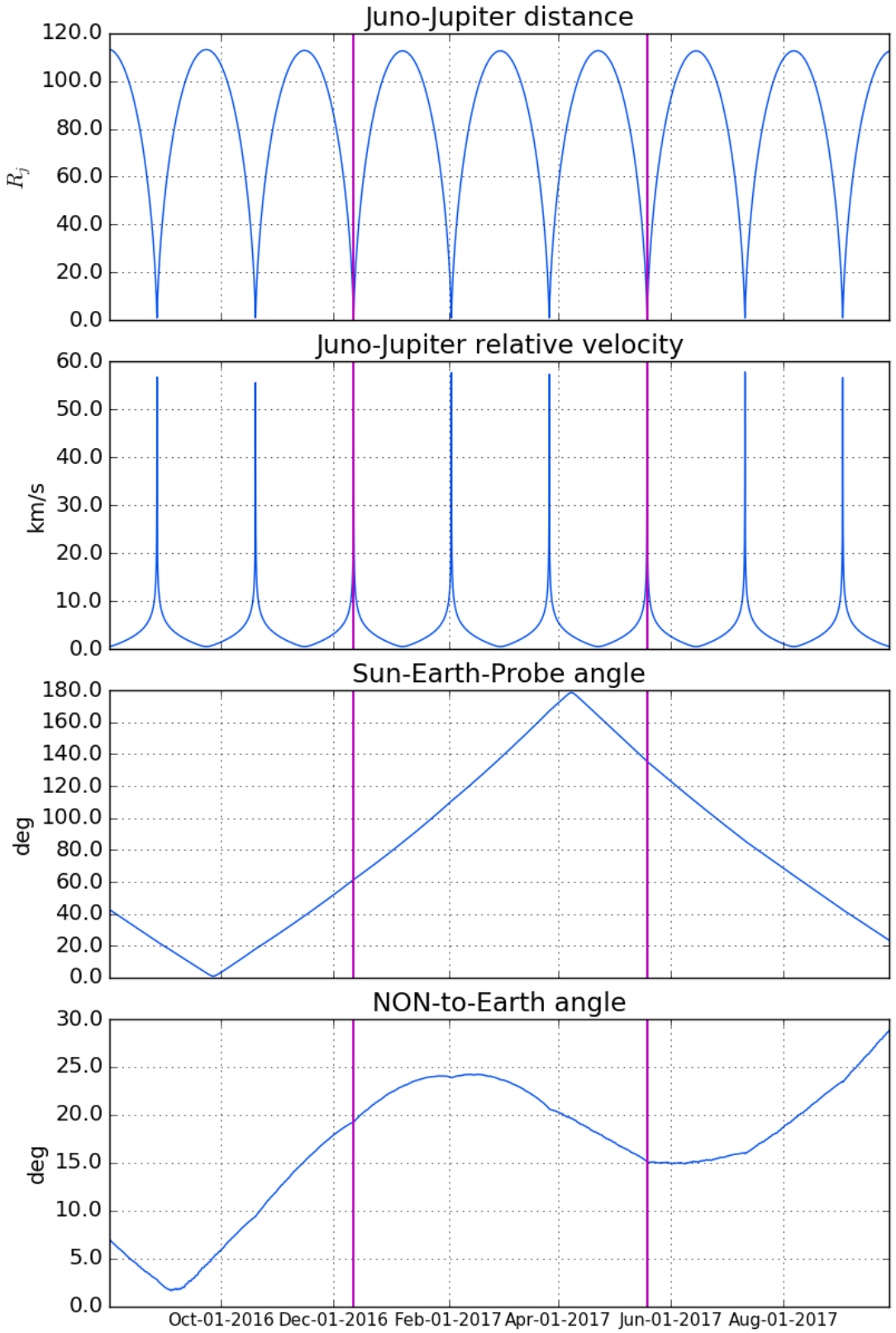

FIGURE 1.2: Juno's orbital characteristics. Vertical lines correspond to the two gravity passes, PJ03 and PJ06.

internal ocean beneath Enceladus' surface (Iess et al., 2014), which could potentially accommodate primordial forms of life.

The Cassini-Huygens mission was designed to explore the Saturnian system, including its rings and moons, with a special focus on Titan. The Huygens probe, carried by Cassini for the whole interplanetary cruise, was released on December 25, 2004, landing on Titan on January 14, 2005. The lander successfully returned data to Earth, using Cassini as a relay. Huygens was the first probe to ever land in the outer Solar System, returning precious images of Titan's surface.

Cassini carries 12 scientific instruments:

- CIRS, Composite Infrared Spectrometer: It is a remote sensing instrument that measures the infrared radiation from atmospheres, rings, and surfaces in the Saturnian system, studying their thermal properties.
- ISS, Imaging Science Subsystem: The instrument takes images mostly in visible light, but it also produced some infrared and ultraviolet images. It has wide angle and a narrow angle CCD cameras.
- UVIS, Ultraviolet Imaging Spectrograph: It captures images of the ultraviolet light reflected off an object to determine its composition and distribution. The instrument covers wavelengths in the 55.8 to 190 nm range.
- VIMS, Visible and Infrared Mapping Spectrometer: It captures images in visible and infrared light, to study the composition of moon surfaces, rings, and atmospheres.
- CAPS, Cassini Plasma Spectrometer: It measures the energy and electrical charge of particles from Saturn's ionosphere and magnetosphere.
- CDA, Cosmic Dust Analyzer: It measures the size, speed, and direction of tiny dust grains orbiting about Saturn.
- INMS, Ion and Neutral Mass Spectrometer: The instrument analyzes charged and neutral particles near Saturn and Titan, to study their atmospheres.
- MAG, Magnetometer: It measures the strength and direction of the magnetic field around Saturn, to study Saturn's magnetosphere and directly probe the core where electric currents are generated.
- MIMI, Magnetospheric Imaging Instrument: It produces images of the particles trapped in Saturn's magnetic field, to learn more about its interaction with the solar wind, rings, and satellites.
- RPWS, Radio and Plasma Wave Science: It measures radio signals coming from Saturn and its interaction with solar wind and Titan.

- Radar: The radar is both an active and passive sensing instrument, designed to produce maps of Titan's surface.
- RSS, Radio Science: The radio science instrument exploits radio waves to probe atmosphere and ring composition by looking at the changes on the transmitted signal. It can also provide accurate determination of Earth-Cassini relative velocities, crucial for locating the spacecraft within Saturn system and study the gravitational field of Saturn and its satellites.

The primary mission lasted 4 years, during which Cassini completed 44 Titan flybys and four targeted encounters with Enceladus, plus a few more flybys of other Saturn moons. In that phase of the mission, the Huygens probe was released into Titan's atmosphere.

Then, the mission was extended for two more years, and Cassini entered the 'Equinox mission' on July 2008. In fact, at that time Saturn was at the equinox, with its rings aligned with the Earth's direction. During that phase, Cassini continued the exploration of the Saturnian system, revealing additional details of Saturn's moons and rings. In particular, seven more flybys of Enceladus were performed.

Next, the 'Solstice mission' began on October 2010. It lasted 7 years (almost doubling the time of the previous two phases), considerably increasing the scientific return of the mission. Cassini's major objective in this phase was the monitoring of seasonal changes induced by varying solar illumination, caused by the progressive increasing of Saturn's ring (and equator) inclination with respect to the ecliptic plane.

The 'Grand Finale' was the final part of Cassini's journey, it lasted 5 months and ended with a deliberate plunge into Saturn's atmosphere on 15 September 2017. The spacecraft collected gravity and magnetic data from a distance as close as 2700 km from Saturn's cloud level.

In the Grand Finale, 22 orbits were planned, six of which were devoted to the study of the gravity field of Saturn. In the last number of years, Cassini never flew as close to Saturn as it did during the Grand Finale orbits. The determination of Saturn's gravity field was essentially obtained by following the orbital motion of its satellites, with uncertainties much larger than those achieved by Cassini during its closest passes to Saturn. Table 1.2 summarizes the orbits devoted to gravity investigations.

Particular attention was given to the possible independent determination of the ring's masses (in particular the most massive B-ring). In fact, Cassini passed between the cloud level and the rings, disentangling the weak gravitational signal of the rings from Saturn's large central field acceleration. Saturn's rings are named from A-ring to F-ring, plus a few divisions in between them. The B-ring is expected to be the most massive of Saturn's rings, followed by the A-ring and C-ring. They mostly consist of ice and rocks, with a thickness which varies from 5 to 30 meters. Spiral bending waves within the rings have

Proximal Orbits	Date of C/A
REV273	9 May 2017
REV274	15 May 2017
REV275	22 May 2017
REV278	10 June 2017
REV280	23 June 2017
REV284	19 July 2017

TABLE 1.2: Summary of Cassini's Grand Finale orbits devoted to Saturn's gravity investigation.

been essential for estimating the rings' surface densities and inferring their properties. In the B-ring, very few waves have been detected, and thus the determination of its mass is highly uncertain (Hedman and Nicholson, 2016). The other rings' surface densities are better constrained since a higher number of waves have been found. The B-ring is expected to contain about 70 to 85% of the total ring system's mass. The mass of the rings is an important parameter to better understand the origin of the ring system, and a more accurate determination of the ring masses will help to increase our knowledge of ring dynamics.

The ground tracks of the gravity passes provide a uniform coverage in longitude. Cassini's ground tracks are reported in Figure 1.3.

The geometry of the Cassini Grand Finale orbits is very interesting. The orbits are very eccentric (0.9) and the inclination with respect to Saturn's Equator is 62 degrees. The orbital period is about 7 days, and the pericenters are between Saturn's top clouds and the inner ring, which let Cassini fly for the first time inside the ring system. The latitude of closest approaches shifts from 5.5 degrees South to 7.5 degrees South, and the longitudinal coverage can inferred from Figure 1.3.

Figure 1.4 reports relevant quantities about Cassini's Grand Finale orbits. As in the case for Juno, the eccentric orbits produce spikes in both the Cassini-Saturn distance and their relative velocity. Vertical lines mark the epoch of the six gravity-dedicated closest approaches. The Sun-Earth-Probe (SEP) angle was favorable in all the passes. The angle between the Negative-Orbit-Normal (NON) and the Earth was favorable: the projection of the relative velocity to the line of sight was maximum, resulting in a large Doppler signal.

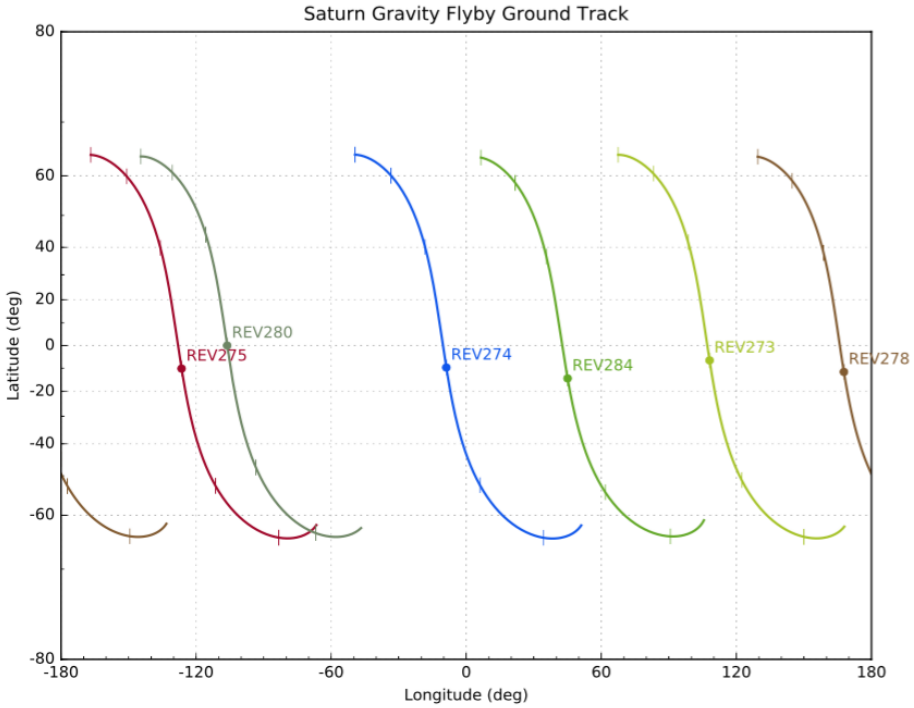

FIGURE 1.3: Cassini's ground tracks projected onto Saturn reference body fixed frame.

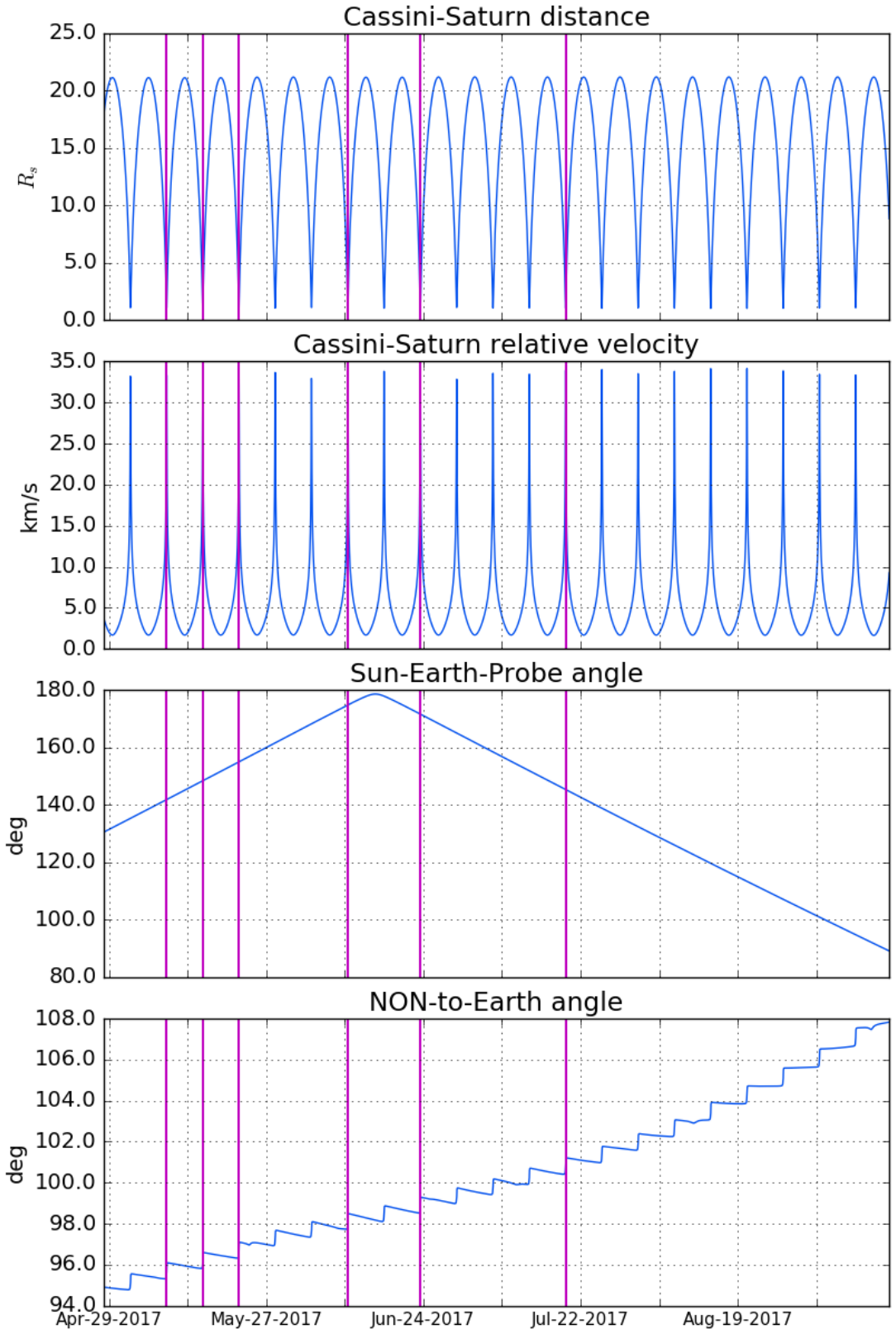

FIGURE 1.4: Cassini orbital characteristics. Vertical lines corresponds to the six gravity-dedicated passes.

Chapter 2

Jupiter and Saturn: interiors and gravity fields

2.1 Jupiter and Saturn interior structures

The understanding of gas giants' interior structures is a fundamental step toward our comprehension of the evolution of the Solar System. In fact, being the most massive planets, Jupiter and Saturn bare important information about the formation processes and the orbital evolution of our Solar System. Recent theories state that the gas giants should have formed 4.55 Ga ago, which is inconsistent with Jupiter and Saturn evolutionary models. Juno and Cassini, by determining the gravity field of the gas giants, and therefore providing observational constraints to their internal composition, are crucial in this context.

A simplified model for gaseous planets includes:

- A possible dense central core (made of "rocks" and "ice")
- A fluid envelope mostly made of hydrogen and helium (plus some heavier elements)
- An upper atmosphere, where clouds form

Concerning the core, by "rocks" we are referring to a combination of refractory materials and by "ice", more volatile species, such as water, methane or ammonia. The central core may have a definite boundary with the envelope or it could be dissolved within the envelope. The viscosity is supposed to be negligible throughout the whole planet due to the fluid state of the interior. The magnetic field can be neglected at first order, but the interaction with the interior structure is of great interest since it imposes limitations on the region where it must be produced.

The interior of giant planets is governed by the equation of state (EOS) of its components, that relates density, pressure, and temperature within the planet. It is the ensemble

of equilibrium thermodynamic properties of the interior materials. However, obtaining an accurate EOS for the interior of gas giants is extremely difficult since the pressure and temperature conditions found in the interior of these planets are difficult to reproduce in laboratory. Thus, accurate determination of the behavior of the interior components (which are known with some uncertainty) is extremely complicated. Also, the fluid is partially degenerate, and molecules, atoms, and ion can all coexist.

The major research so far has focused on the EOS of hydrogen, which is the main component found in the interior of gas giants. Near the upper atmosphere, the temperature is low (50 to 3000K), as is the pressure (0.1 to 10 bar), and the molecular hydrogen can be assumed to be a perfect gas. At deeper radii, the pressure increases, and the perfect gas hypothesis cannot be applied. Hydrogen tends to become fluid, and electron degenerate. At some point, around Mbar pressure, a molecular-to-metallic transition occurs. The details are, however, unclear, leading to large uncertainty in the EOS of the hydrogen. Also, different sets of experimental data acquired about the hydrogen EOS do not agree among themselves within the pressure range of interest. For a given EOS, the associated internal density profile can lead to multiple conclusions when constructing interior models with different EOSs (Miguel, Y., Guillot, T., and Fayon, L., 2016).

Regarding the gas giants' atmospheres, our knowledge is limited. The main components (H_2 and He) are difficult to detect since they have a zero dipole moment and their rotational lines are either weak or broad. In addition, in situ measurements are available only on Jupiter thanks to the Galileo probe, which probed only a limited region of the planet. A comparison of the abundance of the various species found in the atmospheres of giant planets with that measured in the Sun's atmosphere is crucial for understanding the processes that led to the formation of these planets. The Solar System's giant planets are all enriched in heavy elements compared to the Sun, i.e., the ratio between heavy elements (like Ar, Kr, Xe, C, N, or S) in these planets and those found in the Sun is higher than one. In addition, the relative enrichments increase with distance from the Sun. The uncertainties on these ratios are very large for the icy giants, whereas they are smaller for Jupiter and Saturn.

The combination of observation data and theories about the evolution of Jupiter and Saturn enabled the internal composition of the two gas giant to be inferred. A review on the structure of these two planets can be found in Guillot, 2005, which was written prior to both Juno and Cassini data.

In Figure 2.1, Guillot, 2005 reported a schematic representation of the interior of Jupiter and Saturn that matches all the observational constraints prior to recent data about the gravity fields of the two gas giants. The proposed models assume the presence of three main layers:

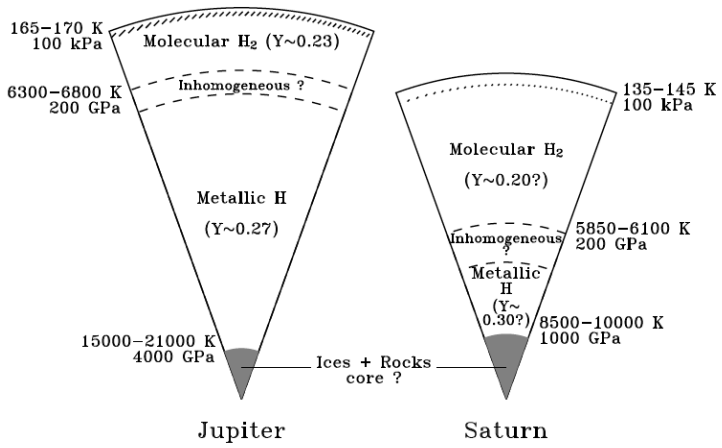

FIGURE 2.1: Schematic representation of the interior of Jupiter and Saturn, prior Juno and Cassini data (from Guillot, 2005).

- An outer hydrogen-helium envelope, whose composition equals that of the deep atmosphere
- An inner hydrogen-helium envelope, enriched in helium
- A central dense core

The main uncertainty on the interior structure is related to the long-standing question of whether a region in which helium separates from hydrogen to form helium droplets exists or not. This phenomena is referred to as helium rain, since the droplets are denser than the surrounding helium-poor mixture and start to rain down to the interior. In the case such a region exists, the location of this transition remains uncertain. Another source of uncertainty comes, as we said before, from the EOS of the hydrogen, which governs the density profile within the planet. For Saturn, the solutions depend less on the assumed EOS, since the Mbar pressure region is smaller than Jupiter's, and the total amount of heavy elements can be recovered with more accuracy.

2.1.1 Jupiter interior model

Like the Sun, Jupiter mostly consists of helium and hydrogen in hydrostatic equilibrium. However, Jupiter contains 3-13 % in mass of other (heavy) elements, whereas the Sun only has 2 % in mass of heavy elements. A detailed description of Jupiter's interior is given by Guillot, 2005, whereas Militzer et al., 2016 explain how the three layer models are constructed for Jupiter.

The internal temperature is about 20000 K, which implies that Jupiter's interior is fluid. The gas giant emits more energy than it receives from the Sun. This is a natural

result of the cooling and contraction of the planet. This energy drives convection within the majority of the interior, producing a temperature profile that is close to being adiabatic. The adiabatic behavior of Jupiter's atmosphere has been confirmed both by in situ measurements of the Galileo probe and by radio-occultation experiments by the Voyager spacecrafts.

Jupiter's atmosphere has been probed directly by the Galileo probe which measured the abundances of several species on the entry location. The helium mole fraction, denoted by q_{He}, obtained by the probe is:

$$q_{He} = 0.1359 \pm 0.0027 \tag{2.1}$$

The helium mass mixing ratio Y is obtained from:

$$Y/(X+Y) = 0.238 \pm 0.05 \tag{2.2}$$

X is the hydrogen mass mixing ratio. This value is lower than that inferred for the protosolar nebula, which implies that there was less helium in Jupiter's atmosphere when the planet formed than previously thought. One possible explanation is a phase separation of helium in hydrogen and the formation of heavy helium droplets, which fall deep into the interior due to gravity. This leads to an atmosphere denser than the material located just over the helium separation region.

The Galileo probe also measured the abundances of heavy elements: carbon, sulfur, phosphorus, krypton, xenon, and argon are all enriched in Jupiter's interior by a factor of 3 with respect to the Sun's atmosphere. The oxygen enrichment is yet unknown, due to difficulties caused by meteorological phenomena, but its determination could help to achieve Juno's goal of understanding Jupiter's interior.

Concerning Jupiter's magnetic field, like that of the Earth, it is likely generated by a dynamo process, arising through convective motions in the deep interior, which is thought to be electrically conductive. Jupiter's dipole is tilted by 9.6 degree with respect to the rotation axis, similar to the Earth's tilt. By comparing the magnetic field coefficients of Jupiter, there are indications of a magnetic boundary at about 0.75 to 0.8 Jupiter radii.

One of the most important aspects when determining Jupiter's internal structure is the equation of state. Gas giants are composed of a fluid mixture of hydrogen, helium, and heavier elements. Due to the high pressure found in the interior, it is very difficult to study either theoretically or experimentally the characteristic of such a mixture. Experimental data about the hydrogen EOS is generally achieved in laboratories by means of shock-compression experiments of small samples. However, the range of pressure and temperature achievable is limited. On the contrary, first-principles computer simulations can overcame the experimental difficulties by obtaining the EOS from numerical simulation.

In the outer regions of the planet, the pressure and temperature are low and hydrogen is a molecular fluid. Deeper into the planet, the pressure increases, and the fluid becomes ionized so that the ions undergo strong Coulomb interactions. This particular state is referred to as liquid metallic hydrogen. However, the region where the transition between the two states happen is poorly understood. It can be either a continuous transition or rather a first order phase transition (called the plasma phase transition), with a sharp change in density and entropy. If the plasma phase transition exists, the implication for Jupiter's interior would be important. In fact, it would create a barrier for convection between the outer envelope and the metallic interior, affecting the mixing of heavier elements.

The equations of state governing Jupiter's interior also involve the helium EOS, which is poorly known too. The comprehension of how the hydrogen-helium mixture behaves within Jupiter first requires a knowledge of the EOS, then understanding of the interactions of the two elements.

In addition, the mixture is also composed of heavy elements. An approximate treatment of the equations of state for these elements is generally sufficient, due to their small molecular abundances. Unfortunately, the amount of each species is unknown but they are supposed to be uniformly mixed throughout the envelope thanks to convection. Among the heavier elements, water is especially important because it can contribute to as much as half of the total mass of heavy elements contained in Jupiter.

The general picture of Jupiter's interior sees it divided into a minimum of three layers. As previously anticipated, these regions are:

- A helium-poor molecular hydrogen envelope (including the atmosphere)
- An inner helium-rich metallic hydrogen envelope
- A central dense core of unknown composition

The division between helium-rich and helium-poor envelopes is due to the low atmospheric abundance, and the different composition is easily explained with a plasma phase transition. The presence of a core is generally required by gravity measurements, but no clues on its composition have been found.

The three-layer model is obviously a simple model, and the general picture for Jupiter's interior may be more complex since it has to account for all the observational constraints and theoretical assumptions. Such a simple model is fully determined by only three main parameters: The mass of the core, M_{core} and the mass mixing ratio of heavy elements in the outer and inner envelopes, Z_{mol} and Z_{met}, respectively. The helium mixing ratio in the outer envelope is set as the atmospheric value, whereas that of the inner, metallic, envelope is computed as having the total helium/hydrogen ratio equal to the protosolar value, since Jupiter obviously formed from the protosolar nebula.

The central core has either a well-defined boundary or it can be dissolved in the envelope. For Jupiter, this question remained for long without an answer (Guillot, Gautier, and Hubbard, 1997). It is intimately related to the origin of the envelope enrichment. Attempts to solve this question start from gas giant formation theories. A first explanation is that the central core is formed from the protosolar nebula, and then the envelope is enriched after the formation, clearing the residual nebula. However, this scenario, referred to as the late accretion of planetesimals, is not supported by dynamical simulation, since the achievable enrichment in both Jupiter and Saturn is too small to explain the observed enrichment values in Jupiter's atmosphere.

Another scenario proposes a rapid accretion of the central core of a gas giant, with a low-metallicity envelope. In this case, the core is eroded to enrich the gaseous envelope with heavy elements. The erosion of the core consists of downward convective plumes, which penetrate the core, and mix the poorly enriched envelope with the dense central core with a large amount of heavy materials. Simulations shows that, in this scenario, Jupiter would become more enriched with respect to Saturn, which agrees with interior models that expect a larger core mass for Saturn. In addition, first-principles simulations for the hydrogen-helium mixture have been used to explore Jupiter's core (Militzer et al., 2008). The resulting EOS imply a massive central core of 14-18 Earth masses of heavier elements, supporting core accretion scenario for Jupiter's formation.

2.1.2 Saturn interior model

A detailed review of Saturn's interior is given in Fortney et al., 2016. Along with Jupiter, Saturn is a natural laboratory to study the physics of hydrogen and helium under high pressure. These two components were predominately found in the protosolar nebula, and Saturn's composition is associated with the formation process of our Solar System.

Even though Jupiter and Saturn have a lot in common, there are a few differences which elect Saturn as an interesting point of comparison with its larger companion Jupiter. As heavily discussed in the previous section, Jupiter's interior is highly sensitive to the hydrogen EOS, whereas Saturn, being 30% of Jupiter's mass, covers a smaller region of the hydrogen phase diagram, and its interior does not reach the high pressure found in Jupiter. In any case, Saturn has its own set of peculiarities, such as the axially symmetric magnetic field or its high intrinsic luminosity, which makes it equally interesting. In addition to Jupiter, Saturn's famous rings proved to be a very accurate seismograph, showing the internal waves traveling within Saturn's interior.

Hydrogen is the most abundant element within Saturn's interior. Its equation of state is the most important physical input to depict a true picture of the interior of giant planets. For that reason, both experimental and theoretical work has been done in the past

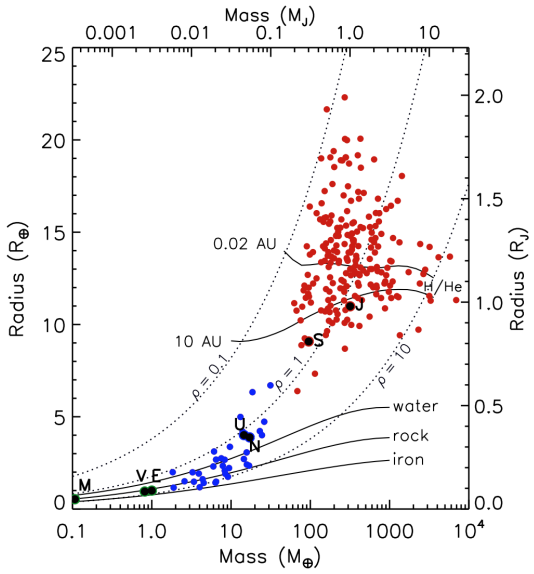

FIGURE 2.2: Mass-Radius relation for several planet (red color is for planets more massive than 0.1 M_j). Solar System's planets are labeled by their first letter. Dotted lines are curves of constant bulk density. (Fortney et al., 2016)

number of years to better understand the behavior of hydrogen under high pressure, such as that found in the interior of Saturn or Jupiter.

Another important basic physic concept is related to the mixture of hydrogen and helium. Deviation from the linear mixture of the two components have been widely studied in the past number of decades. There are suggestions that helium may phase separate from liquid metallic hydrogen at the condition found in the gas giant. A helium-rain region is supposed to exist within the planet.

On the contrary to Jupiter, Saturn is believed to possess a larger percentage of heavy elements. At first order, this is easily seen in the mass-radius relation for planetary and astrophysical objects. The bulk composition can be inferred by simply computing the mean density:

$$\bar{\rho} = \frac{3M}{4\pi R^3} \tag{2.3}$$

with M and R being the mass and radius of the object respectively. On the mass-radius diagram (see Figure 2.2), Saturn shows a mean radius R lower than expected for a planet at its distance from the Sun and with a solar composition. The mean density is thus larger than expected, hinting at an enrichment of the interior with heavy elements.

Concerning Saturn's atmosphere, it can set important constraints on the interior structure and formation process. If the outer envelope is fully convective and well-mixed, the atmospheric abundances of heavy elements equal those of the envelope. However, unlike

Jupiter, Saturn has not been probed by an entry probe and therefore, no in-situ measurements are available. The only abundance that has been determined for all the four Solar System's giants is that of Carbon, found in methane, which shows an increase with decreasing planet mass. For Saturn, the enrichment with respect to the solar value is ~ 10 (Fletcher et al., 2009). This suggests a hydrogen-helium envelope which is strongly enriched with heavy elements. However, the abundances of water and ammonia are yet unknown, and would correspond to about 60 to 80% of the heavy element mass.

Jupiter's magnetic dipolar moment is $M_{jup} = 4.27\ Gauss\ R_j^3$ whereas Saturn's moment is one order of magnitude smaller, $M_{sat} = 0.21\ Gauss\ R_s^3$. The first measurement of the dipolar component of Saturn's magnetic field was made by Pioneer 11 Saturn flyby in 1979, and the subsequent Voyager and Cassini missions have shed further light on Saturn's gravity field. Saturn's magnetic field is different from Jupiter's: Saturn's axial tilt is less than 0.06 degrees (below current accuracy), so extremely axisymmetric. Saturn's axial symmetry is strikingly different from other planetary magnetic fields. Both the Earth and Jupiter have a large dipolar tilt. It has been suggested that the measured field is generated in Saturn's outer region, so that the internal, deep-seated, magnetic field might have the same characteristics of those belonging to Earth and Jupiter.

With the conventional approach, it is possible to infer a "core radius" by computing the radius at which the octupole component of the field is of the same order of the dipole component. For Saturn, this computation reveals a value of $R_{core} \approx 0.47\ R_s$, which is pretty close to the value at which hydrogen becomes highly conductive. This is a first order computation and the result must not be over-interpreted.

Another long-standing question about Saturn is related to its rotation rate, which is still not well constrained. For Jupiter, a measurement of the rotation rate is possible thanks to its magnetic field, which is tilted with respect to the rotation axis and thus the dipole rotates with the planet, allowing a measurement of the rotation rate of its interior. For Saturn, such a measurement is impossible due to the axial symmetry of its magnetic field. Current measurements of Saturn's rotation rate come from Voyager 2 and Cassini data on the periodicity of Saturn's kilometric radiation, emitted from the interior. However, the same exact technique ended with two different results: 10h 39m 22.4s from Voyager 2 and 10h 47m 6s from Cassini. In addition, Cassini has confirmed a time-dependence in Saturn's auroral radio emission. Thus, the real uncertainty on Saturn's rotation rate is of several minutes.

The uncertainty of the rotation rate has several implications for Saturn's interior structure. First, it directly affects the gravitational field of the planet, and a wrong value may lead to a different interpretation of the gravity field data. Second, the wind magnitude is directly affected by the rotation rate, since the cloud motion must be referred to a known rotation rate. In addition, Saturn can rotate differentially on cylinders and the interpretation of its rotation rate is tricky.

Recently, analysis of ring occultation data revealed the presence of Saturn's normal modes, which resonate with the ring producing structures observable in the Cassini data. Seismology is an important technique to constrain the interior of a planet. For the Earth, waves generated by earthquakes have been essential for studying the internal composition, constraining the structure of the Earth, such as the location of its core. For the Sun, the analysis of acoustic oscillations revealed crucial information for the interior of our star. Thus, nowadays, research of seismic activity in the gas giants is a natural consequence to help us understand their interior structure.

A gaseous sphere can oscillate in several ways. The resulting modes are named according to the restoring force: Pressure (p-)modes and gravity (g-)modes. The latter are present only in non-isentropic models, or when density discontinuity is assumed. The oscillation frequencies are strongly related to the interior structure, and thus can be used to make inferences on the deep interior (Jackiewicz et al., 2012). In the case of Saturn, the oscillation frequencies can be accurately measured since they produce resonance within the rings. The data obtained by Hedman and Nicholson, 2013 and Hedman and Nicholson, 2014 confirmed that the origin of the feature seen in the rings is associated with acoustic, fundamental modes (radial order $n = 0$). Recently, Fuller, 2014 explained the oscillation frequencies stating that a mixing of fundamental $\ell = 2$ mode with gravity modes, generated through a convectively stable region above Saturn's core, would produce the observed frequencies. To conclude, seismology has proved to be a good useful tool to study the interior structure of gas giants.

2.2 Gravity fields

Measurements of the gravity field of a planet are essential for constraining the internal density profile, and rule out models that do not match the observations. In particular, an accurate measurement of the gravity field coefficients is important to assess the presence of differential rotation in the interior of the planet. In fact, the observed zonal flow can either be a surface phenomenon, or extend deep into the planetary interior, affecting the density distribution and producing large gravitational disturbances that can be measured with the Juno and Cassini missions.

The gravity field of a gas giant planet has the following main contributions:

- Solid body rotation
- Atmospheric dynamics
- Normal modes

The solid body contribution is related to the fast rotation of the planet as the Coriolis forces arise and distort the planetary shape. The gravity field thus deviates from that of a resting sphere.

The atmospheric dynamics visible on the upper layer of the gas giants perturb the interior pressure profile, down to a depth unknown prior to Juno and Cassini data, causing changes in the density profile and thus a complex gravity field spectrum.

Normal modes of giant planets are, in principle, able to perturb the interior density profile, producing a time-varying gravity field (Durante, Guillot, and Iess, 2017). The intensity of the gravitational disturbance depends on the amount of energy involved, which is actually unknown.

Each contributor has a characteristic time scale. The solid body contribution is driven by the planet rotation rate, which slowly changes over centuries. The atmospheric dynamics have shorter time scale, approximately a few decades. Normal modes can change according to the phenomena that drives them, which are unknown, but it is believed they have shorter time scales.

2.2.1 Solid body rotation

The solid body rotation term represents the gravity field of a perfectly symmetric rotating fluid planet, whose rapid rotation affects the gravitational shape of the planet.

Jupiter and Saturn are two fast spinning planets: Jupiter's rotation period is (as determined by Jupiter's radio emission and magnetic field) 9 hours, 55 minutes, and 30 sec, whereas Saturn's rotation period is 10 hours and 33 minutes, with a larger uncertainty.

The fast rotation rates largely affect the planetary shapes. On the surface, the ratio between the centrifugal force and the gravitational force is a key parameter to understanding the planets themselves. It is easy to compute these values:

$$q = \frac{\omega^2 a^3}{GM} \rightarrow \begin{cases} q_{jup} = 0.089 \\ \\ q_{sat} = 0.158 \end{cases} \tag{2.4}$$

Saturn's small parameter q_{sat} is larger than Jupiter's q_{jup}. The centrifugal force on the surface of the two planets is of the same order, but Jupiter's gravitational acceleration at the surface is more than two times larger than Saturn's. Thus, we expect Saturn to deviate more than Jupiter from the spherical symmetry. The two ratios can be compared with the Earth's value of $q_{earth} = 0.0034$.

The usual approach to describe the shape of a gas giant planet expands the gravity field in a power series of that small parameter (actually, a slightly different parameter). A new numerical approach, presented by Hubbard (Hubbard, 2012; Hubbard, 2013), aims at computing, to computer precision, the shape of a gas giant planet. The Concentric

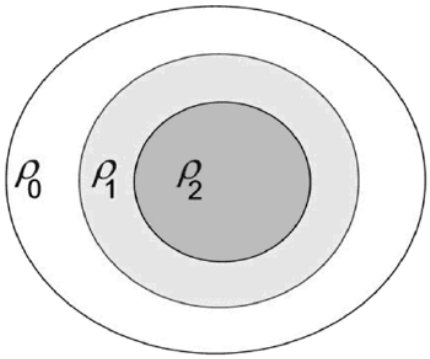

FIGURE 2.3: Schematic of the N-layers of constant density approximation of a planet (from Hubbard, 2013).

Maclaurin Spheroids (CMS) express the exterior gravitational potential by studying the gravitational potentials of a planet made by N-layers of constant density. A schematic concept of the method is reported in Figure 2.3, and well described in Hubbard, 2013.

The CMS method is a very powerful tool able to compute the gravitational potential of a planet such as Jupiter or Saturn, starting from an interior density profile, and eventually imposing the model to satisfy a given equation of state (EOS), which provides the pressure-density relation. The difference between the CMS method and the well-known theory of figures has been analyzed in Nettelmann, 2017

The resulting gravity field depends on the interior density structure, and thus is affected by the presence of a core (diluted or not) or by the amount of heavy metals in the envelope. In any case, the resulting gravity field is symmetric about the rotation axis, and the solid body contribution provides only even gravity coefficients. The gravity field writes:

$$U(r,\theta) = \frac{GM}{r}\left\{1 + \sum_{i=1}^{\infty}\left(\frac{R}{r}\right)^{2i} J_{2i} P_{2i}(\cos\theta)\right\} \tag{2.5}$$

A set of preliminary Jupiter models is given in Hubbard and Militzer, 2016, published before Juno's arrival. The authors explored different plausible theories of Jupiter's interior structures, and computed the corresponding spherical harmonics coefficients. The gravity spectrum for their preferred model (DFT-MD 7.13) is given in Figure 2.4.

For Saturn, S. Wahl provided (private communication) a range for the even gravity coefficients for preliminary Saturn's interior model, computed with the CMS method. The models all match the observation constraints available before Cassini Grand Finale orbits, when the gravity field of Saturn were determined essentially through Saturnian ephemeris motion. No differential rotation have been assumed. Figure 2.4b reports the gravity coefficients.

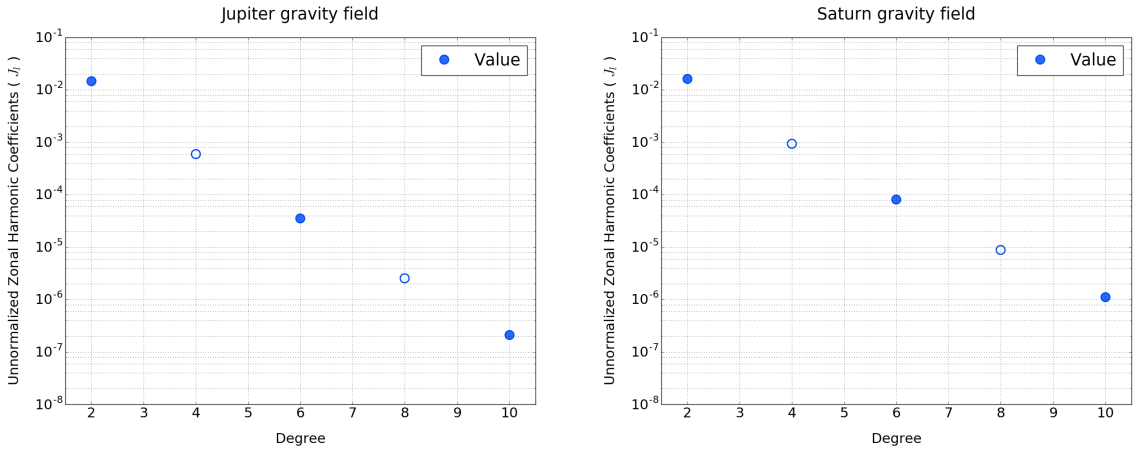

(A) (B)

FIGURE 2.4: Solid body contribution for Jupiter's model DFT-MD 7.13 from Hubbard and Militzer, 2016 (panel A) and preferred model for Saturn from Wahl, S., private communication (panel B).

Due to Saturn's larger q (see Eq. 2.4), its gravity spectrum shows larger values for the gravity coefficients than Jupiter's.

2.2.2 Atmospheric dynamics: effect on gravity fields

The solid body rotation is not the only contribution to the static gravity field of a planet. In fact, gas giants have an atmosphere that may extend, in principle, down to the center of the planet, thus deeply affecting the exterior gravity field.

The atmospheres of both Jupiter and Saturn are famous for their banded structures, caused by the large zonal jets which flow on the surface of the planets. In addition, Jupiter has many local structures, for example spirals and ovals, such as the Great Red Spot (GRS), which complicate the picture of the planet's winds.

The winds produce changes in the velocity profile of the upper part of the planets, which translate into pressure variations, and thus density variations. the exterior gravity field is perturbed according to the wind penetration depth (Hubbard, 1999; Kaspi et al., 2010). The only in situ measurement was been made by the Galileo probe, which entered into Jupiter's atmosphere measuring a wind velocity of 160 m/s at its deepest penetration depth, at 22 bar (0.2% of the planetary radius). At the same location, 6.6°N, the wind speed inferred by cloud tracking is roughly a factor of two lower. However, we do not know if this is a global characteristic of the planet or, more likely, just a local feature of Jupiter's atmosphere. The question of whether the atmospheric flows decay or increase with depth is still unresolved.

The winds may be the surface manifestation of a much deeper-seated circulation. The first tentative analysis of the effect of atmospheric dynamics on Jupiter's gravity field

has been to suppose that the observed surface zonal flows extend to the interior along cylinders parallel to the axis of rotation (Hubbard, 1999), i.e. the interior of Jupiter (and gas giants in general) is rotating along cylinders. Therefore, the interior structure suffers a differential rotation, which further deforms the planetary shape with respect to the idealized solid body rotation flattened sphere. Therefore, the even gravity coefficients must be adjusted.

The magnitude of the effect depends on the penetration depth of the winds. The extreme case is when the winds do not decay along the cylinder, and the speed of the interior equals the surface wind speed. However, in this case the velocity profile should be adjusted in order to have a match between the northern and southern hemisphere wind profiles. The simplest approach is to propagate the norther hemisphere wind profile downward and then repeat the computation of the gravity spectrum with the southern hemisphere wind profile, propagated upward (Hubbard, 1999). The resulting gravity fields differ, but both show a break in the spectrum of Jupiter's gravity harmonics at about ℓ=10 if the differential rotation primarily occurs on cylinders. In addition, we can state that for these higher order harmonics, the gravity spectrum is dominated by the dynamics, since the solid body contribution becomes negligible (see Figure 2.4).

Another approach starts from the basics of atmospheric circulation. The thermal wind (TW) balance relates the velocity field to the density perturbation, and allows the computation of the change in the gravitational field of the planet. The thermal wind model is more flexible, and can easily account for velocity discontinuity at the equator, and thus also solve for odd harmonics.

In these models, the surface wind profile extends parallel to the axis of rotation, with an exponential decay with depth:

$$u(r,\theta) = u_{cyl}\, e^{-(\frac{R-r}{H})} \tag{2.6}$$

This empirical model has proven to be very useful and powerful, mainly due to its simplicity. The free parameter H, the scale height of the exponential decay of the surface winds u_{cyl}, allows the gravitational signal to be studied in terms of changes in the gravity harmonics, or ΔJ_n, with different wind profiles. As one can expect, a larger value for the scale height H produces larger deviations from the solid body rotation. The extreme case of non-decaying winds can be obtained by imposing $H \gg R$, so that the interior wind profile is identical to the surface winds.

Since both Jupiter and Saturn rotate fast, to the leading order the planet is in geostrophic balance, and the thermal wind relation must hold:

$$(2\Omega \cdot \nabla)[\tilde{\rho} u] = \nabla \rho' \times g_0 \tag{2.7}$$

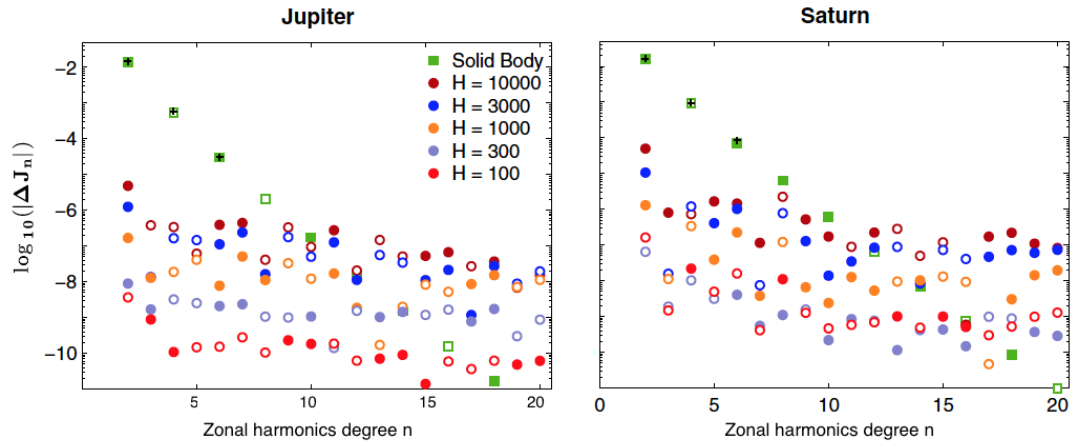

FIGURE 2.5: Thermal wind contribution for different penetration depths, from Kaspi, 2013.

The planet's rotation rate is identified by Ω, $\tilde{\rho}$ is the hydrostatic state density, coming from the internal density profile, and ρ' is the density anomaly due to the winds. The vectors u and g_0 are, respectively, the full 3-D velocity field and the mean gravity vector. Solving Eq. (2.7) allows the density perturbation to be computed, and thus the corrections to the gravity coefficients is given by:

$$\Delta J_l = -\frac{1}{MR^l}\int_0^R r^{l+2}\int_0^{2\pi}\int_{-1}^{1} P_l(\mu)\rho' d\mu d\phi \tag{2.8}$$

The mass and reference radius are denoted, respectively, by M and R. The cosine of the colatitude is μ, and ϕ is the longitude.

The northern wind profile is not identical to the souther's, in both Saturn and Jupiter, and thus odd harmonics are expected to be non-zero. Since the gravitational field coming from the solid body rotation produces only even harmonics, any non-zero value detected from Juno for the odd harmonics is related to the wind dynamics (Kaspi, 2013).

The measurement of odd harmonics is very important to discriminate the contribution of zonal jets, and thus answer one of Juno's main goals: what is the depth of the zonal winds? The same measurement is, of course, also valid for Cassini and Saturn.

The expected contribution from the zonal winds, according to the TW model, is reported in Figure 2.5, both for Saturn and Jupiter.

In Figure 2.6 the contribution to the first low degree odd harmonics is reported both for Saturn and Jupiter. The model predicts a value, and a particular sign, for these harmonics according to the penetration depth of the winds.

The thermal wind model can be greatly improved and expanded. For example, a latitudinal dependence of the scale height parameter can be easily included and different

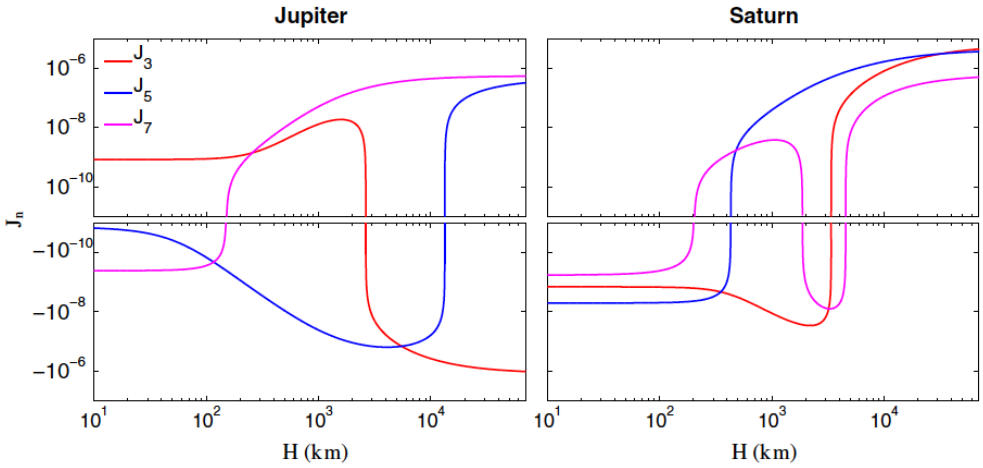

FIGURE 2.6: Thermal wind contribution to low degree odd harmonics for different penetration depths, from Kaspi, 2013.

decay profile are possible. In particular, the effect of Jupiter's magnetic field and its internal conductivity has been studied to assess the influence on the wind profile (Galanti, Cao, and Kaspi, 2017).

The gravity signal of vortices

Following the same approach, Parisi et al., 2016 expanded the thermal wind model to compute the density perturbation starting from a 2-dimensional map of the surface cloud winds (Choi et al., 2007). The new method allows the presence of vortices in Jupiter and Saturn (their work focuses on Jupiter) to be taken into account and computes the deviation induced to the gravity field. The resulting gravity field also produces perturbations on the tesseral field, i.e. predicts non-zero tesseral gravity coefficients, associated with the finer structure of the surface winds. The 2-D wind velocities are supposed to extend in a direction parallel to the rotation axis, in order to conserve the total angular momentum. As in the previous case, an exponential decay over the radius is permitted:

$$u(r,\theta,\phi) = u_{cyl}\, e^{-(\frac{R-r}{H})}$$
$$v(r,\theta,\phi) = v_{cyl}\, e^{-(\frac{R-r}{H})} \tag{2.9}$$

The zonal component of the velocity is u whereas v is the meridional component. The radial direction has a zero velocity. The thermal wind balance can be extended in a 2-dimensional space and allows the computation of the correction to the tesseral field components of the gravity field:

$$\Delta C_{lm} = \frac{1}{MR^l} \int_0^R r^{l+2} \int_0^{2\pi} \int_{-1}^1 P_l(\mu) \cos(m\phi) \rho' d\mu d\phi$$
$$\Delta S_{lm} = \frac{1}{MR^l} \int_0^R r^{l+2} \int_0^{2\pi} \int_{-1}^1 P_l(\mu) \sin(m\phi) \rho' d\mu d\phi \tag{2.10}$$

The vortices are supposed to have, in principle, a different scale height with respect to the zonal flows. The zonally mean wind has a decay scale height H_1, and the deviations from these decay with H_2. For Jupiter, the main contribution to the gravity field is associated with the Great Red Spot, which is of great interest. The result from Parisi et al., 2016 shows that for winds that decay in the same way between zonal and non-zonal flows, the GRS signature can be observed if the winds penetrate with $H > 2000km$, otherwise the threshold for GRS detectability is determined by the extension of the main zonal flows. Note that the simulations were carried out using the old 11-day reference orbits; in the new orbital configuration we do not expect to have a significant difference in the expected results.

2.2.3 Normal modes

An interesting emerging method to probe the interior of a gaseous planet is through the determination of its acoustic normal modes. Seismology is a unique method to probe the interiors of giant planets, since acoustic modes propagate down to the core, and are affected by the internal structure of the planet. The nature of these modes has been studied for pulsating stars, but is yet poorly known for giant planets (Dederick and Jackiewicz, 2017).

Currently, acoustic modes have barely been detected in Jupiter and Saturn. For Jupiter, the only, controversial, observation has been made by Gaulme et al., 2011. Their instrument, SYMPA (Seismographic Imaging Interferometer for Monitoring of Planetary Atmospheres), a Fourier tachometer whose principle is based on the spectro-imaging of the full planetary disk, detected an excess power between 800 and 2100 μHz and a secondary excess power between 2400 and 3400 μHz, as well as a characteristic splitting of the peaks of 155.3 $\pm$ 2.2 μHz. All of these are compatible with frequencies of acoustic oscillations predicted by interior models of Jupiter. However, the amplitude of the observed modes claimed by these authors are quite large and still unexplained, leading to skepticism.

Concerning Saturn, the rings were crucial for identifying acoustic modes inside the planet (Hedman and Nicholson, 2013; Hedman and Nicholson, 2014). Some of Saturn's acoustic oscillations have a period which resonates with the rings' particles, generating waves within the rings. These waves are clearly detected in Cassini's ring occultation data, leading to the identification of a few modes. The observed oscillation spectrum has been used to reveal a stably stratified region within the planet (Fuller, 2014). The

amplitude of these modes is poorly known, but observations hint at smaller amplitudes when compared to Jupiter's observed modes.

While these oscillations are certainly a potential source of information on the radial density profile, they may also complicate the interpretation of Juno and Cassini gravity data. Normal modes displace large masses that may perturb the spacecraft motion to levels that can be measured by Juno's extremely accurate Doppler system or by Cassini during the Grand Finale orbits.

In order to evaluate the perturbation of the gravitational field produced by acoustic modes, we consider the harmonic expansion of the gravitational potential:

$$U(r,\theta,\varphi) = -\frac{GM}{r}\left\{1+\sum_{l\geq 2}\sum_{-l\leq m\leq l}\left[\left(\frac{R}{r}\right)^{l} U_{l,m}\, Y_{l,m}(\theta,\varphi)\right]\right\} \tag{2.11}$$

With the usual convention, R is the planet's reference radius, r is the radial coordinate, θ is the colatitude, and φ is the longitude at which the potential is computed. The normalized spherical harmonic of degree l and order m is denoted by $Y_{l,m}(\theta,\varphi)$.

The internal density distribution $\rho(r)$ determines the spherical harmonic coefficients $U_{l,m}$ through (Bertotti, Farinella, and Vokrouhlick, 2003):

$$U_{l,m} = \frac{\int_V r'^{l}\, Y_{l,m}(\theta',\varphi')\, \rho(P')\, dV}{(2l+1)\, M\, R^{l}} \tag{2.12}$$

The integral is computed over the volume of the reference sphere, with the volume element $dV = r'^{2}\, sin\theta'\, dr'\, d\theta'\, d\varphi'$. The density is computed at the internal point P', normalized by the total mass of the planet, M.

The internal density profile is perturbed by acoustic oscillations, thus:

$$\rho(r',\theta',\varphi',t) = \overline{\rho}(r',\theta',\varphi') + \sum_{l\geq 2}\sum_{-l\leq m\leq l}\sum_{n\geq 0}\left[\Delta\rho_{l,m,n}(r',\theta',\varphi',t)\right] \tag{2.13}$$

The internal, unperturbed density profile $\overline{\rho}(r',\theta',\varphi')$ is disturbed by the superposition of the perturbations, $\Delta\rho_{l,m,n}(r',\theta',\varphi',t)$, characterized by different degrees and orders. Each of these density perturbations must conserve the total amount of mass, and its temporal average over long time-scales must be zero. Thus, they must satisfy:

$$\int_V \Delta\rho_{l,m,n}(r',\theta',\varphi',t)\, dV = 0 \tag{2.14}$$

$$\overline{\Delta\rho_{l,m,n}}(r',\theta',\varphi',t) = 0 \tag{2.15}$$

The Eq. (2.14) and (2.15) must be satisfied for all allowable degrees and orders. The density perturbation can be written as:

$$\Delta\rho_{l,m,n}(r',\theta',\varphi',t) = \widetilde{\Delta\rho}_{l,m,n}(r',\theta',\varphi')\ \cos(\omega_{l,m,n}t + \phi_{l,m,n}) \tag{2.16}$$

The term $\widetilde{\Delta\rho}_{l,m,n}(r',\theta',\varphi')$ indicates the maximum amplitude of the perturbation. In the cosine term, $\omega_{l,m,n}$ is the mode frequency and $\phi_{l,m,n}$ accounts for the oscillation phase. The first factor is:

$$\widetilde{\Delta\rho}_{l,m,n}(r',\theta',\varphi') = \left(\frac{\partial\rho}{\partial r'}\right)\Big|_{r'} \left[A_{l,m,n}\ f_{l,m,n}(r')\ Y_{l,m}(\theta',\varphi')\right] \tag{2.17}$$

In Equation (2.17), $\left(\frac{\partial\rho}{\partial r'}\right)\Big|_{r'}$ is the density gradient at a given internal radius r', $f_{l,m,n}(r')$ is the radial eigenfunction associated with the acoustic mode of degree l, azimuthal order m, and radial order n, whereas $A_{l,m,n}$ is the displacement of the upper troposphere.

By construction, the proposed formulation automatically satisfies the relation given in Eq. (2.15) for every admissible value of l, m, and n. On the other hand, the condition of mass conservation (Eq. 2.14), is not met when $l = 0$. This is because the proposed formulation does not account for the expansion and contraction of Jupiter's shape. In addition, a density perturbation of $l = 0$ (and arbitrary order n) does not affect external gravity, because the external gravitational potential is invariant to spherically symmetric variations of the internal density distribution. Furthermore, the relation given in Eq. (2.17) should not be applied to the dipole $l = 1$ terms as a perturbation associated to a dipole potential would produce a displacement of the center of mass of the planet, which would violate conservation of momentum. Thus, Eq. (2.17) only applies to modes with $l \geq 2$ and arbitrary order m and n.

The above formulation allows the computation of the dynamic contribution to the gravitational potential of gaseous planets, such as Jupiter or Saturn. The spherical harmonic coefficients of the gravity field expansion given in Eq. (2.11) now include the dynamic part due to the acoustic modes:

$$U_{l,m} = U_{l,m}^{STATIC} + \sum_{n\geq 0} \widetilde{U}_{l,m,n}\ \cos(\omega_{l,m,n}t + \phi_{l,m,n}) \tag{2.18}$$

The dynamic spherical harmonic coefficients (identified by an upper tilde) are:

$$\widetilde{U}_{l,m,n} = \frac{\int_V r'^l\ Y_{l,m}(\theta',\varphi')\ \widetilde{\Delta\rho}_{l,m,n}(P')\,dV}{(2l+1)\ M\ R^l} \tag{2.19}$$

Eq. (2.19) allows the computation of acoustic perturbations to the gravity field coefficients where the integral can be computed numerically in spherical coordinates. Spherical harmonic functions are well defined in the literature, and the density perturbation at a given point P′ is given by Eq. (2.17). The amplitude of the coefficients depends only

on the free parameters $A_{l,m,n}$, i.e., the surface displacement for the different modes. The gravitational potential, including the perturbation from Jupiter modes, is given by:

$$U(r,\theta,\varphi) = -\frac{GM}{r}\left\{1 + \sum_{l\geq 2}\sum_{-l\leq m\leq l}\left[\left(\frac{R}{r}\right)^{l} U_{l,m}\, Y_{l,m}(\theta,\varphi)\right] + \right. \\ \left. + \sum_{l\geq 2}\sum_{-l\leq m\leq l}\sum_{n\geq 0}\left[\left(\frac{R}{r}\right)^{l} \widetilde{U}_{l,m,n}\, Y_{l,m}(\theta,\varphi)\, \cos(\omega_{l,m,n}t + \phi_{l,m,n})\right]\right\} \tag{2.20}$$

The gravitational acceleration is obtained by computing the gradient of the gravitational potential, $a = -\nabla U$.

Since an accurate determination of the oscillation spectrum and mode amplitude of both planets is not yet accessible, in order to assess the contribution of acoustic oscillation on gravity fields, we develop a model for Jupiter, based on Gaulme et al., 2011 measurements. Their results suggest a mode peak amplitude, in terms of radial velocity, of roughly:

$$v \simeq 49\ cm/s \tag{2.21}$$

The frequency of maximum amplitude in the first window (800-2100 μHz) has been estimated as:

$$f \simeq 1213 \pm 50\ \mu Hz \tag{2.22}$$

These results are in broad agreement with the theoretical values (Vorontsov, Zharkov, and Lubimov, 1976; Bercovici and Schubert, 1987; Mosser, 1995) and previous observations (Mosser, Maillard, and Mékarnia, 2000). However the mechanism responsible for exciting these waves at these high amplitudes remains unknown (e.g., Gaulme et al., 2015).

Fuller, 2014 estimates that the mode amplitudes detected in Saturn by Hedman and Nicholson, 2013 are approximately 1000 times smaller than those found by Gaulme et al., 2011. This difference is in line with what has been observed on the Sun, where the amplitudes of low frequency modes are generally much smaller than the peak amplitude at higher frequency modes (Goldreich, Murray, and Kumar, 1994).

We would like to stress that Jupiter's detected modes are essentially p-modes (with radial order $n \sim 4-11$ and a low degree $l \sim 1$), whereas for Saturn, only f-modes ($n = 0$) have been observed. The main difference between the two is essentially the associated frequency: f-modes have a lower frequency than p-modes. For the Sun, the ratio between the observed mean velocity associated with p-modes and the observed mean velocity associated with f-modes (equal degree) is about 2 orders of magnitude [J. Jackiewicz,

personal communication]. Thus, we may also expect p-mode velocities to be larger than f-modes for Jupiter and Saturn.

Unfortunately, Gaulme et al., 2011 were not able to identify the degree and order of the spherical harmonics expansion of Jupiter's modes due to the high correlation between the projection of spherical harmonics into 2-dimensions, mainly produced by the resizing of the sensitivity area to 75% of the Jovian diameter. For this reason, a number of assumptions have been made for simplification purposes:

1. We suppose that the radial velocity associated with each mode depends only on its oscillation frequency, and not directly by its degree or radial order. This is in agreement with the observation of solar p-modes [J. Jackiewicz, personal communication];

2. While the excitation mechanisms do not show a preference for zonal modes, Juno is sensitive mostly to a zonal field. We therefore focus on the effects of those components of acoustic oscillations;

3. We assume a Gaussian profile for the radial velocity to frequency mapping function, plus a constant radial velocity, independent of mode characteristics.

With these assumptions, each mode's amplitude depends only on its frequency, and the mapping function is given by:

$$v(f) = v_{bias} + (v_{max} - v_{bias}) \exp\left[-\frac{1}{2}\left(\frac{f - f_{max}}{\sigma_f}\right)^2\right] \tag{2.23}$$

The velocity-to-frequency profile is constructed to match the observed peak frequency (1210 μHz) and the maximum observed radial velocity (50 cm/s). The parameter σ_f is the standard deviation in frequency, which is related to the Gaussian distribution assumed for the radial velocity. The quantity v_{bias} is an additive constant value, independent of the mode's frequency. To compute the surface displacement, we divide each mode's mean radial velocity at the surface by its frequency:

$$A_{l,m,n}|_{r=R} = \frac{v(f_{l,m,n})}{2\pi f_{l,m,n}} \tag{2.24}$$

The surface displacement allows the computation of the perturbation on harmonic coefficients. However, because we have information only within the observed frequency range, the quantities v_{bias} and σ_f are unknown, with no direct indication of their putative value. We explore two different scenarios to account for the uncertainty in the velocity-to-frequency profile, identified as case *A* and case *B*.

Case *A* is a nominal case. The value for v_{bias} is selected to match (by order of magnitude) the observed ratio between the amplitudes of p-modes and the amplitudes of

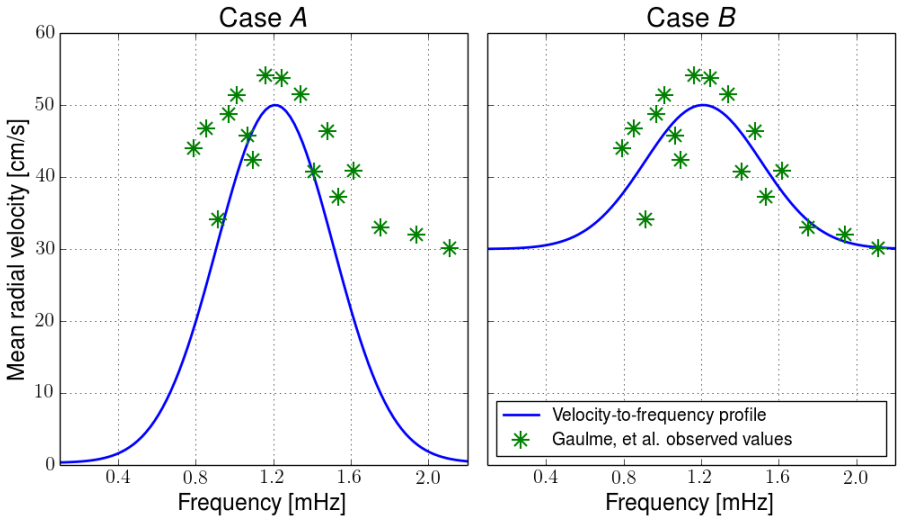

FIGURE 2.7: Mean radial velocity versus frequency for two selected cases, compared to the observed value reported by Gaulme et al., 2011. Note that the observations do not offer indications on the mode amplitude at low frequency. The two Gaussian profiles are attempts to extrapolate the mode amplitude outside the observed frequency range.

the f-modes in the Sun. This ratio represents the relative contribution to p-modes with respect to f-modes. For the Sun, the maximum ratio is about 100 (it changes with the degree considered). For Jupiter, we can achieve this by imposing $v_{bias} = 0.3$ cm/s, and selecting the other free parameter to match the trend in the observed values of the mean radial velocity around the maximum amplitude frequency, thus setting $\sigma_f = 300$ μHz. The fact that our function is a relatively poor approximation of the spectral amplitudes at high frequencies is inconsequential: as we will see afterwards, high order modes have much smaller effects on the global gravitational acceleration.

The second scenario, case *B*, depicts a very energetic Jupiter, with large f-mode amplitudes. The bias velocity is selected to match SYMPA's observed values for radial velocity at high frequencies (larger than the peak amplitude frequency), neglecting the contribution from the background noise. Thus, we set $v_{bias} = 30$ cm/s, and $\sigma_f = 300$ μHz. These values correspond to a profile that fits the observed values reported in Gaulme et al., 2011. Fig. 2.7 shows the velocity-to-frequency profiles for the two cases considered, with observed values reported for comparison. This unphysical case represents an upper limit set by the current observation.

In order to evaluate the contribution to Jupiter's gravity field coming from acoustic modes in the two cases, we compare the acoustic gravity harmonics with those expected from static gravity. A summary plot of the harmonic coefficients for the selected cases is reported in Figure 2.8, including modes with different degree and radial orders. For comparison, we also report the static contribution due to zonal winds for two different

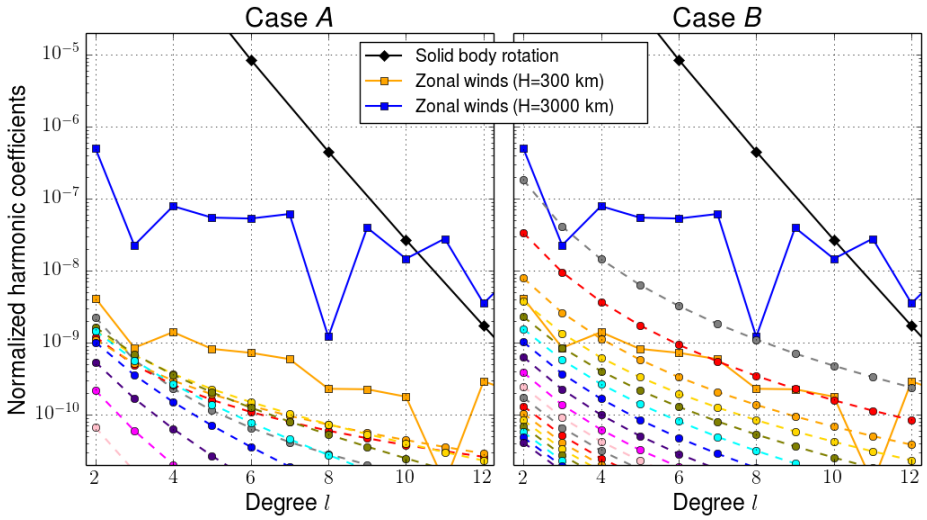

FIGURE 2.8: Perturbation to normalized harmonic coefficients of Jupiter's gravity field due to acoustic modes (colors), compared to the solid body rotation (black) and possible zonal wind contributions (blue and yellow, as labeled). The colors for the acoustic modes correspond to different radial orders, as in Fig. 1 (e.g., grey for $n = 0$, red for $n = 1$, orange for $n = 2$, yellow for $n = 3$, etc.).

penetration depths: $H = 300$ km (shallow winds), and $H = 3000$ km (deep winds).

Figure 2.8 shows that the expected dynamical contribution to gravity field harmonics tends to decrease for increasing radial order (for $n > 8$) and harmonic degree. Thus, low degree, low radial-order modes give the largest contribution to the gravity signal. Note that high order mode amplitudes ($n \simeq 5 - 7$) are essentially fixed by the maximum velocity given by the observations, whereas for the $n = 0$ f-modes (and generally for low n modes) we do not have direct indications, and the amplitude depends substantially on the parameter v_{bias}. In fact, in Fig. 2.7 we notice that in case *B* a large bias exists for all modes, while in case *A* the low frequency modes have a much smaller amplitude.

Note that in case *A*, the perturbing coefficients have about the same order of magnitude of shallow winds coefficients. In case *B*, gravitational perturbations due to acoustic modes are very significant, with magnitudes comparable to the contribution coming from density perturbations due to wind circulation in the deep zonal winds scenario.

The effects on Juno measurements have been assessed in Durante, Guillot, and Iess, 2017. In the strong mode scenario *B*, the signatures are mainly produced by the fundamental modes, which induce the largest perturbation (see Fig. 2.8). When the mode amplitude is large, a static field expansion is inadequate to absorb the effect of Jupiter's oscillation on Doppler data, so large signatures appear in the post-fit residuals. These signatures would be an indication of an inadequate dynamical model, and of the unreliability of the gravity solution. In this case a new data analysis approach would be required,

inescapably entailing the estimation of the mode amplitude, frequency, and phase. In case *A*, the post-fit residuals do not show a clear signature of acoustic modes, although some indiscernible evidence is present in a number of perijove passages, depending on whether the modes interact constructively. In that case, the low n modes have much lower amplitudes (a hundred times less than peak amplitude modes), producing only small perturbations on Jupiter's gravitational field. For the low f-mode amplitudes assumed within case *A*, it would be difficult to extract information on the modes from Juno Doppler data. On the other hand, the effect on the estimation of Jupiter's static field will be minimal (although biases at the level of a few sigma could still be possible).

Chapter 3

Data analysis

In this chapter, the general procedure of satellite orbit determination is presented along with details on the Doppler observables used for determining Jupiter and Saturn gravity fields. Then, Juno and Cassini data are analyzed, and the estimation results presented and discussed. The implications for the gas giants' interior structures are discussed in Chapter 4.

3.1 The orbit determination problem

The orbit determination (OD) process reconstructs the state of motion of a satellite, i.e., its trajectory. Specifically, the objective of the orbit determination of a satellite is to determine the dynamic system state vector, indicated by $X(t)$, which is a collection of parameters able to completely describe the state of motion of the probe. The OD procedure requires the knowledge of the dynamic state of a satellite and associated dynamical model. Integration of the differential equations governing the spacecraft motion, along with the initial condition, is used to allow the trajectory of the satellite to be computed at any future time.

However, it is impossible to know, with absolute accuracy, neither the state of a satellite nor the differential equations of the dynamic model as they will always be accompanied by some uncertainty. These errors affect the state of motion of the satellite, and the predicted trajectory may deviate considerably from the real trajectory after a given amount of time. For this reason, the satellite must be tracked from ground station to observe its motion over time.

Through observation of the satellite motion, it is possible to improve the dynamic model and the initial satellite state of motion in order to obtain a predicted trajectory as close as possible to the true trajectory during the time span of interest. However, it should be noted that the state is not directly observable, and that the observation data set usually consists of measurements of range, range-rate, elevation, or other physically observable quantities. Consequently, the dynamic model must be accompanied by the model of the

observations, which is a set of equations relating the observable to the dynamic state of the satellite.

In the general orbit determination problem, both the dynamics and the measurements involve nonlinear relationships which can generally be expressed by:

$$\dot{X} = F(X, t) \tag{3.1}$$

$$Y_i = G_i(X_i, t_i) + \epsilon_i \ , \ \ i = 1, 2, ... \, l \tag{3.2}$$

In these expressions, X is the so-called state vector, which collects the n parameters that will be estimated; the l vectors Y_i are each a set of p observations that will be used to obtain an estimation for the state vector, and the associate vector ϵ_i which contains the observation errors. Generally, the relation $m = p \cdot l \gg n$ is satisfied; the minimum observables m must be greater than the unknown parameters n, otherwise the procedure that follows cannot be applied.

Since the general expression in the case of orbital dynamics is highly non linear, a linearization procedure has been developed. If a reasonable reference trajectory is available, i.e., the deviation between the true trajectory and the reference trajectory is sufficiently small, the trajectory for the actual motion can be expanded in a Taylor's series about the reference trajectory at each point in time. If this expansion is truncated to first order terms, the state deviation from the reference trajectory is described by a set of linear differential equations, with time-dependent coefficients. By a similar expansion procedure, the observation deviation is in a linear relation with the state deviation. With the introduction of the deviations from a reference solution, the nonlinear orbit determination problem can be completely replaced by an iterative linear orbit determination problem. Accordingly, we introduce the state deviation and the observation deviation vectors:

$$x = X - X^* \ , \ \ y = Y - Y^* \tag{3.3}$$

Here, X^* is the reference trajectory, whereas Y^* are the observables computed on the reference trajectory. Deviation vectors are denoted by lowercase x, y.

Expanding Equation (3.1) about the starred trajectory and limiting the Taylor's series to first order, leads to:

$$\dot{X} = F(X^*, t) + \left. \frac{\partial F}{\partial X} \right|_{X^*} (X - X^*) + o(X - X^*)^2 \tag{3.4}$$

Higher order terms $o(X - X^*)^2$ are neglected. With some computation, the equation becomes:

$$\dot{x} = \left.\frac{\partial F}{\partial X}\right|_{X^*} x = A(t)\, x \tag{3.5}$$

The result (3.5) is a set of linear differential equations. The very same procedure can be applied to Equation (3.2), which produces:

$$y_i = \left.\frac{\partial G_i}{\partial X}\right|_{X^*} x_i + \epsilon_i = \tilde{H}_i\, x_i + \epsilon_i \tag{3.6}$$

The general solution for Equation (3.5) can be easily expressed thanks to the state transition matrix:

$$x(t) = \Phi(t_0, t)\, x_0 \tag{3.7}$$

Where x_0 is the state at a given epoch. In fact, the state transition matrix can be used to express all observations in terms of the state at a given epoch in order to reduce the number of unknowns to n, the same dimension of a the state vector. Each observation can be written as:

$$y_i = \tilde{H}_i\, \Phi(t_i, t_0)\, x_0 + \epsilon_i \tag{3.8}$$

Writing this equation for each observation leads to m equations with n unknowns of the state components plus the m unknown errors ϵ_i; therefore the total unknowns are $n + m$ and the system cannot be directly resolved. The least squares method overcomes this difficulty, providing us with conditions on the m observation errors that allow solving for the n state variables.

We can introduce the matrix H, which collects the $\tilde{H}_i\Phi(t_i, t_0)$ terms, and the vector ϵ, which collects the observation errors:

$$H = \begin{bmatrix} \tilde{H}_1\Phi(t_1, t_0) \\ \vdots \\ \tilde{H}_l\Phi(t_l, t_0) \end{bmatrix} \quad , \quad \epsilon = \begin{bmatrix} \epsilon_1 \\ \vdots \\ \epsilon_l \end{bmatrix} \tag{3.9}$$

The observations in Equation (3.8) can be collected and expressed as:

$$y = H\, x_0 + \epsilon \tag{3.10}$$

Where y and ϵ are m-by-1 vectors, x_0 is an n-by-1 vector, and H is an m-by-n mapping matrix. The essential condition to resolve this linear system is $m > n$.

The least squares criterion was first proposed by Gauss in 1809. It is able to select the estimate of x_0 that minimizes the sum of the squares of the calculated observation

residuals. That is, $\hat{x}_0$ is selected to minimize the following performance index, or cost function:

$$J = \frac{1}{2}\epsilon^T \epsilon \tag{3.11}$$

Note that it is a quadratic function of x. The sum of the squares of the calculated observation errors is a logical choice for the performance index because, whether the observation error is positive or negative, its square will be positive as well as the performance index, which can vanish only if each of the observation errors is identically zero.

Minimization of the cost function with respect to the state $\hat{x}_0$ leads to the best estimate of the state:

$$\hat{x}_0 = (H^T H)^{-1} H^T y \tag{3.12}$$

which solves the problem.

The least square solution can be improved by including a weight matrix for the observations and a priori information on the reference state. The weight matrix W is introduced to assign different weights to the observables. Also, if the weight matrix is selected as the inverse of the observation noise covariance matrix, $R = E[\epsilon\epsilon^T]$, the unbiased estimate $\hat{x}_0$ has the minimum variance. In addition, a priori information on the state $\overline{x}_0$ may be available (with associated weighting matrix $\overline{W}$) as previous estimate of the spacecraft position or gravity field coefficients, and can be included in the least square formulation.

The cost function is modified:

$$J = \frac{1}{2}\epsilon^T W \epsilon + \frac{1}{2}(\overline{x}_0 - x_0)^T \bar{W}(\overline{x}_0 - x_0) \tag{3.13}$$

And the least square solution is given by:

$$\hat{x}_0 = (H^T W H + \overline{W})^{-1}(H^T W y + \overline{W}\overline{x}_0) \tag{3.14}$$

We can define the covariance matrix as:

$$P_0 = (H^T W H + \overline{W})^{-1} \tag{3.15}$$

The covariance matrix is symmetric and positive defined, and it is computed by inverting the information matrix, $H^T W H + \overline{W}$, which must be positive defined. The matrix P_0 is related to the accuracy of the state estimate, $\hat{x}_0$. In general, the larger is the magnitude of the element, the less accurate is the corresponding estimate.

A quantity closely related to the covariance matrix is the correlation matrix, defined by:

$$C_0 = diag(P_0)^{-1/2}\ P_0\ diag(P_0)^{-1/2} \tag{3.16}$$

Where $diag(P_0)$ is the matrix composed only by the diagonal elements of the covariance matrix P_0. From the definition, it follows that the absolute value of the correlation matrix elements varies between 0 and 1 and in particular, the diagonal will be formed only by ones. In addition, the higher is the value of an element, the higher is the correlation between the two parameters, i.e., there is an aliasing of the two effects. In this case, the least-square filter can not properly distinguish between the two parameters leading to greater formal uncertainties.

To conclude, orbit determination is an iterative process; thus, after the first estimate $\bar{x}_0$, a new process should be carried out, starting from the solution computed in the previous step. The process stops when convergence is reached, i.e., when the actual computed trajectory is sufficiently close to the true trajectory, and the observations residuals do not greatly change with additional iterations.

3.1.1 The multi-arc approach

In the previous paragraphs we discussed the process of orbit determination and we have seen that, thanks to the state transition matrix it is possible to express all observations in terms of the state at a given epoch, usually the initial date of the observations. However, this is not the optimal solution in the case of long observation periods, or more generally, when the uncertainty on the parameters which define the dynamical system is such that it produces a considerable deviation with respect to the trajectory actually followed by the satellite. In fact, one of the main assumptions made is that the dynamical model used is deterministic. Small errors in the model may cause effects on the satellite's state of motion, which in time may significantly affect the results of the orbit determination process.

In the multi-arc approach, the entire time span of the observations is decomposed in shorter intervals, each with its own set of observables, and is referred to as an observed arc, or just an arc of trajectory. This subdivision is extremely useful if you cannot exactly follow the evolution of the dynamic state of the probe between two distinct intervals of observation or if each arc of trajectory is not dynamically coherent with the others. In fact, in the model first developed, the trajectory of the satellite was consistent throughout the whole selected interval of time. For example, in the case of Juno, at least one orbital trim maneuver is planned, which inevitably destroys the coherence between two successive orbits, mainly because the high uncertainties coming from the maneuver. In this case, the total time span of the mission will be divided in smaller arcs, where observables for radio-science experiments are provided, without any orbital maneuvers.

As part of the multi-arc approach, the distinction is made between global fit parameters and local fit parameters. Global parameters are those parameters that are estimated using all available observables and whose value affects equally all arcs. Therefore, they are parameters that do not change between different arcs and thus are treated as global. Generally, this category contains the coefficients of the spherical harmonics expansion of the gravitational potential. On the other hand, the local parameters are those parameters that affect the single arc, and that are in no way involved in the description of other arcs. Therefore they may be parameters not constant over time. Clear examples are the position and the initial velocity of the satellite at the beginning of each arc; these parameters are inherently local for each arc.

From a practical point of view, the vector of parameters to be estimated will contain N-times the local parameters of each of the N arcs (note that each arc may have different set of local parameters), and only one instance of the global parameters:

$$x = \begin{bmatrix} x^{l,1} \\ x^{l,2} \\ \vdots \\ x^{l,N} \\ x^{g} \end{bmatrix} \tag{3.17}$$

The analytical formulation is formally the same as that presented in the previous paragraph, except for this distinction between the various parameters. The complete measurement model for the observation over arcs is exactly the same:

$$y = H\, x_0 + \epsilon \tag{3.18}$$

This is written as:

$$\begin{bmatrix} y^1 \\ y^2 \\ \vdots \\ y^N \end{bmatrix} = \begin{bmatrix} H^{l,1} & 0 & \cdots & 0 & H^{g,1} \\ 0 & H^{l,1} & \cdots & 0 & H^{g,2} \\ \vdots & \vdots & \ddots & \vdots & \vdots \\ 0 & 0 & \cdots & H^{l,N} & H^{g,N} \end{bmatrix} \begin{bmatrix} x^{l,1} \\ x^{l,2} \\ \vdots \\ x^{l,N} \\ x^{g} \end{bmatrix} + \begin{bmatrix} \epsilon^1 \\ \epsilon^2 \\ \vdots \\ \epsilon^N \end{bmatrix} \tag{3.19}$$

The solution to the least square problem leads to the same result for both the best estimate of the state vector and its associated covariance. Only the mapping matrix H is constructed in a different way, as reported above.

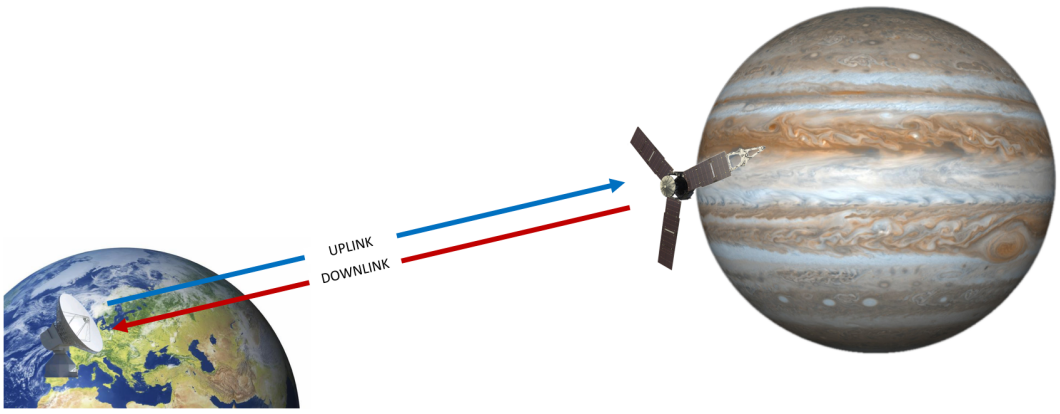

FIGURE 3.1: Schematic representation of a two-way Doppler tracking configuration.

3.2 Doppler observables

The observable quantities generally used for spacecraft navigation and scientific investigations are:

- Range observables
- Range-rate (Doppler) observables
- Angular observables

For deep space navigation and radio science experiments, Doppler observables are the main source of information for a spacecraft orbiting a planet thanks to their exquisite accuracy. The Doppler measurements are made by means of a radio tracking system, which measures the properties of a radio signal that travels from a transmitter to a receiver.

The classical configuration, used during scientific operation as well, is the two-way radio link. The two-way range-rate observable comes from a measurement of the Doppler shift of a signal. The signal is transmitted from the ground station at a frequency f_T at time t_1 and is received at time t_2 by the spacecraft with a certain Doppler shift caused by the relative motion between the satellite and the ground antenna. The on board transponder (DST or KaTS) transmits the signal back, coherently in phase, with a frequency which is a multiple (turn-around ratio, α) of the one received so as not to interfere with the incoming signal. In the end, the signal is received at t_3 at the some ground station with a frequency f_R. See Figure 3.1 for a schematic representation. In a three-way configuration, the receiving antenna is different from the transmitting antenna.

The downlink signal can be acquired with various kind of receivers, leading to different data sets:

- Closed-loop data
- Open-loop data

The closed-loop receiver is a PLL (Phase Lock Loop) which locks onto the incoming signal, providing the received frequency. The open-loop receiver directly records the I and Q samples of the incoming signal, and further processing is required to extract the sky frequencies.

The closed-loop receiver directly produce in real time the received frequency as output, not allowing a further processing of the data acquired. The closed-loop data are the standard data, used also from the navigation team for the determination of the spacecraft trajectory. Instead, the open-loop reciever directly records the electrical signal recieved by the antenna (the I and Q samples), and a dedicated software PLL is devoted to extract the received frequencies of the signal. Open-loop data can be processed via software to obtain the best data set possible, and for that reason are generally used for radio science investigation, where the data quality is very important. In addition, this data are acquired also as a backup option, in the case of a failure of the closed-loop reciever, or when the signal-to-noise ratio is low and the standard receiver cannot lock onto the incoming signal, not producing an output dataset. Processing of open-loop data enables the recovering of the received signal even if the SNR is low (for example during Saturn's ring occulation).

The Doppler shift cannot be measured instantaneously, but by counting the accumulated cycles of zero-crossing over a time span T_c, called count time, or integration time. For this reason, the observable computed is called the Integrated Doppler shift. The number of cycles that the Doppler frequency accumulates over a time interval can be calculated by:

$$N = \int_{t-T_c/2}^{t+T_c/2} (f_R - f_{ref})dt \tag{3.20}$$

The observed observable is compared with the OD's computed observable, which, for the two-way Doppler, is given by:

$$C = -\frac{\alpha}{T_c} \int_{t_{1,beg}}^{t_{1,end}} f_t(t_1)dt_1 \tag{3.21}$$

where α is the spacecraft turn around ratio for a specified band, $t_{1,beg}$ and $t_{1,end}$ are the times at which the ground antenna was transmitting, corresponding to the times at which the signal is received at ground and integrated trough the count time $[t-T_c, t+T_c]$. The quantity f_t is the transmitted frequency.

3.2.1 Noise sources

Radiometric measurements are affected by several sources of noise. The noise level found in the Doppler data is directly reflected in estimation accuracies, as the covariance matrix of the estimation process scales with the weights assigned to the observables, i.e., with the data quality.

The main sources of noise in radiometric observables can be categorized as:

1. Instrumental noise
2. Propagation noise
3. Systematic errors

The instrumental noise consists of random errors introduced by the ground antenna instrumentation and the on-board systems (DST or KaTS).

The propagation noise is caused by the signal propagating in a medium whose refractive index is not equal to one, nor sufficiently stable with time. Random refractive index fluctuations change the direction and velocity of the propagating wave, thus introducing a phase instability (Asmar et al., 2005), which compromises the quality of the Doppler data.

The two main sources of noise related to propagation effects are due to Earth's troposphere and dispersive media (like interplanetary plasma or Earth's ionosphere).

Earth's troposphere has two main components which affect the carrier's stability: A dry component (dry air) and a wet component (water vapor). The dry part induces the largest delay on the signal (90% of the total), but the wet troposphere is the most unstable. An Advanced Media Calibration (AMC) system is able to measure the wet component by about 90% (see Subsection 3.2.2), enhancing the Doppler data quality.

Dispersive noise can be calibrated using a dedicated radio tracking configuration (see Subsection 3.2.3).

Systematic errors occur due to residual orbital signatures (i.e., the dynamical model does not account for a particular effect) or calibration biases.

A measurement of a radio link stability is given by the Allan deviation (Barnes et al., 1971), which is a time domain measure of fractional frequency fluctuation as a function of averaging time, τ. The observables are represented by a time series $y(t)$ of fractional Doppler fluctuations, that is the change in frequency between the received and reference signal, divided by the nominal frequency of the Doppler link:

$$y(t) = \frac{\Delta f(t)}{f_0} \tag{3.22}$$

The Allan variance (Allan deviation squared) is computed as:

$$\sigma_y^2(t) = \frac{1}{2}\left\langle \left| \overline{y(t)} - \overline{y(t+\tau)} \right| \right\rangle \tag{3.23}$$

with:

$$\overline{y(t)} = \int_{t'}^{t'+t} y(t')dt' \tag{3.24}$$

During the Cassini cruise phase, calibrated Doppler data achieved Allan deviations of the order of 10^{-15} for integration times of 1000s (Asmar et al., 2005). Data analyzed during Juno's cruise show similar accuracies.

3.2.2 Tropospheric calibration

Earth's troposphere is a portion of the atmosphere located from sea level to an altitude of approximately 42 km. It is composed mostly by neutral gas and the fluctuations of the refractive index are mostly induced by fluctuations of temperature, pressure, or partial pressure of water vapor. At microwave frequencies, the troposphere acts as a non-dispersive medium, thus the delay suffered by the radio signal in unaffected by the frequency of the signal itself.

NASA has developed a continuous troposphere calibration system, based on GPS observations made at each DSN site with an hourly and daily cadence, to calibrate Doppler data acquired by the DSN antennas. The system, known as Tracking System Analysis Calibration (TSAC), creates calibrations of the Zenith Total Delay (ZTD) over time, which are then scaled to the elevation angle of the spacecraft with the Niell mapping function (Niell, 1996). The TSAC system can produce observations of the ZTD with an RMS lower than 1 cm (daily version).

Recently, NASA has developed a new system, named Advanced Water Vapor Radiometer (AWVR) (see Tanner, 1998; Naudet et al., 2000), devoted to accurately characterize fluctuations in the Earth's water vapor content at time scales larger than 20 s. The radiometer measures the brightness temperature at 22.2, 23.8, and 31.4 GHz, with a long term stability, along the line of sight (as close as possible to the pointing direction of the ground antenna). The path delay along the line of sight is then estimated by measuring the strength of the 22.2 GHz spectral line of water, which is related to the integrated columnar density of water vapor. The additional frequencies are used to increase the performance of the system, accounting for minor effects (such as the presence of clouds).

The system has been used during the Cassini GWE (Gravitational Wave Experiment) in 2002, and is currently scheduled to be used for all Juno perijove passes at DSS 25.

Date	SEP angle	Adev w/ TSAC	Adev w/ AMC	Improvement
25 Feb. 2015	174 deg	$5.76 \cdot 10^{-15}$	$3.54 \cdot 10^{-15}$	- 38.6%
5 Mar. 2015	166 deg	$6.09 \cdot 10^{-15}$	$4.30 \cdot 10^{-15}$	- 29.4%
12 Mar. 2015	158 deg	$1.03 \cdot 10^{-14}$	$5.85 \cdot 10^{-15}$	- 43.0%
13 Apr. 2015	122 deg	$3.25 \cdot 10^{-14}$	$7.97 \cdot 10^{-15}$	- 75.4%
4 May 2015	102 deg	$1.01 \cdot 10^{-14}$	$8.38 \cdot 10^{-15}$	- 17.4%
11 Sep. 2015	3.7 deg	$3.33 \cdot 10^{-14}$	$2.93 \cdot 10^{-14}$	- 12.2%
25 Sep. 2015	14 deg	$2.87 \cdot 10^{-14}$	$1.24 \cdot 10^{-14}$	- 56.9%
24 Feb. 2016	159 deg	$6.93 \cdot 10^{-15}$	$6.83 \cdot 10^{-15}$	- 1.4%
21 Mar. 2016	171 deg	$7.40 \cdot 10^{-15}$	$3.73 \cdot 0^{-15}$	- 49.6%
18 Apr. 2016	139 deg	$1.45 \cdot 10^{-14}$	$1.33 \cdot 10^{-14}$	- 8.6%

TABLE 3.1: Comparison of Juno cruise data Allan deviation at 1000 s with and without AWVR calibration.

Calibration comparison during the Juno cruise

During cruise, Juno collected Ka-band data for testing purposes on a few occasions, along with AWVR data to be used for calibration. Ten tracking passes were analyzed between February 2015 and April 2016, prior Juno's Jupiter Orbit Insertion (JOI).

Table 3.1 show the results for the different tracking passes, comparing the TSAC calibration (widely used for their simplicity) and the AMC.

There was an improvement from -1.4% on 24 Feb. 2016, where the data quality was already good with TSAC calibration, to -75% on 13 Apr. 2015, where the tropospheric noise was clearly dominant, thus the AMC lowered the Doppler noise to $8\ 10^{-15}$.

The minimum Allan deviation is about $3.5\ 10^{-15}$ at 1000 s during Solar opposition (SEP angle close to 180 degrees).

3.2.3 Plasma calibration

A phase-coherent carrier signal in a two-way radio link is subject to a phase scintillation caused by the refractive index of the interplanetary medium being crossed during the uplink and downlink leg. An ionized plasma has, at first order, a refractive index which is inversely proportional to the frequency of the incoming signal.

Dispersive effects are the predominant noise source in Doppler error budget nowadays, as mentioned in Section 3.2.1. The use of a Ka/Ka radio link reduces the effect of dispersive noise by a factor of almost 16 over the widely used X/X link (for spacecraft navigation), as it is inversely proportional to the frequency squared.

A complete calibration of dispersive effects on radio tracking system is enabled by a triple link, as done in Cassini prior to the KaT failure, where an X/X, an X/Ka, and a Ka/Ka radio link was established simultaneously. For such a radio system, the set of

equations which describes the fractional frequency shift y is (Bertotti, Comoretto, and Iess, 1993; Mariotti and Tortora, 2013):

$$y_{xx} = y_{nd} + y_{\uparrow} + \frac{y_{\downarrow}}{\alpha_{xx}^2} \tag{3.25}$$

$$y_{xk} = y_{nd} + y_{\uparrow} + \frac{y_{\downarrow}}{\alpha_{xk}^2} \tag{3.26}$$

$$y_{kk} = y_{nd} + \frac{y_{\uparrow}}{\beta^2} + \frac{y_{\downarrow}}{\beta^2\ \alpha_{kk}^2} \tag{3.27}$$

The subscript nd stands for non-dispersive (i.e., the contribution unaffected by propagation within a media), the arrows indicates the uplink and downlink legs, $\alpha_{*/*}$ are the turn-around ratios for specified bands (α_{kk} is the turn-around ratio for the Ka/Ka link). β is the ratio between uplink frequency of the X-band, and that of the Ka-band:

$$\beta = \frac{f_{\uparrow,k}}{f_{\uparrow,x}} \tag{3.28}$$

For a triple link, the observables can be easily combined to compute the plasma-free observable y_{nd}, since the system of three equations has exactly three unknowns. However, neither Juno nor Cassini have access to this calibration. Juno's radio system was not designed to support the triple link, and Cassini's KaT (for Ka/Ka link) failed during cruise.

An alternative calibration scheme can be applied. For an X/X along with an X/Ka link, the downlink contribution $y_{\downarrow}$ can be extracted, by simply subtracting the first two equations (Eq. 3.26 minus Eq. 3.25):

$$y_{\downarrow} = \frac{y_{xx} - y_{xk}}{\alpha_{xx}^{-2} - \alpha_{xk}^{-2}} \tag{3.29}$$

This calibration scheme is, however, not very effective in reducing the Doppler noise, since the uplink contribution, $y_{\uparrow}$ is unaffected, whereas the downlink noise was already greatly reduced in X/Ka link due to the higher frequency of the Ka band signal.

A very useful calibration scheme can be applied for X/X and Ka/Ka links. This incomplete calibration scheme allows to reduce up to 75% the dispersive noise, when compared to the uncalibrated Ka/Ka link. The calibrated observable y_* can be obtained by removing a contribution from the uplink, downlink or a combination of both. Mariotti and Tortora, 2013 show that the calibrated observable with minimum variance for y_* can be obtained through a statistical optimization, which leads to:

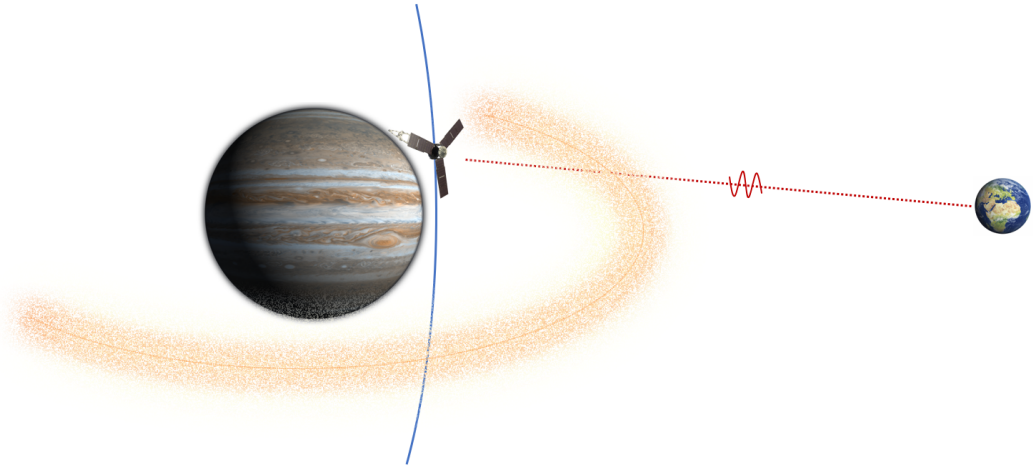

FIGURE 3.2: Schematic representation of Juno geometry with respect to the Io Torus. The line of sight crosses the torus when Juno moves along its polar orbit.

$$y_* = -\frac{\beta^{-2}\,(1+\alpha_{kk}^{-2}\,\alpha_{xx}^{-2}) - (1+\alpha_{xx}^{-4})}{D}\; y_{kk} + \\ +\frac{\beta^{-4}\,(1+\alpha_{kk}^{-4}) - \beta^{-2}\,(1+\alpha_{kk}^{-2}\,\alpha_{xx}^{-2})}{D}\; y_{xx} \tag{3.30}$$

with the constant D defined by:

$$D = \beta^{-4}\,(1+\alpha_{kk}^{-4}) - 2\beta^{-2}\,(1+\alpha_{kk}^{-2}\,\alpha_{xx}^{-2}) + (1+\alpha_{xx}^{-4}) \tag{3.31}$$

Io Plasma Torus

A special case where plasma calibration has proved to be very useful is Juno, due to the characteristics of Jupiter's magnetosphere and the presence of the Io Plasma Torus (see Figure 3.2). A brief discussion on the radio occultation of the Io plasma Torus can be found in Phipps and Withers, 2017. They made simulations to assess the feasibility of Io Torus occultation experiments, showing that they are feasible.

Jupiter's moon Io has multiple volcanoes currently active on its surface. These erupt, spewing a gas of ionized particles with a velocity high enough to start orbiting Jupiter, and interacting with its strong magnetic field. This process results in a donut shaped plasma region surrounding Jupiter, i.e. the Io Plasma Torus. The plasma particles in the Torus are forced from Jupiter's magnetic field to co-rotate with the planet, with a period of 10h, faster than Io's orbital period. This means that the plasma is accelerated and overtakes Io itself.

The Io Plasma Torus is mainly composed of different ion species Bagenal et al., 1997; Nerney, Bagenal, and Steffl, 2017: S+, S2+, S3+, O+, and O2+, with 10% of protons. The plasma torus electron density has a peak at about the radial distance of Io with respect to Jupiter, and decreases with both radial distance and transverse distance from the centrifugal equator.

The Juno Deep Space Transponder radio system is complemented by a Ka-band system devised for the radio science investigation. The system was not designed to implement the multi frequency link (i.e., X/X, X/Ka, and Ka/Ka links established simultaneously), therefore the X/X link can be supported by either a X/Ka link or a Ka/Ka link.

During dedicated perijove passes, the on-board Ka-band frequency translator (KaT) locks into a Ka band uplink signal at 34 GHz and retransmits it coherently to ground at 32 GHz. This radio system configuration, used on December 2016 during the third and sixth perijove passes (PJ03 and PJ06) and planned for all gravity orbits, allows a 75% calibration of dispersive contributions in the Ka signal, such as the effect due to Io's plasma torus.

During PJ01, a direct measurement of downlink plasma contribution was possible by transmitting downlink signals at X and Ka band coherent with a common X-band uplink. For PJ03 and PJ06, the incomplete calibration scheme has been applied, and the dispersive contribution can be extracted.

The extracted dispersive fractional frequency shift y_d can then be integrated to compute the path delay over time:

$$\Delta l = \Delta l_0 + \int_{t_0}^{t} y_d \, c \, dt \tag{3.32}$$

The path delay at the beginning of the pass, Δl_0, is set to zero arbitrarily. The constant c is the speed of light. TEC profiles can be computed from the path delay profiles. At first order, it is given by:

$$\Delta l = -\kappa \frac{TEC}{f^2} \tag{3.33}$$

The constant $\kappa \simeq 40.3 \; m^3/s^2$, and frequency must be expressed in Hertz. The reference frequency used to compute the path delay and TEC profiles is the X-band downlink frequency.

The dispersive contributions (reference frequency: $f = 7.2 \; GHz$) and path delays (and TEC) extracted from PJ01 and gravity passes (with different calibration techniques) are reported in Figure 3.3

The PJ01 dispersive contribution caused by the Io torus, close to the pericenter, is pretty clear. The constant bias found, which translates to a linear trend in the recovered path delay, is compatible with the (uncalibrated) solar corona delay at PJ01 solar

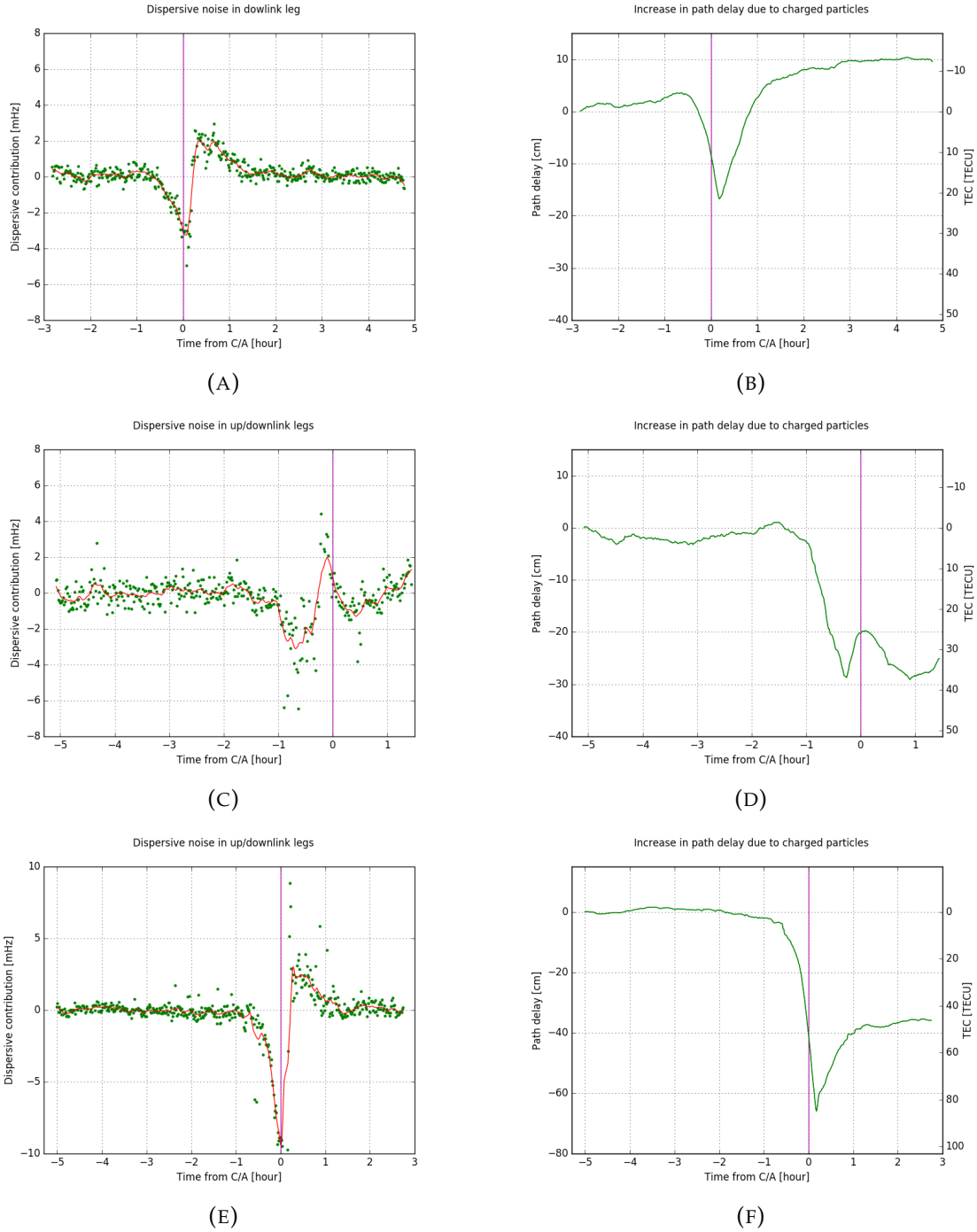

FIGURE 3.3: Dispersive contribution (panels A, C, and E) and path delay (panels B, D, and F) for PJ01, PJ03, and PJ06 data.

Perijoves	Scope	Data collected
PJ01	Generic science	X/X and X/Ka
PJ02	Safe Mode	X/X only
PJ03	Gravity science	X/X and Ka/Ka
PJ04	MWR measurements	X/X only
PJ05	MWR measurements	X/X only
PJ06	Gravity science	X/X and Ka/Ka
PJ07	MWR measurements	X/X only

TABLE 3.2: Summary of Juno perijoves and data acquired.

elongation angle. During PJ03 and PJ06, the contribution due to the Io Plasma Torus is still evident around pericenter (peaking at a different time with respect to C/A), but the asymmetry in the tracking pass prevents the complete signal of the torus from being seen.

Juno radio instrumentation is able to provide an accurate determination of dispersive contributions in radio observables collected for gravity science purposes. Although a complete calibration is not possible, the incomplete calibrations (X/X+X/Ka or X/X+Ka/Ka) can provide very interesting results for the Io Torus characterization.

In the past, Voyager, Galileo, and Cassini missions have contributed to the understanding of the Io Torus structure and composition (Nerney, Bagenal, and Steffl, 2017). Juno will provide accurate measurements of TEC profiles along the line-of-sight, across all future gravity orbits. In addition, the spacecraft will probe the Torus at different longitudes, potentially providing information about its longitudinal variability.

3.3 Juno data analysis

In this section, we report the analysis of Juno gravity data. Table 3.2 summarizes the perijove passes completed by Juno as of September 2017, with the scope and the type of Doppler data collected.

Two passes have been dedicated to the gravity field determination, PJ03 and PJ06. In both of them, X/X and Ka/Ka two-way Doppler data have been collected by NASA's DSS 25 for 8 hours, covering the closest approach. The Doppler data have been calibrated for both Earth's troposphere (see Subsection 3.2.2) and plasma scintillation and Io Torus (see Subsection 3.2.3).

3.3.1 Dynamical model and observables

Juno's dynamical model accounts for several effects, both gravitational and non-gravitational accelerations. It includes:

- Relativistic acceleration from Jupiter and the Galilean satellites

- Spherical harmonic expansion of Jupiter's gravity field (static and time-varying)
- Newtonian (point-mass) acceleration from all the other Solar System's planets
- Tides raised on Jupiter from the satellites
- Lense-Thirring relativistic acceleration caused by Jupiter's rotation
- Solar radiation pressure on Juno
- Jupiter's albedo and infrared emission acting on Juno

The list contains all the models whose acceleration on Juno is sufficiently large to produce a detectable signal in Juno Doppler data. The larger contribution obviously comes from Jupiter's gravity field. Solid tides are a major perturbation to Juno's motion, whereas Lense-Thirring and non-gravitational accelerations are orders or magnitude below the large Jupiter' central field acceleration, but near the threshold of detectability. For a detailed discussion of Juno's dynamical model, refer to Finocchiaro and Iess, 2010; Finocchiaro, 2013; Tommei et al., 2015.

The Doppler observables formulation includes the Shapiro effect caused by celestial bodies (Jupiter causes the greatest effect) on the propagation of radio waves. In addition, the effect of Jupiter's large oblateness (J_2) is taken into account when computing the Doppler observables. In fact, Einstein's general relativity theory explains how a propagating radio wave is perturbed when traveling in a gravitational field. Juno's orbital geometry and the radio science experiment are not sufficiently sensitive to test Einstein's theory as done during Cassini cruise phase, when the post-Newtonian parameter γ was accurately measured (Bertotti, Iess, and Tortora, 2003).

Since Juno is a spinning spacecraft, an additional effect must be included when analyzing Juno's Doppler data. The transponder on-board the spacecraft measures a frequency of the incoming signal which is shifted since it is in a rotating reference frame. In addition, when the signal is retransmitted back to the Earth, it experiences an additional Doppler shift. The Marini effect (Marini, 1972) is then given simply by:

$$\Delta f_{Marini} = (\pm 1 \pm \alpha)\, f_{spin} \tag{3.34}$$

The signs depends on the polarizations of the transmitted signals (either left of right polarized), which are mission dependent. The frequency f_{spin} is the projection along the line of sight of the spin frequency. The equations are simplified since Juno is almost aligned with the Earth during gravity perijoves, and the antenna boresight is approximately along the rotation axis.

3.3.2 Multi-arc setup

The Doppler data acquired during PJ03 and PJ06, are first analyzed independently, and then combined in a multi-arc least square information filter, solving for:

- Spacecraft state at given epoch
- Jupiter's gravitational parameter μ_{jup}
- Jupiter's zonal spherical harmonics (up to degree 24)
- Jupiter's tesseral field to degree 2
- Jupiter tidal response (Love number k_{22})
- Jupiter's spin axis inertial direction and rate
- Jupiter's ephemeris (linear correction to the orbit)

The very same set of estimated parameters is able to fit both the single arc and the multi-arc solution. In the latter, the components of the spacecraft's state are estimated as local parameters, referred to approximately 6 hours prior to the closest approach. The a priori value for position and velocity are, respectively, 100 km and 1 m/s, in order not to constrain the final solution.

Jupiter's gravitational parameter and its uncertainty are set to the values estimated from the motion of Galileian satellites (JUP310 solution by Jacobson, 2013). Juno's orbital geometry is not appropriate to produce a better estimate Jupiter's gravitational parameter with a greater accuracy. IFor that reason, it will be constrained to the a priori value estimated with observations of the satellite's motion.

Concerning the gravity field of the gas giant, the minimum set of spherical harmonic coefficients able to fit the Doppler data to the noise level is given by zonal harmonics up to degree 24, and a tesseral field of degree 2 (full quadrupole coefficients). As a priori uncertainty, a value of 10^{-5} for all the harmonics have been selected, which does not constrain the solution.

Jupiter's Love number k_{22} has been estimated, whereas the higher order Love numbers are currently set to the values computed by Wahl, Hubbard, and Militzer, 2016 on a preliminary Jupiter interior model. The non-estimated Love numbers are considered at 20% of their values.

Concerning the spin axis direction, its right ascension and declination are estimated at a reference epoch (J2000). The rates (linear terms) are estimated, but their determination is not accurate, due to the limited number of passes.

Jupiter's ephemeris is updated since the knowledge of Jupiter's position prior to Juno's data was fairly inaccurate. As the uplink frequency profile has a steep dynamic, an

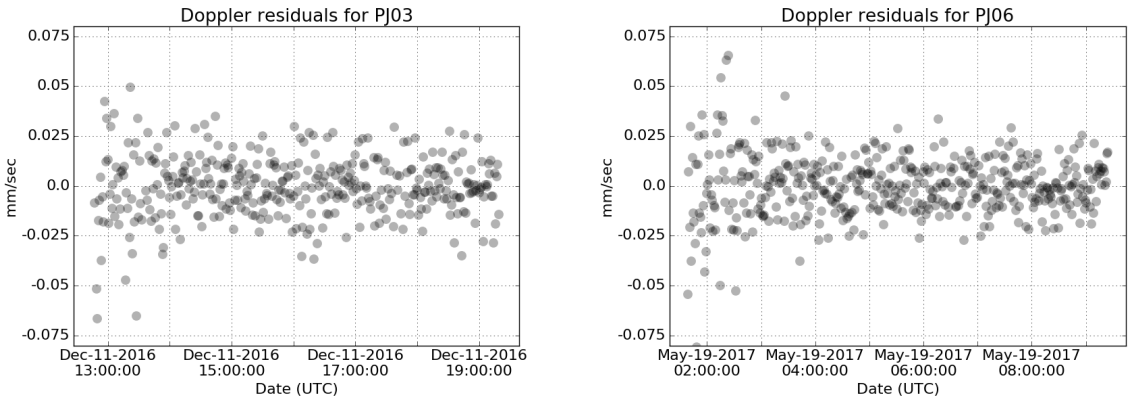

(A) (B)

FIGURE 3.4: Doppler residuals for PJ03 (panel A) and PJ06 (panel B).

error in Jupiter's ephemeris would have an effect on Juno's extremely accurate Doppler data, and this effect must be taken into account.

Other parameters, such as Juno's solar radiation pressure scale factor, Jupiter's thermal albedo and emissivity scale factors, and the satellite's gravitational parameters, are included in the multi-arc filter as consider parameters. The satellite's μ_{sat} are considered with an uncertainty given by the Jovian ephemeris, whereas the scale factors are considered with a 20% uncertainty.

3.3.3 Results

The Doppler residuals at an integration time of 60 s, converted in mm/s for convenience, are reported in Figure 3.4. The data quality is very good: RMS of $0.013\ mm/s$ for both PJ03 and PJ06. In addition, no signature near the closest approach is evident, meaning that the data have been fitted to the noise level.

The multi-arc solution can be found in Table 3.3. The estimated values for the gravity field coefficients are reported along with the formal uncertainties (3-sigma level).

Gravity harmonics to degree 10 (included) are well resolved, with the central value higher than the 3-sigma uncertainty. On the contrary, higher order harmonics are unresolved, but the filter requires them to fit the Doppler data satisfactorily to the noise level close to the perijoves. The formal uncertainties on the low-degree even harmonics previously published (JUP310 solution by Jacobson, 2013) have been dramatically improved. The uncertainty on J_2 is decreased by about two order of magnitude, whereas for J_4 and J_6 the improvement is of three order of magnitude. This exquisite accuracy enables a good inference of Jupiter's internal structure. The first determination of the low-degree odd harmonics enables to further constrain the internal mechanisms that govern the upper layers of Jupiter: The odd-harmonics are indeed related to the wind dynamics.

Parameter	Value	Uncertainty (3-sigma)
GM_{jup} (km^3/s^2)	126686534.27	2.80
J_2 $(\times 10^6)$	14696.572	0.014
C_{21} $(\times 10^6)$	-0.013	0.015
S_{21} $(\times 10^6)$	-0.003	0.026
C_{22} $(\times 10^6)$	-0.000	0.008
S_{22} $(\times 10^6)$	0.000	0.011
J_3 $(\times 10^6)$	-0.042	0.010
J_4 $(\times 10^6)$	-586.609	0.004
J_5 $(\times 10^6)$	-0.069	0.008
J_6 $(\times 10^6)$	34.198	0.009
J_7 $(\times 10^6)$	0.124	0.017
J_8 $(\times 10^6)$	-2.426	0.025
J_9 $(\times 10^6)$	-0.106	0.044
J_{10} $(\times 10^6)$	0.172	0.069
J_{11} $(\times 10^6)$	0.033	0.112
J_{12} $(\times 10^6)$	0.047	0.178

TABLE 3.3: Jupiter's gravity field from the multi-arc solution with PJ03 and PJ06 data.

Figure 3.5 display the gravity harmonics (to degree 12), and associated 3-sigma formal uncertainty. It is clearly visible that the first low-degree odd harmonics are estimated with a remarkable accuracy.

To study the stability of the solution, single-arc estimates are compared to the multi-arc solution. Figure 3.6 display the 3-sigma error ellipses for different pairs of gravity harmonics. Even and odd harmonics are plotted separately since they relate to two different phenomena of gravity field generation: Solid body rotation and atmospheric dynamics.

The multi-arc solution is compatible with the single-arc solution within the 3-sigma level, since the central value is contained in all the single arc error ellipses, for all the gravity coefficients reported. The multi-arc solution is thus consistent with the gravity fields estimated using only one data set at a time, confirming the correctness of the selected set of estimated parameters. The error ellipses also show the large correlation of high-degree harmonics (see for example J_7 vs J_9). In fact, the ellipses are more flatter than the J_2-J_4 ellipses. This is related to the orbital geometry, that does not allow to disentangle the effects of successive high-degree harmonics.

In single-arc solutions, low degree harmonics are generally correlated with the spacecraft's state vector. From Figure 3.6, it is evident that the low degree harmonics benefit the most from the multi-arc approach. The multi-arc method helps to reduce their correlation with the spacecraft trajectory.

Concerning Jupiter's tidal response, only the Love number k_{22} has been estimated. As previously mentioned, higher degree Love numbers are set to the values predicted by

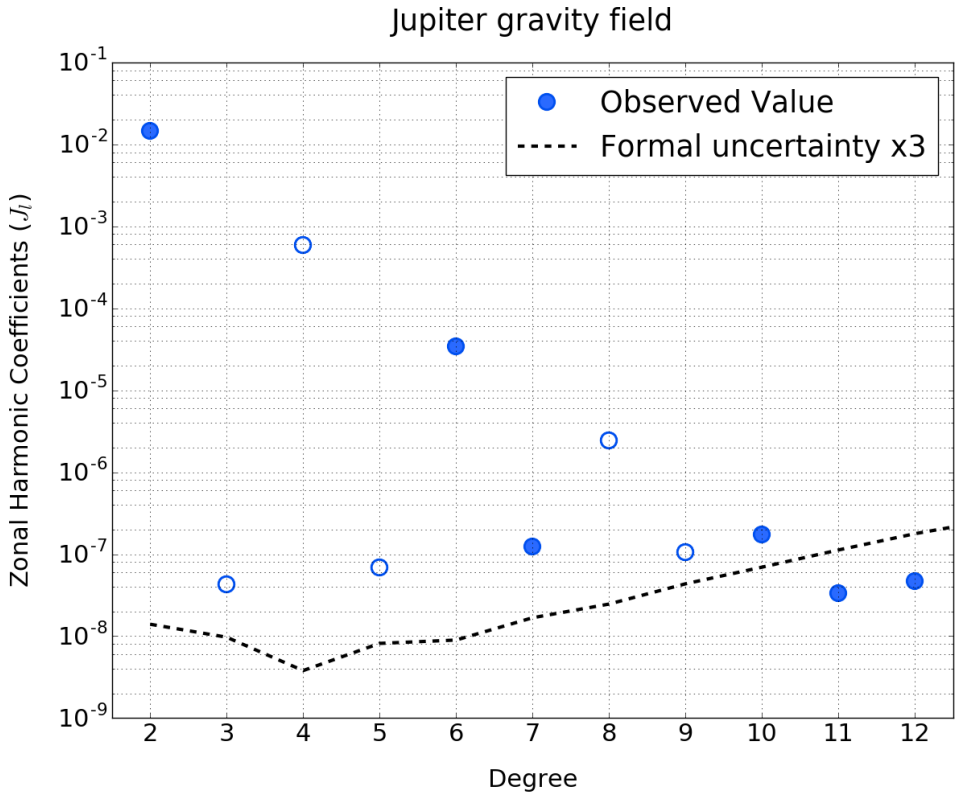

FIGURE 3.5: Un-normalized gravity field harmonics for the multi-arc solution. Filled circles indicate a positive value, empty circles stand for negative values.

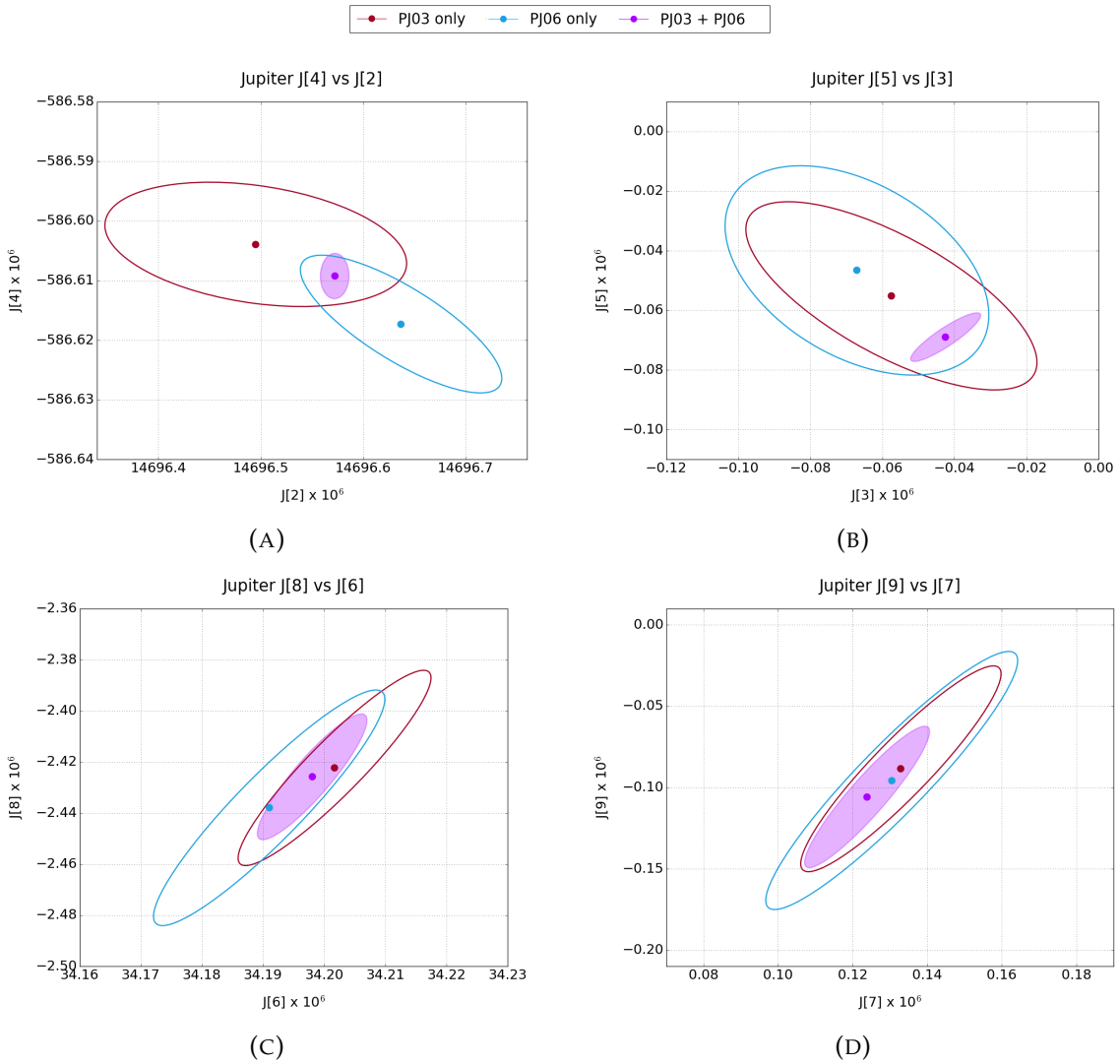

(A) (B)

(C) (D)

FIGURE 3.6: Error ellipses (3-sigma) for different pairs of low degree gravity harmonics. Single arc solutions are compared with the multi-arc solution.

Parameter	Theoretical value	Estimate ($\pm$ 3-sigma)
k_{22}	0.590	0.625 ± 0.063

TABLE 3.4: Estimate of Love number k_{22} compared with theoretical predictions.

Wahl, Hubbard, and Militzer, 2016, with a consider uncertainty of 20%. Imaginary Love numbers have been set to zero and un-estimated, due to the limited number of passes. In fact, the limited coverage of the tidal bulge prevents a good determination of the tidal response of Jupiter, and in particular of the phase lag associated with tidal dissipation. This is one of the remaining questions Juno will hopefully answer in the future. A frequency dependence of the tidal response of the gas giant may also be investigated.

Table 3.4 reports the estimated value (and associated 3-sigma uncertainty), to be compared with the theoretical prediction by Wahl, Hubbard, and Militzer, 2016. The estimation uncertainty is still quite large, and the central value is recovered with a relative accuracy of about 10%. The theoretical value is fully compatible with the estimated value.

The last subset of parameters that has been determined with the Juno gravity experiment is Jupiter's spin axis inertial direction. The location of Jupiter's pole is fundamental for gravity field determination, since the gravitational potential of a planet is defined in the so-called body-fixed frame, i.e, the frame associated with the body. Although the definition is clear for a rocky planet, being a solid body rotating uniformly, the definition of a body-fixed frame for a gas giant is not trivial. We can associate a body fixed frame to the rotation of the deep interior of a gas giant. One of Juno goals is also to understand how the gas giant behaves under its layer of clouds. The pole of a gas giant is somehow easier to define, being associated with the total angular momentum of the planet, which is supposed to be perfectly aligned to its principal axis of inertia, and thus to the spin axis. Deviations from the perfect alignment are expected to be very small, and may be detected by Juno during the next passes.

Tracking the motion of Jupiter's spin axis is fundamental for constraining its interior structure: the rate at which the pole moves in the inertial space is inversely proportional to the polar moment of inertia (MOI), which is a crucial parameter for assessing the presence of a core. Jupiter's MOI can been inferred from Jupiter's obliquity (Ward and Canup, 2006), and set to C=0.236. Interior models can also compute the value for the MOI, thus its determination would be very important for constructing fully consistent interior models. Juno can measure the spin axis rate with good accuracy, improving our knowledge about the interior of the gas giant (Le Maistre et al., 2016; Helled et al., 2011).

Current data does not allow the rate of Jupiter's pole to be determined with a good accuracy, but its location can be estimated and compared with current predictions. The most up-to-date model is IAU 2010 (Archinal et al., 2011), where the pole motion is described by:

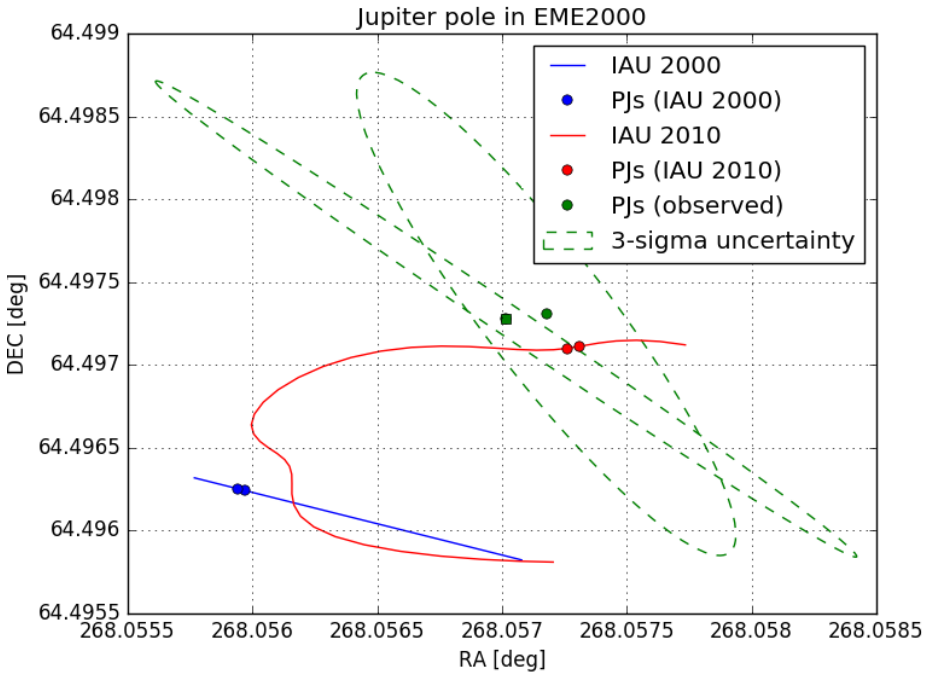

FIGURE 3.7: Jupiter's pole direction: blue and red curves are, respectively, IAU 2000 and IAU 2010. Dots refer to PJ03 and PJ06 epochs, and the green dots and ellipses refer to Juno's estimation.

$$\begin{aligned} \alpha_0 &= 268.056595 - 0.006499\,T + \sum A_k\, sinJ_k \\ \delta_0 &= 64.495303 + 0.002413\,T + \sum B_k\, cosJ_k \\ W &= 284.95 + 870.5360000\,d \end{aligned} \tag{3.35}$$

The quantities α_0, δ_0 are the standard equatorial coordinates (in degrees) with equinox J2000 at epoch J2000, namely the right ascension and declination of the rotation axis. The prime meridian, whose definition is arbitrary for a gas giant, is denoted by W. T is time expressed in Julian centuries (of 36525 days), and d is expressed in days, both from the reference epoch. The trigonometric quantities A_k, B_k, J_k are reported in Archinal et al., 2011. The IAU 2000 rotation model (Seidelmann et al., 2002) supposes only a linear motion for the spin axis:

$$\begin{aligned} \alpha_0 &= 268.05 - 0.009\,T \\ \delta_0 &= 64.49 + 0.003\,T \\ W &= 284.95 + 870.5366420\,d \end{aligned} \tag{3.36}$$

Figure 3.7 shows the location of the spin axis according to both the models, along with the location determined by Juno. The dots refer to the PJ03 and PJ06 epochs, where the determination of the spin axis is more accurate. Currently, with only two passes, it

is difficult to comment on this result. We may note that Juno's estimate is compatible, at 3-sigma, with the pole location predicted by IAU 2010 model with the Juno estimate. Future passes will surely increase the confidence on Jupiter's rotation model.

3.3.4 Statistical analysis of residuals

To conclude the analysis of the Juno Doppler data, we report in Figure 3.8 the Allan deviations and Power Spectral Density (PSD) for the data set analyzed. The Allan deviations and PSDs are evaluated starting from Doppler data at 1 second, computed on the reference trajectory obtained with the multi-arc solution.

Allan deviations do not show indications of thermal noise at low integration time scale (1 to 10 s): The processing of Open-Loop data with a software PLL drastically reduces the noise at short time scale. Thermal noise follows indeed a characteristic law of τ^{-1}. At higher time-scales, in the band of the gravity signals, the noise is approximately white, and the Allan deviation follows the power law $\tau^{-1/2}$. This is one of the conditions required by the least square filter for a maximum likelihood estimate, which is therefore satisfied.

The power spectral density of the two passes is also easily interpretable. The noise is almost white, with a flat spectrum. The exception is on low frequencies (large time-scales), where a residual signature due to the orbital fit may be present. This is, however, at frequencies lower than those characteristic of the gravity field harmonics. Other remarkable signals are found at the spin frequency (Juno rotates at 2 RPM, 0.033 Hz) and its multiple. This is believed to be caused by Juno's antenna phase pattern, which induces a small Doppler shift at frequencies multiple of the spin frequency. This spurious signal does not interfere with the determination of the gravity field since the data have been compressed at 60s, averaging out those signals. Note that in PJ06 the harmonics have more power since the Earth aspect angle was slightly larger than in PJ03.

3.4 Cassini data analysis

In this section, the analysis of Cassini gravity data acquired during the Grand Finale orbits is reported, to study Saturn's gravity field. Table 3.5 summarizes the pericenter passes completed by Cassini that are dedicated to gravity science investigations.

Cassini completed a total of 22 orbits prior to its final plunge into Saturn's atmosphere on 15 September 2017. Six orbits were dedicated to the study of Saturn's gravity field. Unfortunately, the data acquired during REV275 were not collected by the Malargue complex due to an acquisition problem. Thus, the data from this orbit have not been analyzed, since the Doppler data acquired prior to and following the C/A are too far from Saturn to contribute significantly to the determination of Saturn's gravity field.

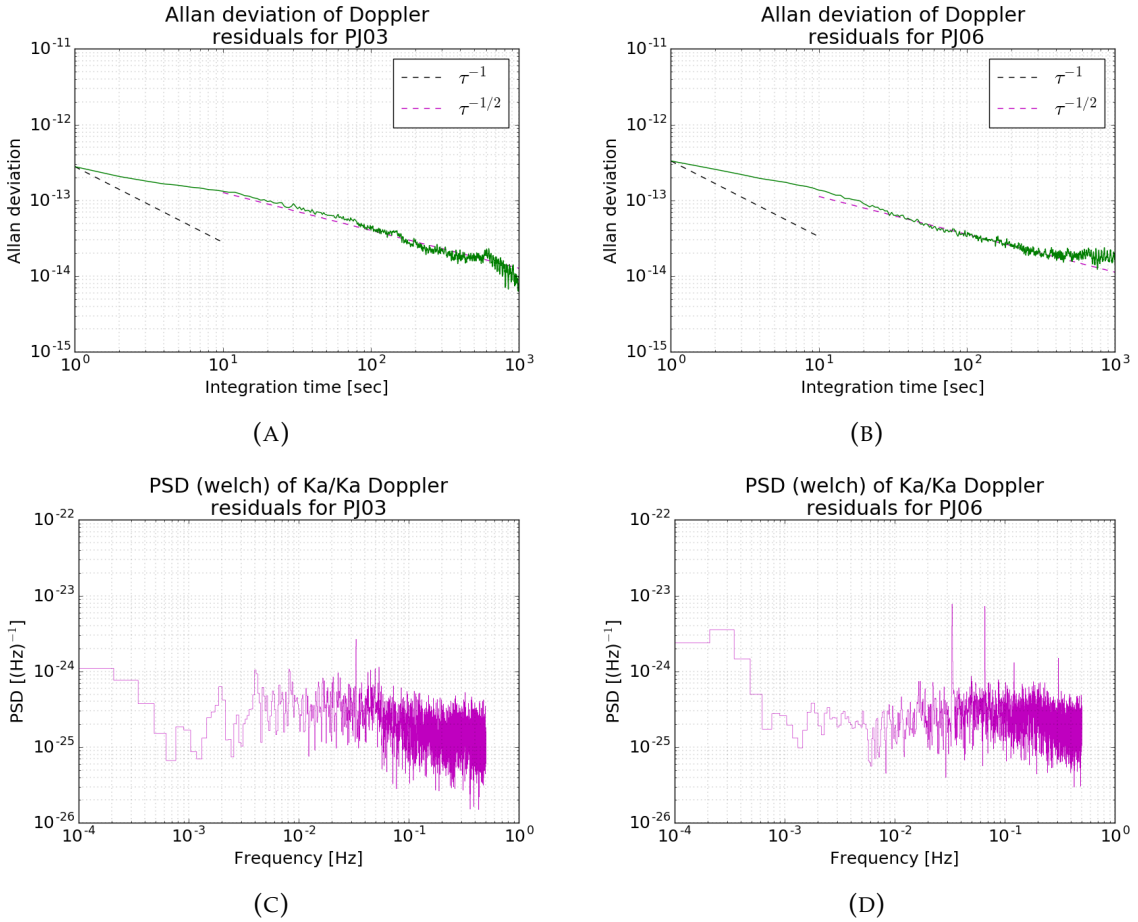

FIGURE 3.8: Allan deviation (top panels) and PSD (estimated with the welch method, bottom panels) for Juno PJ03 (panels A and C) and PJ06 (panels B and D).

Proximal Orbits	Date of C/A	Complex acquiring data at C/A
REV273	9 May 2017	Malargue
REV274	15 May 2017	Canberra
REV275	22 May 2017	Data not acquired by Malargue
REV278	10 June 2017	Canberra
REV280	23 June 2017	Canberra
REV284	19 July 2017	Canberra

TABLE 3.5: Summary of Cassini's Grand Finale orbits devoted to Saturn's gravity investigation.

Cassini was tracked by DSN's and ESA's antennas during a 24-hour window, about the C/A, in order to acquire also ring occultation data. In fact, the radio signal crosses Saturn's rings on different occasions. During ring occultation, Cassini passes in between the rings and Saturn's cloud top and the signal is occulted by the rings (close ring occulation). The more massive B-ring causes a drastic drop in the signal amplitude, and Doppler data are not acquired for approximately 10 to 15 minutes in that time frame. Other rings have a smaller effect on the Doppler noise, but the frequency of the signal can be easily recovered. After that phase, due to the orbital geometry, the signal is occulted again after the pericenter passes, in the so-called distant ring occultation. The occultation lasts for a few hours, and the data acquired are used to recover the optical depth of the rings, rather than for gravity science. For gravity investigation, Doppler data at X-band was used and compressed to 30s.

3.4.1 Dynamical model and observables

Cassini's dynamical model accounts for several effects, both gravitational and non-gravitational accelerations. It includes:

- Relativistic acceleration from Saturn and its satellites
- Spherical harmonic expansion of Saturn's gravity field (static and time-varying)
- Gravitational acceleration due to the rings (A-ring, B-ring, and C-ring)
- Newtonian (point-mass) acceleration from all the other Solar System's planets
- Tides raised on Saturn from the satellites
- Lense-Thirring relativistic acceleration caused by Saturn's rotation
- Solar radiation pressure on Cassini
- Non isotropic acceleration from the onboard RTGs
- Drag acceleration due to H_2 particles of Saturn's atmosphere

Cassini's dynamical model has been heavily tested during the past number of years, for the tour of Saturn's moons. It accounts for all the major accelerations acting on the spacecraft, which are mainly gravitational accelerations. In addition, solar radiation pressure and the non-isotropic acceleration from the onboard RTGs (Radioisotope Thermoelectric Generator) has been included, as well as the small drag effect coming from Saturn's upper atmosphere (mainly induced by H_2).

The determination of Saturn's gravity field is a major goal for Cassini's Grand Finale orbits. The determination of the low degree even and odd harmonics is of great interest

from a geophysical point of view. In fact, as for Jupiter, the gravity field of the planet contains important information about the interior structure and its density profile. In addition, anticipating the results, the higher number of gravity passes may help in the determination of the time-varying gravity coefficients.

Apart from Saturn's gravity field, the ring system fulfills a fundamental role: an independent determination of their masses (namely, the B-ring mass) has important implications in constraining the age of Saturn's ring. The gravitational acceleration coming from the rings is thus included in Cassini's dynamical model.

Concerning the Lense-Thirring effect, the resulting acceleration is inaccessible with the Cassini Doppler data. However, with the aim of obtaining a realistic dynamical model for Cassini, it has been included when integrating the spacecraft trajectory. Note also that the precession experienced by Cassini due to Saturn's Lense-Thirring effect is way smaller than the one experienced by Juno due to Jupiter's larger mass.

The Doppler observables' model is the same that was used for Juno, thus accounting for the relativistic effects on wave propagation as proposed by the theory of general relativity.

Since Cassini is a three-axis stabilized spacecraft, the Marini effect, a correction to the observables caused by the rotation, is generally not relevant. However, during REV273 and REV284, the spacecraft was spinning around the antenna axis for calibration purposes, and this effect must be taken into account.

3.4.2 Single-arc setup and solutions

The Doppler data acquired during Cassini's Grand Finale orbits are first analyzed as single arcs, and then a combined solution is researched. The least-square information filter solves for:

- Spacecraft state at given epoch
- Saturn's gravitational parameter μ_{sat}
- Saturn's rings' masses (to be precise, only the more massive B-ring is resolved)
- Saturn's zonal spherical harmonics (up to degree 20)
- Saturn's tesseral field to degree 2
- Saturn tidal response (Love number k_{22})
- Saturn's spin axis inertial direction

The single arc solution can be easily fitted with the proposed set of parameters. However, the multi-arc solution does not fit the Doppler data when the estimated parameter list is limited to considering only the above-mentioned effects.

The components of Cassini's state are estimated and referred to approximately 12 hours prior to the closest approach, when the tracking begins. The a priori values for position and velocity are, respectively, 100 km and 1 m/s.

Saturn's gravitational parameter and its uncertainty are set to the values estimated from the motion of Saturn's satellites. To be precise, since Saturn's gravitational parameter contained in the planetary ephemeris includes the rings' masses, the sum of Saturn's mass and ring's masses has been constrained to be equal to the value (and uncertainty) estimated for Saturn, prior to the Grand Finale orbits. Cassini's orbital geometry is not appropriate to better estimate Saturn's gravitational parameter, but, in principle, it can allow disentangling the ring's weak acceleration from the gravity coefficients, since the spacecraft passes between the rings and the planet.

The minimum set of spherical harmonic coefficients able to fit the Doppler data to the noise level for Cassini is given by zonal harmonics up to degree 20, and a tesseral field of degree 2 (full quadrupole coefficients), when considering single arc solutions. As a priori uncertainty, a value of 10^{-5} for all the harmonics has been selected, which does not constrain the solution.

Saturn's Love number k_{22} has been estimated, but it is unresolved with single arc estimates (the formal uncertainty is larger that the central value).

Concerning the spin axis direction, Saturn's rings define its equatorial plane, and in the past number of years a lot of observations of Saturn's rings yielded a very accurate determination of Saturn's equator, and thus of its spin axis direction (French et al., 2017). The spin axis is constrained to the position determined by ring occultation data, which is much more accurate than what can be achieved with gravity field determination.

Figure 3.9 display the single-arc solutions obtained with the proposed set of estimated parameters, for a few pairs of low-degree gravity harmonics. The error-ellipses are at 3-sigma. The solutions are not all consistent at that level, and the central values estimated are not stable enough.

3.4.3 Multi-arc approach

As previously reported, the set of parameters able to separately fit the arcs is not sufficient to fit the data in a multi-arc solution. This leads to the assumption that an acceleration is missing in Cassini's dynamical model. One option is to include the presence of normal modes in the estimation filter, which is a non-trivial task. The inclusion of normal modes poses a few important questions:

- Which modes are relevant?
- What are the amplitudes and frequencies of these modes?

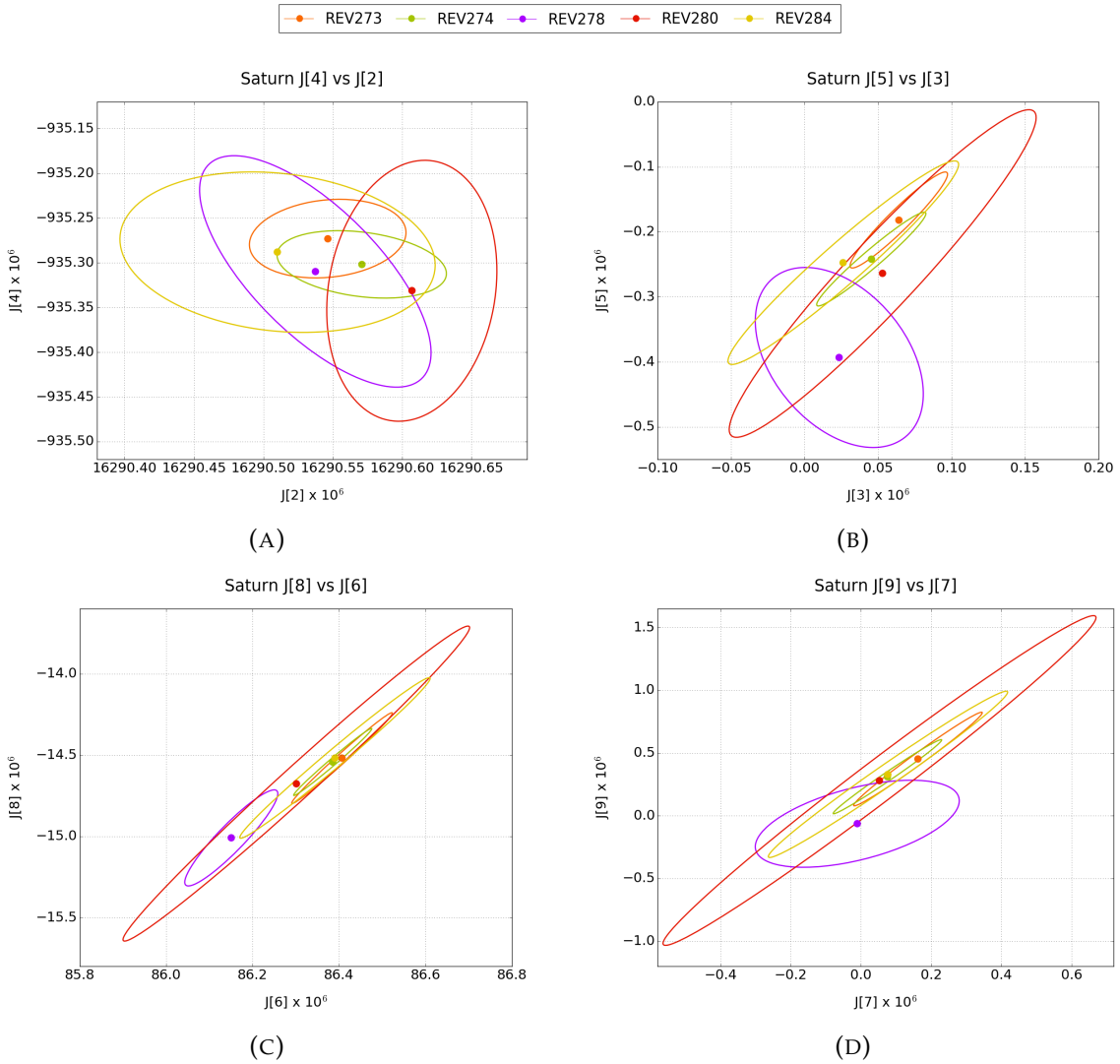

(A) (B)

(C) (D)

FIGURE 3.9: Error ellipses (3-sigma) of single-arc solutions for different pairs of low degree gravity harmonics.

The first question is the most difficult to answer. The amount of possible modes is infinite, and both gravity and acoustic modes exist. In addition, through the gravity experiment, the discrimination of the modes is almost impossible. Since Cassini is sensitive to the acceleration induced by the normal modes only in a very limited amount of time, a large correlation exists between the different modes, and a clear detection of a particular mode is denied. Thus, in principle, Cassini is sensitive to a time-varying gravity field, but is not able to determine which modes exist. Several solutions are possible.

The second question is related to the first, and can be partially solved. The classical orbit determination problem exploits a least-squares filter to solve for dynamical model parameters. Thus, the amplitude and frequency of the mode may be, in principle, solved for. Recall that the effect of acoustic oscillations on zonal gravity field is modeled as (Durante, Guillot, and Iess, 2017):

$$J_l = J_l^{STATIC} + \sum_{n\geq 0} \widetilde{J}_{l,n}(t) \tag{3.37}$$

$$\widetilde{J}_{l,n}(t) = \widetilde{J}_{l,n}\ \cos(\omega_{l,n}t + \phi_{l,n}) = \widetilde{J}^C_{l,n}\ \cos(\omega_{l,n}t) + \widetilde{J}^S_{l,n}\ \sin(\omega_{l,n}t) \tag{3.38}$$

For each mode, one should solve for an amplitude and a phase (or equivalently the alternative, preferred representation with a cosine and a sine term) and possibly a frequency. However, a few difficulties arise. The frequency of the modes is nearly impossible to solve, since it is highly non-linear, and the OD problem is sensitive to non-linearities in the dynamical model. Simulations show that the non-linearity of the problem for the frequency prevents the filter from reaching a converged solution. The modes' frequencies are thus unresolvable.

The inability to estimate the frequency of a selected mode poses another important question. Since an error in the frequency propagates with time and consecutive REVs are separated by weeks, this would result in a completely incorrect mode phase by the time Cassini would have reached its closest-approach with Saturn. For example, an error of 1 minute on the degree 2 fundamental acoustic mode (whose period is about 3 hours) corresponds to a difference of one full cycle (2π) after about 22 days, which is less that the total duration of Cassini's Grand Finale orbits (see Table 3.5).

For that reason, the approach pursued is to estimate the initial phase of a selected mode as a local parameter, and constrain the amplitude to be consistent for all the REVs. As an a priori uncertainty for the magnitude of the modes, we selected a value of $3.0{\cdot}10^{-8}$, which constrains the modes to be small, according to geophysical expectations (bases on excitation mechanism and dumping considerations). In addition, this is the minimum value able to fit the data consistently. This allows the mitigation of the error in frequency through an over-parametrization of the problem. The frequency is fixed to those predicted by the models, in particular, the $Sa8$ model from Gudkova and Zharkov, 2006.

Five different sets of gravity and/or acoustic modes were selected, all including only zonal coefficients. Normal modes on a tesseral field are not included since the amplitudes estimated from ring seismology are too small to be detected with the Cassini radio instrumentation. The sets of normal modes selected are:

- f-modes: Only fundamental modes $\widetilde{J}_{l,0}$ are estimates, from degree 2 to 10
- f+p-modes: Fundamental modes from degree 2 to 6, and the first few low-degree low-radial order p-modes (on degree 2 to 4, first and second overtone)
- g+f-modes: Gravity modes on degrees 2 and 3, plus fundamental modes up to degree 6
- g+f+p-modes: Gravity and acoustic modes, on degree 2 and degree 3 only
- g+f+p-modes (full): Gravity modes on degree 2 and 3, f-modes up to degree 10, p-modes up to degree 4 (first and second overtones)

All the selected sets of normal modes fit the data to the noise level. As a reference, the solution named g+f-modes is selected since it is one of the most consistent (along with the g+f+p-mdoes (full), which solves for the largest number of parameters). See next section for a more complete discussion.

3.4.4 Results

The Doppler residuals at an integration time of 30 s, converted in mm/s for convenience, are reported in Figure 3.10, for the reference solution. Note that all the other solutions fit the data at the same level, and no signatures are found near the pericenter. The data quality is good (see Table 3.6), and the best performance is achieved on REV278, with an RMS noise of $0.020\ mm/s$ at the C/A. During REV 280, the RMS noise level is $0.088\ mm/s$, more than four times the best value achieved. Thus, we can expect that the data coming from this REV do not contribute to a drastic reduction of the uncertainty of the multi-arc solution (as a crude approximation, for a given geometry, the information matrix elements sum up with the inverse power of two of the noise in the data).

We report only residuals during the C/A tracking period, which are the most relevant. The Doppler data far from the C/A helps to constrain the inbound and outbound trajectory of Cassini, reducing the correlation between the low-degree gravity coefficients and the state vector. With respect to Juno, much more data far from C/A have been acquired by Cassini, since it has been possible to avoid any re-pointing maneuver after the closest approach. On the contrary, Juno has to perform an Orbit Trim Manuver (OTM) for navigation purposes.

REV	Date of C/A (ERT)	Doppler noise (RMS)
273	09 May 2017 07:35	$0.029\ mm/s$
274	15 May 2017 18:04	$0.023\ mm/s$
278	10 June 2017 14:12	$0.020\ mm/s$
280	23 June 2017 12:10	$0.088\ mm/s$
284	19 July 2017 09:15	$0.044\ mm/s$

TABLE 3.6: Cassini C/A data (in Earth-Received Time, ERT) and data quality for the C/A tracking pass.

Parameter	Value	Uncertainty (3-sigma)
GM_{sat} (km^3/s^2)	37931206.00	3.74
J_2 $(\times 10^6)$	16290.564	0.042
C_{21} $(\times 10^6)$	0.003	0.006
S_{21} $(\times 10^6)$	0.004	0.007
C_{22} $(\times 10^6)$	-0.004	0.006
S_{22} $(\times 10^6)$	0.005	0.007
J_3 $(\times 10^6)$	0.079	0.059
J_4 $(\times 10^6)$	-935.281	0.071
J_5 $(\times 10^6)$	-0.261	0.097
J_6 $(\times 10^6)$	86.395	0.150
J_7 $(\times 10^6)$	0.018	0.190
J_8 $(\times 10^6)$	-14.533	0.294
J_9 $(\times 10^6)$	0.190	0.303
J_{10} $(\times 10^6)$	4.746	0.435
J_{11} $(\times 10^6)$	-0.555	0.426
J_{12} $(\times 10^6)$	-0.960	0.596

TABLE 3.7: Saturn's gravity field from the multi-arc solution which includes g-modes and f-modes.

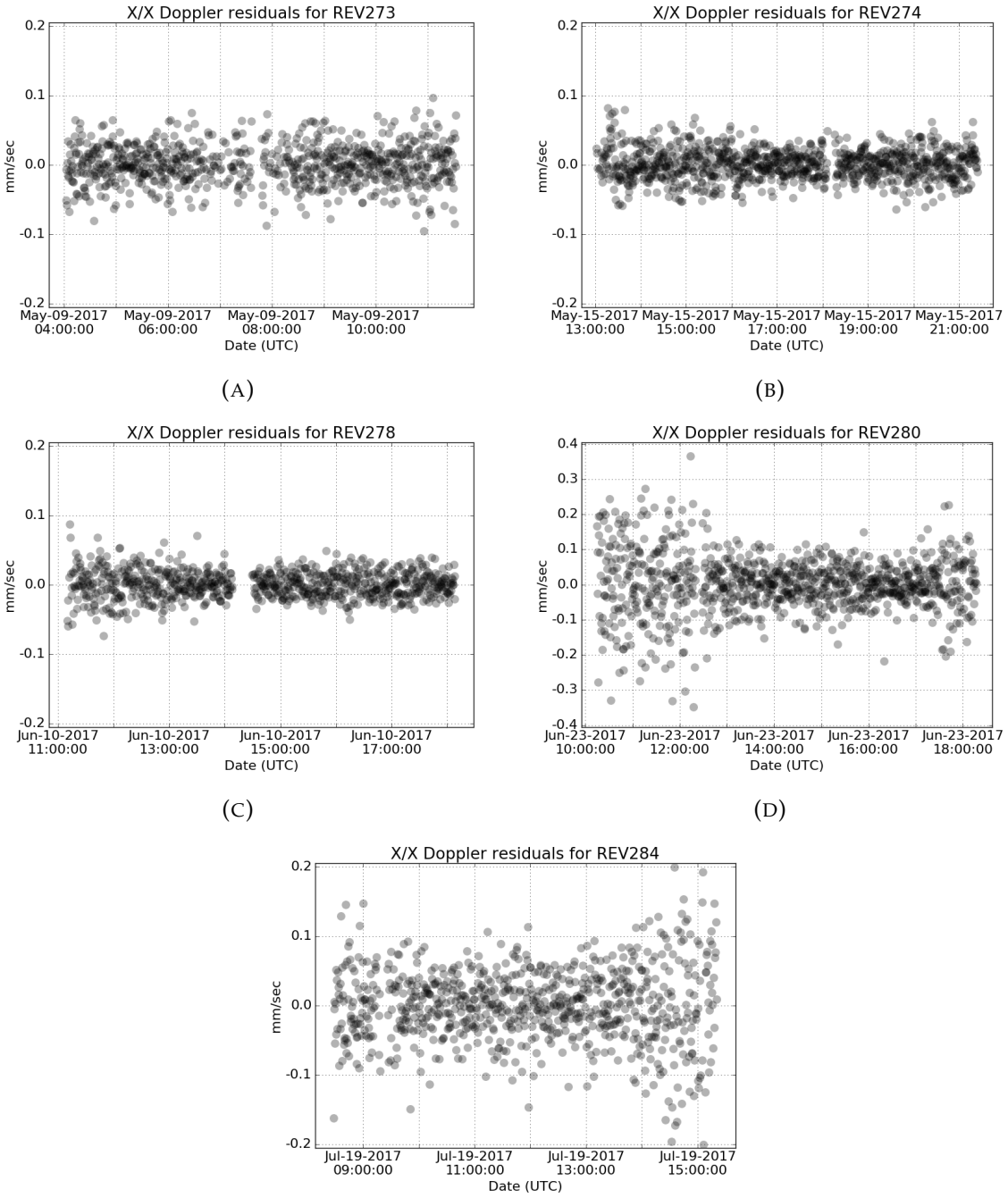

FIGURE 3.10: Doppler residuals for: (A) REV273, (B) REV274, (C) REV278, (D) REV280, and (E) REV284. Note the different limits for the y-axis of REV284.

The multi-arc solution for the g+f-modes case is reported in Table 3.7, including estimated values and the 3-sigma formal uncertainty for the gravity coefficients.

The uncertainty on Saturn's gravitational parameter is essentially fixed to the a priori value dictated by the analysis of Saturnian ephemeris (Jacobson et al., 2006). The most remarkable difference obtained with Saturn's Grand Finale orbits is the disentanglement of the contribution coming from the rings and that associated directly with Saturn (the gravitational parameter estimated from the Saturnian ephemeris includes the rings' masses, since Cassini never passed so close to Saturn to disentangle the two effects).

For the gravity field coefficients, the Grand Finale orbits enabled an accurate determination of Saturn's gravity field. Prior to this phase of the Cassini mission, only J_2, J_4, and J_6 where determined with sufficient accuracy. The formal uncertainty on J_2 decreased by about a factor of 20 whereas for J_4 and J_6 the improvement is larger than two orders of magnitude. In any case, the previous solution (Jacobson et al., 2006) is statistically compatible at 1-sigma with the new estimate from Cassini's Grand Finale orbits.

The new solution drastically increases the precision on the determination of higher-degree even harmonics, such as J_6, J_8, and J_{10}, which are crucial for determining the interior structure and the internal characteristics of the planet. In addition, for the first time, the Doppler data acquired enabled a reliable estimate of the low-degree odd gravity harmonics. Among them, only J_3 and J_5 are estimated over the 3-sigma level. In particular, the latter is very well determined, with the central value estimated at about 8-sigma. This asymmetric field is a clear indication that something inside Saturn is not axially symmetric, as expected from a rotating fluid body in hydrostatic equilibrium.

Figure 3.11 display the gravity harmonics (to degree 12), and associated 3-sigma formal uncertainty. The filled circles indicate positive values for the particular harmonic coefficients, whereas negative harmonics are marked with an empty circle. This representation helps to identify which harmonics are determined with a good accuracy, i.e., the estimated value is over the 3-sigma level. In any case, a value close to zero provides also important information for constraining the internal dynamics, since it represents an upper bound.

Figure 3.12 shows the error ellipses (3-sigma) for the five solutions selected, for the first few low-degree static components of Saturn's gravity, which are those more important from a geophysical point of view. In general, there is a good consistency between the different solutions, all grouped together. The different correlation and sigmas are due to the different modes selected for each solution. The larger ellipses are, of course, found for the g+f+p-modes (full) case, where there are more modes than the ones strictly needed to fit the data (as in the other cases). Among the others, the solution selected as a reference (the g+f-modes) shows consistency with all the other solutions, and simultaneously has smaller uncertainties for the gravity coefficients when compared to the g+f+p-modes (full).

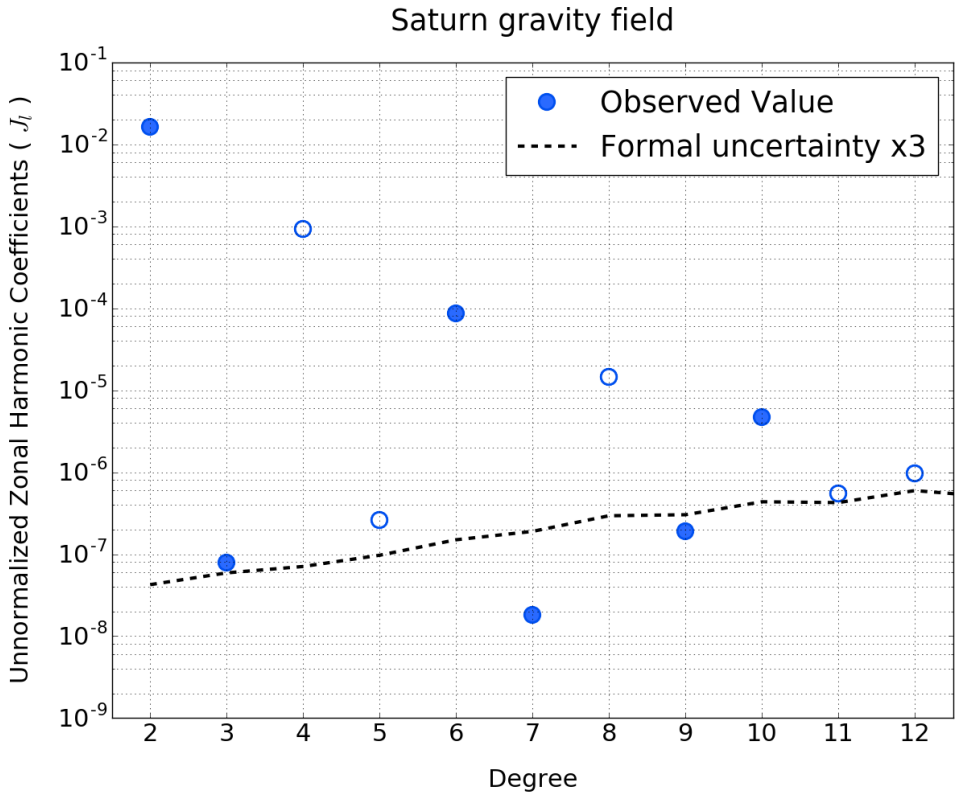

FIGURE 3.11: Un-normalized gravity field harmonics for the reference multi-arc solution. Filled circles indicate a positive value, empty circles represent negative values.

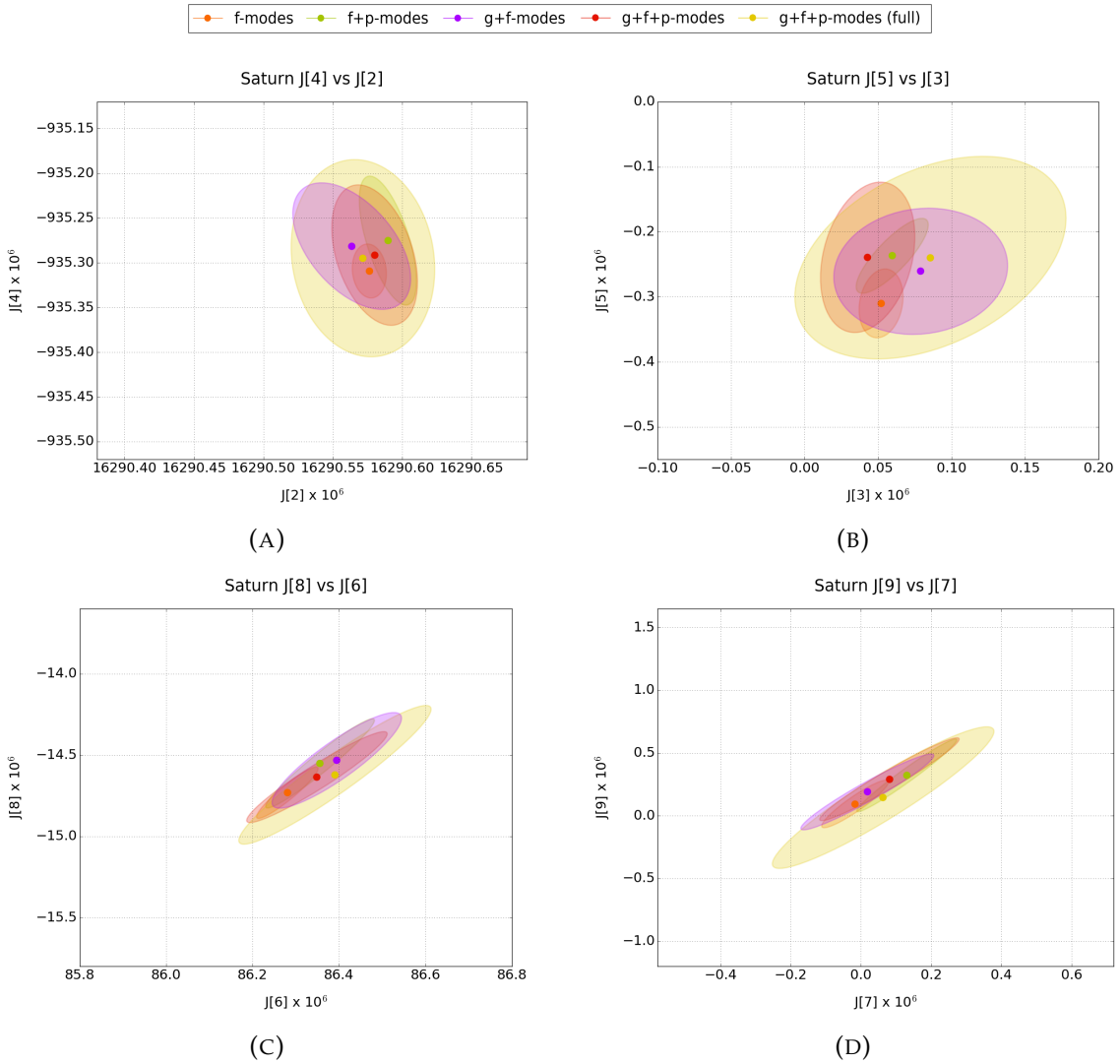

(A) (B)

(C) (D)

FIGURE 3.12: Error ellipses (3-sigma) of several multi-arc solutions for different pairs of low degree gravity harmonics.

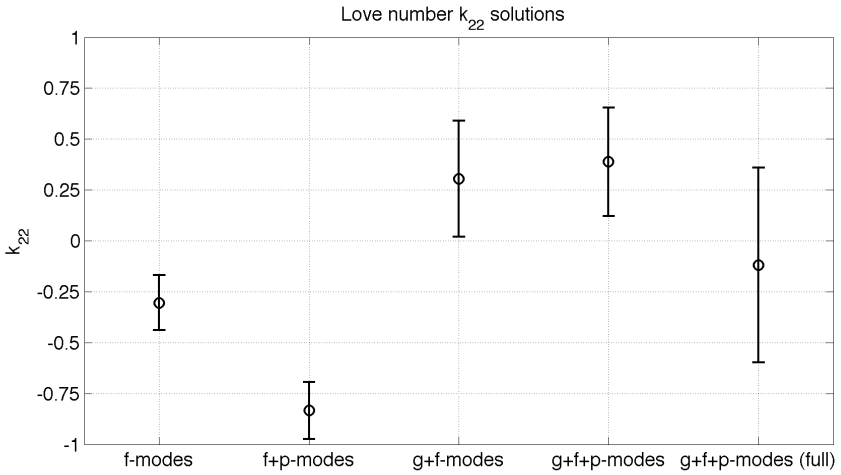

FIGURE 3.13: Love number k_{22} estimates, with 1-sigma uncertainty, for the different set of normal modes.

In contrast to Juno, the Cassini multi-arc solutions do not dramatically improve the uncertainties with respect to the single-arc solution. This is caused by the need to include normal modes when solving all the arcs together. The larger set of solved parameters is thus responsible for an increase in the estimation uncertainties. Also, the single-arc solutions underestimate the uncertainties for the static field component since it neglects the presence of normal modes. The multi-arc solution is thus more robust, including all the data acquired.

As for Juno, the high-degree gravity harmonics are highly correlated. The low-degree coefficients are generally more correlated with the state vector, and with the normal mode coefficients, which are (according to the set selected) mostly oscillations on the low components of Saturn's gravity field.

Concerning the Love number k_{22}, the situation is more difficult to interpret. Figure 3.13 shows the different estimates of the Love number for the set of normal modes selected, at 1-sigma. The previously estimated value for Saturn's Love number is $k_{22} = 0.39 \pm 0.024$ (Lainey et al., 2017). The value they found also agrees with interior models for Saturn (Wahl, Hubbard, and Militzer, 2017). The uncertainties of the different solutions reported here is about one order of magnitude larger than the previous estimate, thus a better determination of Saturn's tidal response is not possible. However, the estimates of Saturn's Love number can be used to assess the consistency of these solutions with the previously estimated value.

From Figure 3.13 it is clear that the first two solutions (f-modes and f+p-modes) estimate a negative value for k_{22}, which is hardly interpretable (not impossible, but it requires unconventional physics, D. Stevenson private communication). In addition, even

at 3-sigma, the previous estimate is not compatible. This indicates that the first two solutions have a bias in the estimation. Durante, Guillot, and Iess, 2017 demonstrated that even in the presence of normal modes with small amplitudes, a bias at a level of few sigmas can be found for the Love numbers (the simulations were made for Juno and Jupiter, but the same applies to Cassini and Saturn).

In contrast to the first two solutions, the other three (which all include the presence of gravity modes) estimate a value which is compatible at 1-sigma with the value found by Lainey et al., 2017. The estimate of the reference solution is:

$$k_{22} = 0.305 \pm 0.285 \tag{3.39}$$

This may be an indication that gravity modes are more adequate to fit the Doppler data, producing an estimate of the Love number k_{22} statistically compatible with previous estimates reported in the literature. Note: This is not strong evidence for the presence of gravity modes, and may be a coincidence.

Concerning the B-ring mass estimation, all the solutions show a remarkable consistency. Figure 3.14 shows the estimate for the B-ring mass, with 1-sigma uncertainty, in terms of Mimas' mass (1 $M_M = 3.75 \times 10^{19}\ Kg$, or 6.3×10^{-6} Earth's mass). The estimate of the reference solution is:

$$\text{B-ring}|_{mass} = (0.36 \pm 0.18)\ M_M \tag{3.40}$$

Recent analysis on density waves found in the B-ring suggest that its masse is between one-third to two-thirds the mass of Saturn's moon Mimas (Hedman and Nicholson, 2016). The solution obtained with the analysis of Cassini's Grand Finale orbits is perfectly compatible with the theory proposed by these authors. It is an independent estimate of the B-ring mass, which is crucial for constraining the age of Saturn's ring system.

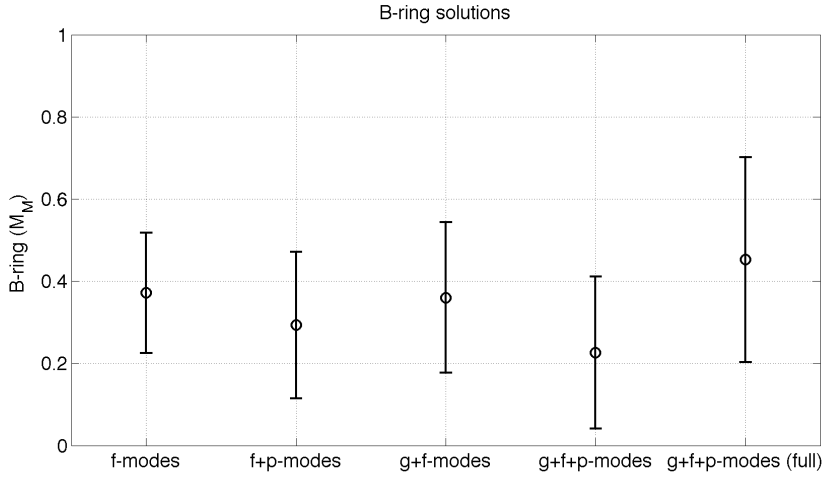

FIGURE 3.14: B-ring mass estimates, with 1-sigma uncertainty, for the different set of normal modes.

Chapter 4

Interpretation of results

The analysis of Jupiter and Saturn's gravity fields as determined by Juno and Cassini has been discussed in the previous chapter. Hereafter, the implications for the gas giants' interior structures are reported. The even part of the gravity field is strictly related to the deep interior structure, whereas the odd terms are caused by internal wind dynamics. However, the picture is more complicated, and a more complete discussion follows.

4.1 Deep interior structure

To start the discussion about Jupiter and Saturn interior structures, an analysis of the state-of-the-art interior models prior to Juno and Cassini data is required.

Table 4.1 contains the range of even gravity coefficients for Jupiter and Saturn due to the solid body contribution only, for a set of preliminary models, prior to Juno and Cassini data. In addition, the newly estimated gravity field coefficients are reported for comparison. Jupiter models are discussed on Hubbard and Militzer, 2016. Saturn models have been provided by B. Militzer (personal communication). All the models fit the mass, radius, and the gravity coefficient J_2.

Parameter	Jupiter		Saturn	
	Preliminary value	Estimate	Preliminary value	Estimate
J_2 ($\times 10^6$)	14696.43	14696.57	16290.71 $\pm$ 0.27	16290.56
J_4 ($\times 10^6$)	-601.72 to -587.14	-586.61	-938.62 to -933.19	-935.28
J_6 ($\times 10^6$)	34.17 to 35.77	34.20	80.53 to 81.74	86.39
J_8 ($\times 10^6$)	-2.608 to -2.450	-2.420	-8.95 to -8.68	-14.53
J_{10} ($\times 10^6$)	0.201 to 0.217	0.176	1.08 to 1.13	4.75

TABLE 4.1: Range of gravity coefficients based on Jupiter and Saturn preliminary models, priori to Juno and Cassini gravity data, compared with the new estimates. Data on the preliminary models are based, respectively, on Hubbard and Militzer, 2016 and on a personal communication with B. Militzer.

Jupiter's models reported in table 4.1 use an EOS based on DFT-MD theory (Militzer and Hubbard, 2013) and explore different assumptions for the interior structure. For Saturn, different rotation rates have been tested, but no differential rotation is involved. The helium rain layer is assumed either as a sharp boundary or an extended region, and no change in heavy elements is assumed across that layer.

By comparing the predictions with the actual observations from Juno and Cassini, a fairly different situation emerges for the two planets. Jupiter's preliminary models are in much better agreement with Juno's more accurate estimates, with the central values varying only slightly from the predictions (the special case is J_{10}, about 10% off). For Saturn, only the low-degree J_2 and J_4 are in agreement with the preliminary models, whereas for higher degree coefficients the difference is striking.

Concerning Jupiter, the preliminary models were actually quite accurate, since the range of possible gravity coefficients contains Juno's estimate. However, it should not be forgotten that Juno's accuracy is fairly tight when compared with the range of possible values due to interior models. For that reason, a closer look shows that even the preferred model from Hubbard and Militzer, 2016 does not precisely match all the gravity coefficients as determined by Juno. A refinement of these models is thus required.

Wahl et al., 2017 provides a first review of Jupiter's interior models and Juno data. Their work is based on Juno's estimate from the first two non-gravity dedicated orbits and not on the most updated reference solution from the gravity-dedicated orbits. In any case, the solution determined by Folkner et al., 2017 is fully compatible with the new reference solution, but since it does not exploit the more accurate Ka-band radio tracking system it has larger uncertainties.

Juno's data can be explained by the presence of a diluted core expanded to 0.3 to 0.5 times Jupiter's radius. A diluted core can arise since the central core materials, at the high pressure and temperatures found in the deep interior, become soluble in the outer metallic hydrogen envelope, and can expand outwards. However, the core erosion is a process whose efficiency is difficult to assess, just like determining if Jupiter has a fully eroded or an eroding core at the present age.

Wahl et al., 2017 also predict an enrichment in heavy elements in the deep envelope when compared with the outer, shallower region. This prediction is almost model-independent, as it shows up in all their models, and is unaffected by the selected EOS for the hydrogen-helium mixture. Regarding the core, it is supposed to contain a mass of heavy elements comparable to 7-25 Earth masses, out of 24-27 Earth masses worth of heavy elements in the whole planet. These masses, and the presence of a diluted core, are fully compatible with a formation scenario based either on core collapse or on dissolution of planetesimals. The uncertainty on EOS arises when determining the heavy element abundances. The REOS3 EOS predicts heavy elements to be 7-10 times the solar

fraction, whereas the preferred MH13 EOS, based on ab initio computer simulations of hydrogen-helium mixtures, predicts 5-6 times the solar fraction.

When analyzing the even gravity field, the effect of differential rotation must be taken into account. Kaspi et al., 2017 reports on this topic, stating that wind dynamics, i.e., differential rotation, affects the gravity spectrum at a level larger than Juno's formal accuracy. For instance, the dynamical range of ΔJ_4 is about 8×10^{-6}, with the current 3-sigma formal uncertainty being 4×10^{-9}; for ΔJ_6 the range is 4×10^{-6}, and the corresponding 3-sigma accuracy is 9×10^{-9}, i.e., a difference of about three orders of magnitude. Thus, when constructing interior models of Jupiter, the need for a correction due to the effect of wind dynamics poses important limits on the real accuracy that must be taken into account. However, since the wind dynamics affects the odd gravity spectrum, it is possible to infer, from that part of the gravity field, the decay depth of the wind, and use the same model to predict the effect on the even part of Jupiter's field. In such a way, it has been shown (T. Guillot personal communication) that the discrepancy found in J_{10} from interior models of Jupiter (matching the current estimate for the lower-degree even coefficients) to Juno's observed value can be explained with a correction given by wind dynamics, with a depth inferred from the odd gravity field (see Section 4.2).

Concerning Saturn, the only explanation for the large discrepancy in the higher-degree harmonics is a strong differential rotation of the interior. The small uncertainties on these gravity field coefficients enable models without differential rotation to be ruled out, which, on the contrary, fitted the previously estimated Saturn's gravity field (due to larger uncertainties). B. Militzer suggests a differential rotation with equatorial jets having a wind speed up to about 3.6% larger than the rest of the planet (see Figure 4.1). That is, the equatorial zonal flow is decoupled from the interior and proceeds with its own larger speed with respect to the internal regions. In addition, the larger speed of the equatorial region agrees qualitatively with cloud-tracking data and with occultation profile.

The differential rotation profile predicts a smaller rotation rate between 0.5 to 0.8 times Saturn's radius, corresponding to a latitude between 35 to 60 degree. This slower region is required to fit the gravity data, but no explanation has been found yet.

Y. Kaspi applied the thermal wind (TW) model to the Cassini data, analyzing the large discrepancies in the high-degree gravity coefficients, and found that the winds must penetrate to a depth of about 40,000 km, thus very deep inside the planet (Saturn's reference radius is 60,330 km). This finding agrees with the B. Militzer model, in which the equatorial region is found to be faster than the interior.

In addition, the thermal wind model matches the observed value of J_5, which is the only odd harmonics determined over the three-sigma level.

However, the TW model requires an adjustment to the surface winds profile, i.e. the surface wind speeds must be slightly modified to be able to fit the data. This is not

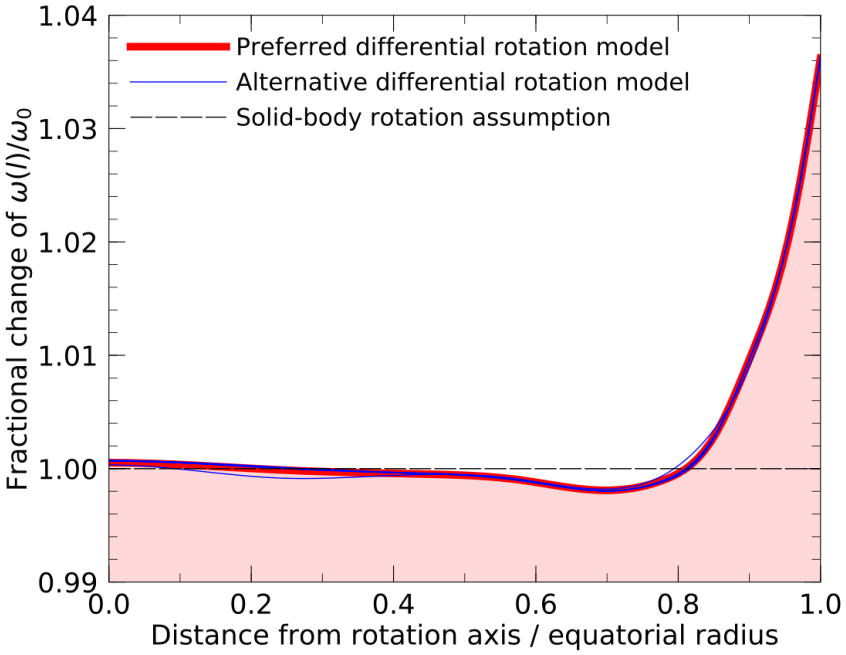

FIGURE 4.1: Fractional change of the rotation rate as a function of the distance from the rotation axis. Saturn differential rotation is very strong (B. Militzer personal communication).

the case for Jupiter, where the propagation of the observed surface winds enables an accurate fit of the gravity data. This means that the surface winds and the deep interior, only at particular high latitudes, may not match. This finding qualitatively agrees with B. Militzer models, making Saturn's high latitudes of particular interest.

To conclude, a detailed model of Saturn's interior is not yet available, due to the large surprise found in the Cassini data. Further investigations are ongoing, attempting to solve Saturn's mysteries in its interior structure.

4.2 Atmospheric flow inference

As heavily discussed, the atmospheric dynamics induce a perturbation to the gravity spectrum of a gas giant to a level that was predicted to be accessible to Juno and Cassini gravity measurements (Kaspi, 2013). The zonal flows observed on the surface of the two planets induce a correction to both even and odd harmonics. The contribution to the even gravity field, which modifies the interpretation of the deep interior structure, has been discussed in the previous section. Hereafter, the contribution of wind dynamics to the odd gravity spectrum will be discussed.

Table 4.2 lists the estimated values and associated uncertainties for Jupiter and Saturn's odd gravity coefficients, as determined by Juno and Cassini. Juno's more accurate

Parameter	Value ± 3-sigma	
	Jupiter	Saturn
J_3 ($\times 10^6$)	-0.045 ± 0.010	0.079 ± 0.059
J_5 ($\times 10^6$)	-0.070 ± 0.008	-0.261 ± 0.097
J_7 ($\times 10^6$)	0.119 ± 0.018	0.018 ± 0.190
J_9 ($\times 10^6$)	-0.116 ± 0.047	0.190 ± 0.303

TABLE 4.2: Jupiter and Saturn odd gravity field coefficients estimated from analysis of Juno and Cassini radiometric data.

Ka-band radio system enables a much clearer determination of Jupiter's odd gravity field to be obtained. Cassini's tracking system is based on the standard DST, operating in X-band, which does not allow the reduction of plasma noise. In addition, during Cassini's tracking, the water vapor radiometer was not operating (NASA only has two radiometers, currently both at DSS-25 for supporting Juno's observations), and accurate tropospheric calibrations were not possible. In addition, the need to solve for Saturn's normal modes enlarges the uncertainties on the static part of the gravity field. The result is that Saturn's odd harmonics are not determined as clearly as they are for Jupiter's. Jupiter's low-degree odd harmonics (J_3, J_5, J_7, and J_9) are all well determined, with the central values over the associated 3-sigma uncertainty. For Saturn, only J_3 and J_5 are determined above the 3-sigma level, with J_3 being only at 4-sigma from zero.

Figure 4.2 displays the contributions to odd coefficients from wind dynamics with different decay depths, compared to Juno's retrieved gravity field (horizontal lines). All the first four odd harmonics show a remarkable agreement with the theoretical predictions. All the measurements intersect (as an order of magnitude, since the model only has one free parameter) the model predictions for a depth of about 1000 to 3000 km, thus solving the long-standing question of Jupiter's wind depth. Also, Y. Kaspi and E. Galanti demonstrated that a latitudinal variation of the wind depth is required to accurately match Juno's measurements, as well as a more complex decay profile.

The situation of Saturn's wind dynamics is not as clear as for Jupiter. The only coefficient whose estimated value is much larger than the 3-sigma uncertainty, is J_5, whereas J_3 is determined at about 4-sigma. However, since the very deep differential rotation on Saturn has helped to determine the wind depth, Y. Kaspi found that the estimated value of the zonal wind depth is adequate to fit both J_3 and J_5. The model values are very close (and statistically compatible) with those estimated with Cassini's data. Thus, a thermal wind model with a depth of 40,000 km can fit both the low-degree odd and high-order even harmonics.

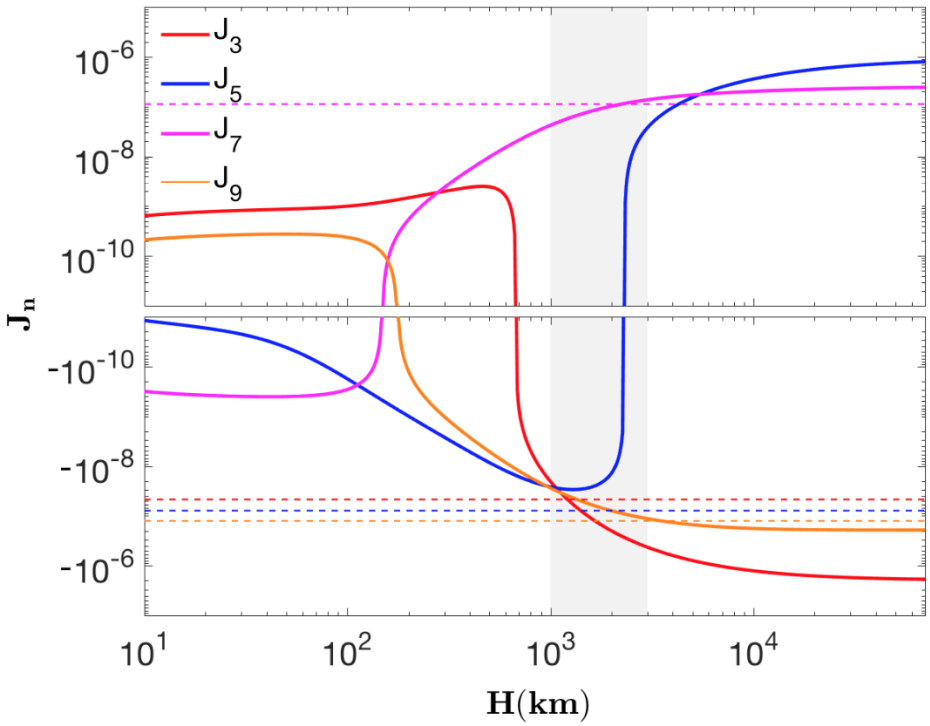

FIGURE 4.2: Jupiter's odd gravity field coefficients from wind dynamics: Juno's estimate (horizontal lines) are compared with model predictions (Y. Kaspi personal communication).

4.3 Saturn's normal modes: a clue or a mirage?

Potentially, one very interesting result is the need of a time-varying gravity field to fit Cassini Doppler data. However, as already discussed, the discrimination of the relevant modes is almost impossible. The data analysis has shown that different combinations of gravity and/or acoustic modes can be employed to obtain a good fit of the residuals, and much more combinations are surely possible.

The presence of normal modes inside Saturn has already been proved with ring seismology (Hedman and Nicholson, 2013; Hedman and Nicholson, 2014), and used to constrain the interior structure of the planet (Fuller, 2014). However, the rings are not sensitive to all the conceptually possible modes, and only a limited set can induce density waves within the rings. In particular, only tesseral and sectorial modes, with a determined frequency which resonates with the rings' particles at selected locations, induce a perturbation visible through the rings (to be more precise, only the order m of the gravity field can be determined). However, the modes observed with the rings are believed to have an amplitude which is one to two orders of magnitude lower than Cassini's formal uncertainty on the static component of the field (Fuller, 2014; Luan, Fuller, and Quataert, 2017). For that reason, solving for tesseral and sectorial coefficients was not attempted.

On the contrary, normal modes associated with zonal coefficients do not produce any perturbation in the rings, since the field is perturbed axial symmetrically, and all the particles would suffer the same perturbation, thus no local structure are generated. For this reason, which may be easily contested, only perturbations to zonal harmonics have been taken into account in Cassini's data analysis. In particular, only modes with lower frequency (period $\tau \gtrsim 30\ min$) have been included in the analysis, since the gravity data would not be sufficiently sensitive to higher frequency modes. Also, the sets selected in the analysis are only those able to fit the data, and additional tests have partially shown that a set which included only modes with larger frequencies do not produce satisfactory results, thus confirming that normal modes with periods of about half an hour to one or two hours are required.

Recently, Luan, Fuller, and Quataert, 2017 explained the Saturnian satellites' migration rate with resonance locking between them and internal oscillations of Saturn. They also predicted that these oscillations may be detected during the Cassini Grand Finale orbits, which may actually match Cassini's observation of a time-varying field.

To conclude, the question of whether normal modes have been found on not in Cassini's Doppler data is still unresolved.

4.4 Future constraints from Juno

Cassini ended its voyage on 15 September, 2017, with a plunge into Saturn's atmosphere, completing its mission after more than 10 years spent collecting scientific data around the Saturnian system. On the contrary, Juno arrived at Jupiter on 4 July, 2016, and still has major objectives to complete and long-standing questions to answer. Regarding Juno's gravity experiment, the future still has to deliver important answers, involving:

- Jupiter's higher degree zonal harmonics
- Jupiter's tesseral field
- Normal modes: gravity and acoustic oscillations
- Jupiter's response to the tidal perturbations and frequency dependence
- Spin-axis precession and the normalized polar moment of inertia

Higher degree zonal harmonics ($J_n > J_{12}$) are required to fit the data, but their central values do not exceed the 3-sigma formal uncertainty, thus a clear determination of these harmonics is still not possible. In the future, Juno will better constrain the magnitude of Jupiter's high-order gravity field, enabling the exploration of this region of the gravity spectrum as well, which is believed to be caused by wind dynamics, but additional physics actually not accounted for may be possible.

Concerning the tesseral field, Section 2.2.2 described the possibility of having a tesseral field induced by wind dynamics, in particular by the presence of vortices. Of great interest is a possible determination of a contribution from these particular structures on Jupiter's cloud level, in particular a gravity signal associated with the Great Red Spot would be very interesting as it would help to assess the penetration depth of this structure, which may be, in principle, different from that of the zonal flows. Parisi et al., 2016 demonstrated that for winds decaying with a depth $H > 2000km$ the signal coming from the Great Red Spot would be visible in Juno's Doppler data. This penetration depth is very close to the observed penetration depth of the zonal flow inferred from the analysis of the odd harmonics. Thus, a detection of that weak gravity signal with the upcoming Juno gravity-dedicated passes is desirable.

Additional constraints on the extend of Jupiter's tesseral field can be pose with a joint analysis between thermal wind models and orbit determination. The TW model can predict the values for Jupiter's gravity field, that can be tested with the orbit determination to check the consistency of the predicted model with the acquired gravity data (Galanti et al., 2017).

Another very important question is the presence of normal modes with a detectable amplitude. Durante, Guillot, and Iess, 2017 have shown that even in a scenario where

fundamental modes have much smaller radial velocity with respect to the higher-frequency p-modes, a gravity signal would appear in Juno's Doppler data. However, as for Cassini, a detection of the relevant mode characteristics (amplitude and frequency) may only be possible from a statistical point of view. In contrast to Cassini, Juno will probe Jupiter's gravity during more gravity-dedicated passes, and the greater accuracy of Juno's radio system may provide important information on the time-varying gravity field of Jupiter.

An additional way to probe Jupiter's interior is to determine its response to the tidal perturbation, induced by the Galilean satellites. The actual determination of Jupiter's Love number k_{22}, although perfectly compatible with theoretical predictions, is not yet sufficiently accurate to provide additional constraints on Jupiter's interior structure. Future passes will additionally increase Juno's accuracy on Jupiter's Love numbers, simulations declare up to degree four, helping to constrain the tidal response of the gas giant. In addition, a possible frequency-dependence of Jupiter's response may be investigated and determined in the case that it is much more different than that actually expected.

To conclude, the measurement of the precession constant of Jupiter's spin axis will provide a direct measurement of the polar moment of inertia (Le Maistre et al., 2016), which is an additional, important constraint on Jupiter's interior. In fact, the polar moment of inertia is a direct measurement of the degree of concentration of Jupiter's interior, thus directly probing the deep core.

Bibliography

Archinal, B. A. et al. (2011). "Report of the IAU Working Group on Cartographic Coordinates and Rotational Elements: 2009". In: *Celestial Mechanics and Dynamical Astronomy* 109, pp. 101–135. DOI: 10.1007/s10569-010-9320-4.

Asmar, S. W. et al. (2005). "Spacecraft Doppler tracking: Noise budget and accuracy achievable in precision radio science observations". In: *Radio Science* 40, RS2001, RS2001. DOI: 10.1029/2004RS003101.

Bagenal, F. et al. (1997). "Galileo measurements of plasma density in the Io torus". In: *Geophysical Research Letters* 24, p. 2119. DOI: 10.1029/97GL01254.

Barnes, J. A. et al. (1971). "Characterization of frequency stability". In: *IEEE Transactions on Instrumentation and Measurements* 20, pp. 105–120.

Bercovici, D. and G. Schubert (1987). "Jovian seismology". In: *Icarus* 69, pp. 557–565. DOI: 10.1016/0019-1035(87)90024-8.

Bertotti, B., G. Comoretto, and L. Iess (1993). "Doppler tracking of spacecraft with multi-frequency links". In: *Astronomy and Astrophysics* 269, pp. 608–616.

Bertotti, B., P. Farinella, and D. Vokrouhlick, eds. (2003). *Physics of the Solar System - Dynamics and Evolution, Space Physics, and Spacetime Structure.* Vol. 293. Astrophysics and Space Science Library. DOI: 10.1007/978-94-010-0233-2.

Bertotti, B., L. Iess, and P. Tortora (2003). "A test of general relativity using radio links with the Cassini spacecraft". In: *Nature* 425, pp. 374–376. DOI: 10.1038/nature01997.

Bolton, S. J. (2010). "The Juno Mission". In: *Galileo's Medicean Moons: Their Impact on 400 Years of Discovery*. Ed. by C. Barbieri et al. Vol. 269. IAU Symposium, pp. 92–100. DOI: 10.1017/S1743921310007313.

Choi, D. S. et al. (2007). "Velocity and vorticity measurements of Jupiter's Great Red Spot using automated cloud feature tracking". In: *Icarus* 188, pp. 35–46. DOI: 10.1016/j.icarus.2006.10.037.

Dederick, E. and J. Jackiewicz (2017). "A Possible Mechanism for Driving Oscillations in Hot Giant Planets". In: *The Astrophysical Journal* 837, 148, p. 148. DOI: 10.3847/1538-4357/aa61a8.

Durante, D., T. Guillot, and L. Iess (2017). "The effect of Jupiter oscillations on Juno gravity measurements". In: *Icarus* 282, pp. 174–182. DOI: 10.1016/j.icarus.2016.09.040.

Finocchiaro, S. (2013). "Numerical Simulations of the Juno Gravity Experiment". PhD thesis. Sapienza, University of Rome. URL: http://hdl.handle.net/10805/1889.

Finocchiaro, S. and L. Iess (2010). "Numerical simulations of the gravity science experiment of the Juno mission to Jupiter". In: *Advances in the Astronautical Sciences*. Vol. 136, pp. 1417–1426.

Fletcher, L. N. et al. (2009). "Methane and its isotopologues on Saturn from Cassini/CIRS observations". In: *Icarus* 199, pp. 351–367. DOI: 10.1016/j.icarus.2008.09.019.

Folkner, W. M. et al. (2017). "Jupiter gravity field estimated from the first two Juno orbits". In: *Geophysical Research Letters* 44.10. 2017GL073140, pp. 4694–4700. ISSN: 1944-8007. DOI: 10.1002/2017GL073140. URL: http://dx.doi.org/10.1002/2017GL073140.

Fortney, J. J. et al. (2016). "The Interior of Saturn". In: *ArXiv e-prints*. arXiv: 1609.06324 [astro-ph.EP].

French, R. G. et al. (2017). "Noncircular features in Saturn's rings IV: Absolute radius scale and Saturn's pole direction". In: *Icarus* 290, pp. 14–45. DOI: 10.1016/j.icarus.2017.02.007.

Fuller, J. (2014). "Saturn ring seismology: Evidence for stable stratification in the deep interior of Saturn". In: *Icarus* 242, pp. 283–296. DOI: 10.1016/j.icarus.2014.08.006.

Galanti, E., H. Cao, and Y. Kaspi (2017). "Constraining Jupiter's internal flows using Juno magnetic and gravity measurements". In: *Geophysical Research Letters* 44, pp. 8173–8181. DOI: 10.1002/2017GL074903.

Galanti, E. et al. (2017). "Estimating Jupiters Gravity Field Using Juno Measurements, Trajectory Estimation Analysis, and a Flow Model Optimization". In: *The Astronomical Journal* 154, 2, p. 2. DOI: 10.3847/1538-3881/aa72db.

Gaulme, P. et al. (2011). "Detection of Jovian seismic waves: a new probe of its interior structure". In: *Astronomy and Astrophysics* 531, A104, A104. DOI: 10.1051/0004-6361/201116903.

Gaulme, P. et al. (2015). "Seismology of Giant Planets". In: *Extraterrestrial Seismology*. Ed. by V. C. H. Tong and R. A. Garcìa. Cambridge, UK: Cambridge University Press, pp. 189–202.

Goldreich, P., N. Murray, and P. Kumar (1994). "Excitation of solar p-modes". In: *Astrophysical Journal* 424, pp. 466–479. DOI: 10.1086/173904.

Gudkova, T. V. and V. N. Zharkov (2006). "Theoretical free oscillations spectrum for Saturn interior models". In: *Advances in Space Research* 38, pp. 764–769. DOI: 10.1016/j.asr.2006.02.042.

Guillot, T. (2005). "THE INTERIORS OF GIANT PLANETS: Models and Outstanding Questions". In: *Annual Review of Earth and Planetary Sciences* 33, pp. 493–530. DOI: 10.1146/annurev.earth.32.101802.120325.

Guillot, T., D. Gautier, and W. B. Hubbard (1997). "NOTE: New Constraints on the Composition of Jupiter from Galileo Measurements and Interior Models". In: *Icarus* 130, pp. 534–539. DOI: 10.1006/icar.1997.5812.

Hedman, M. M. and P. D. Nicholson (2013). "Kronoseismology: Using Density Waves in Saturn's C Ring to Probe the Planet's Interior". In: *The Astronomical Journal* 146, 12, p. 12. DOI: 10.1088/0004-6256/146/1/12.

— (2014). "More Kronoseismology with Saturn's rings". In: *Monthly Notices of the Royal Astronomical Society* 444, pp. 1369–1388. DOI: 10.1093/mnras/stu1503.

— (2016). "The B-ring's surface mass density from hidden density waves: Less than meets the eye?" In: *Icarus* 279, pp. 109–124. DOI: 10.1016/j.icarus.2016.01.007.

Helled, R. et al. (2011). "Jupiters moment of inertia: A possible determination by Juno". In: *Icarus* 216, pp. 440–448. DOI: 10.1016/j.icarus.2011.09.016.

Hubbard, W. B. (1999). "NOTE: Gravitational Signature of Jupiter's Deep Zonal Flows". In: *Icarus* 137, pp. 357–359. DOI: 10.1006/icar.1998.6064.

— (2012). "High-precision Maclaurin-based Models of Rotating Liquid Planets". In: *The Astrophysical Journal Letters* 756, L15, p. L15. DOI: 10.1088/2041-8205/756/1/L15.

— (2013). "Concentric Maclaurin Spheroid Models of Rotating Liquid Planets". In: *The Astrophysical Journal* 768, 43, p. 43. DOI: 10.1088/0004-637X/768/1/43.

Hubbard, W. B. and B. Militzer (2016). "A Preliminary Jupiter Model". In: *The Astrophysical Journal* 820, 80, p. 80. DOI: 10.3847/0004-637X/820/1/80.

Iess, L. et al. (2014). "The Gravity Field and Interior Structure of Enceladus". In: *Science* 344, pp. 78–80. DOI: 10.1126/science.1250551.

Jackiewicz, J. et al. (2012). "Forward and inverse modeling for jovian seismology". In: *Icarus* 220, pp. 844–854. DOI: 10.1016/j.icarus.2012.06.028.

Jacobson, R. A. et al. (2006). "The Gravity Field of the Saturnian System from Satellite Observations and Spacecraft Tracking Data". In: *The Astronomical Journal* 132, pp. 2520–2526. DOI: 10.1086/508812.

Kaspi, Y. (2013). "Inferring the depth of the zonal jets on Jupiter and Saturn from odd gravity harmonics". In: *Geophysical Research Letters* 40, pp. 676–680. DOI: 10.1029/2012GL053873.

Kaspi, Y. et al. (2010). "Gravitational signature of Jupiter's internal dynamics". In: *Geophysical Research Letters* 37, L01204, p. L01204. DOI: 10.1029/2009GL041385.

Kaspi, Y. et al. (2017). "The effect of differential rotation on Jupiter's low-degree even gravity moments". In: *Geophysical Research Letters* 44, pp. 5960–5968. DOI: 10.1002/2017GL073629.

Lainey, V. et al. (2017). "New constraints on Saturn's interior from Cassini astrometric data". In: *Icarus* 281, pp. 286–296. DOI: 10.1016/j.icarus.2016.07.014.

Le Maistre, S. et al. (2016). "Jupiter spin-pole precession rate and moment of inertia from Juno radio-science observations". In: *Planetary and Space Science* 126, pp. 78–92. DOI: 10.1016/j.pss.2016.03.006.

Luan, J., J. Fuller, and E. Quataert (2017). "How Cassini Can Constrain Tidal Dissipation in Saturn". In: *ArXiv e-prints*. arXiv: 1707.02519 [astro-ph.EP].

Marini, J. (1972). "A Test of the Effect of Satellite Spin on Two-Way Doppler Range-Rate Measurements". In: *IEEE Transactions on Aerospace Electronic Systems* 8, pp. 269–272. DOI: 10.1109/TAES.1972.309508.

Mariotti, G. and P. Tortora (2013). "Experimental validation of a dual uplink multifrequency dispersive noise calibration scheme for Deep Space tracking". In: *Radio Science* 48, pp. 111–117. DOI: 10.1002/rds.20024.

Miguel, Y., Guillot, T., and Fayon, L. (2016). "Jupiter internal structure: the effect of different equations of state". In: *Astronomy And Astrophysics* 596, A114. DOI: 10.1051/0004-6361/201629732. URL: https://doi.org/10.1051/0004-6361/201629732.

Militzer, B. and W. B. Hubbard (2013). "Ab Initio Equation of State for Hydrogen-Helium Mixtures with Recalibration of the Giant-planet Mass-Radius Relation". In: *The Astrophysical Journal* 774, 148, p. 148. DOI: 10.1088/0004-637X/774/2/148.

Militzer, B. et al. (2008). "A Massive Core in Jupiter Predicted from First-Principles Simulations". In: *The Astrophysical Journal* 688, L45, p. L45. DOI: 10.1086/594364.

Militzer, B. et al. (2016). "Understanding Jupiter's interior". In: *Journal of Geophysical Research (Planets)* 121, pp. 1552–1572. DOI: 10.1002/2016JE005080.

Mosser, B. (1995). "Propagation and trapping of global oscillations in the Jovian troposphere and stratosphere." In: *Astronomy and Astrophysics* 293.

Mosser, B., J. P. Maillard, and D. Mékarnia (2000). "New Attempt at Detecting the Jovian Oscillations". In: *Icarus* 144, pp. 104–113. DOI: 10.1006/icar.1999.6271.

Naudet, C. J. et al. (2000). "The Media Calibration System for Cassini Radio Science: Part I". In: *Interplanetary Network Progress Report* 143, pp. 1–8.

Nerney, E. G., F. Bagenal, and A. J. Steffl (2017). "Io plasma torus ion composition: Voyager, Galileo, and Cassini". In: *Journal of Geophysical Research (Space Physics)* 122, pp. 727–744. DOI: 10.1002/2016JA023306.

Nettelmann, N. (2017). "Low- and high-order gravitational harmonics of rigidly rotating Jupiter". In: *Astronomy And Astrophysics* 606, A139, A139. DOI: 10.1051/0004-6361/201731550.

Niell, A. E. (1996). "Global mapping functions for the atmosphere delay at radio wavelengths". In: *Journal of Geophysical Research* 101, pp. 3227–3246. DOI: 10.1029/95JB03048.

Parisi, M. et al. (2016). "Probing the depth of Jupiter's Great Red Spot with the Juno gravity experiment". In: *Icarus* 267, pp. 232–242. DOI: 10.1016/j.icarus.2015.12.011.

Phipps, P. H. and P. Withers (2017). "Radio occultations of the Io plasma torus by Juno are feasible". In: *Journal of Geophysical Research (Space Physics)* 122, pp. 1731–1750. DOI: 10.1002/2016JA023447.

Seidelmann, P. K. et al. (2002). "Report of the IAU/IAG Working Group on Cartographic Coordinates and Rotational Elements of the Planets and Satellites: 2000". In: *Celestial Mechanics and Dynamical Astronomy* 82, pp. 83–111.

Tanner, A. B. (1998). "Development of a high-stability water vapor radiometer". In: *Radio Science* 33, pp. 449–462. DOI: 10.1029/97RS02749.

Tommei, G. et al. (2015). "On the Juno radio science experiment: models, algorithms and sensitivity analysis". In: *Monthly Notices of the Royal Astronomical Society* 446, pp. 3089–3099. DOI: 10.1093/mnras/stu2328.

Vorontsov, S. V., V. N. Zharkov, and V. M. Lubimov (1976). "The free oscillations of Jupiter and Saturn". In: *Icarus* 27, pp. 109–118. DOI: 10.1016/0019-1035(76)90187-1.

Wahl, S. M., W. B. Hubbard, and B. Militzer (2016). "Tidal Response of Preliminary Jupiter Model". In: *The Astrophysical Journal* 831, 14, p. 14. DOI: 10.3847/0004-637X/831/1/14.

— (2017). "The Concentric Maclaurin Spheroid method with tides and a rotational enhancement of Saturn's tidal response". In: *Icarus* 282, pp. 183–194. DOI: 10.1016/j.icarus.2016.09.011.

Wahl, S. M. et al. (2017). "Comparing Jupiter interior structure models to Juno gravity measurements and the role of a dilute core". In: *Geophysical Research Letters*.

Ward, W. R. and R. M. Canup (2006). "The Obliquity of Jupiter". In: *The Astrophysical Journal* 640, pp. L91–L94. DOI: 10.1086/503156.